論文 / 著書情報
Article / Book Information

題目(和文)	エポキシ樹脂の破壊靭性に及ぼす熱粘弾性の影響
Title(English)	Thermo-Viscoelastic Effect on Fracture Toughness of Epoxy Resin
著者(和文)	荒木稚子
Author(English)	Wakako Araki
出典(和文)	学位:工学博士, 学位授与機関:東京工業大学, 報告番号:乙第3794号, 授与年月日:2005年3月31日, 学位の種別:論文博士, 審査員:足立忠晴
Citation(English)	Degree:Doctor of Engineering, Conferring organization: Tokyo Institute of Technology, Report number:乙第3794号, Conferred date:2005/3/31, Degree Type:Thesis doctor, Examiner:
学位種別(和文)	博士論文
Type(English)	Doctoral Thesis

Thermo-Viscoelastic Effect on Fracture Toughness of Epoxy Resin

Wakako Araki

Thermo-Viscoelastic Effect on Fracture Toughness of Epoxy Resin

by
Wakako Araki

A DISSERTATION

submitted to

Tokyo Institute of Technology

in partial fulfillment of
the requirements for the degree of

Doctor of Engineering

ACKNOWLEDGEMENTS

During the writing of this dissertation, I received many helps from the persons whom I would like to thank. First of all, I would like to sincerely thank my major supervisors, Prof. Tadaharu Adachi and Prof. Akihiko Yamaji, for all their help and advice during all of the works toward this dissertation. Secondly, I wish to thank Prof. Akira Todoroki, Prof. Naoto Otake, Prof. Kikuo Kishimoto, Prof. Isao Sato, and Prof. Masatoshi Kubouchi, for their meticulous feedback and advice. I would also thank Mr. Masahiro Gamou for his kindly experimental help. Finally, I should like to thank to all the persons concerned with this dissertation.

TABLE OF CONTENTS

NOTATION

a_T	Shift factor
E'	Dynamic storage modulus
E''	Dynamic loss modulus
I_{epo}	Intensity of a peak concerning epoxide ring vibration in Raman spectra
I_{ref}	Intensity of a reference peak in Raman spectra
K_i	Stress intensity factor (i=I, II)
K_{ic}	Fracture toughness (i=I, II)
m	Angell's fragility
R_a	Average surface roughness
T	Temperature
T_g	Glass transition temperature
T_R	Reference temperature of time-temperature equivalent principle
t	Time
t_f	Fracture initiation time
ΔH	Apparent thermal activation energy
τ	Relaxation time

Chapter 1

Introduction

1.1 PREFACE

Epoxy resins are widely used in various engineering fields, because of their excellent mechanical characteristics, electrical insulation, and adhesion. In general, their thermo-viscoelasitc properties are related to their network morphology of epoxy resins. The network morphology depends on how they are cured, so an appropriate curing process must be selected according to the type of epoxy resin and curing agent in order to obtain consistent products with the desired physical and mechanical properties.

With the rapid development of electronics technology, the application field of epoxy resins and their composites has expanded. In the electronics industry, they are now used for casting, molding, encapusulation, and sealing. Higher performance and reliability under various environments of temperature and time are required of electronic devices in these days, so predicting their thermo-mechanical and fracture behaviors in these environments has become more important recently.

However, no papers have discussed the fracture property of epoxy resins in terms of its time and temperature dependences, which is attributed to their network morphology. Moreover, any method for predicting fracture initiation in thermo-viscoelastic materials as epoxy resins has not been established.

It is therefore significant both industrially and scientifically to establish methods for estimating the fracture property with time-temperature dependence and also for predictioning the fracture initiation in consideration of thermo-viscoelastic effects.

1.2 EPOXY RESIN[1.1,1.2]

Epoxy resin is a family of thermosetting resins containing more than two oxirane structures, three-membered rings containing two carbon atoms and one oxygen atom, namely the epoxide group for epoxy resins (Fig. 1.1).

Most common epoxy resins are glycidyl ethers of alcohols or phenolics, but many epoxy resins are now generally formed from low-molecular-weight diglicidyl ethers of bisphenol A (DGEBA), which are made by condensing epichlorohydrin and bisphenol A. DGEBA accounts for more than 75% of the epoxy resin used in industrial applications because, when cured, it has excellent toughness, adhesiveness, and chemical resistance. The structure of DGEBA is shown in Fig. 1.2. Depending on the molecular weight, and thus variable n, epoxy resins range from liquids to solids. Epoxy resins such as DGEBA have the ability to react and cross-link via the epoxide group on each end to generate three-dimensional networks, which provides cured epoxy resins that do not reflow. The chemicals chosen to react with these epoxide groups are called curing agents and typically have active hydrogen attached to nitrogen, oxygen, or sulfur. Selection of the curing agents determines characteristics of the cured epoxy resins. Well-known curing agents are polyamines, acid anhydrides, and polymerization catalysts. Among these, acid anhydride curing provides epoxy resins with a high glass transition temperatures and excellent mechanical properties, especially at high temperature. In addition, the shrinkage caused by curing is small. The structure of the acid anhydride curing agent is shown in Fig. 1.3.

The anhydrides are sometimes used alone, but they are more frequently used in combination with such basic compounds such as tertiary amine catalysts to accelerate the curing. The mechanism, which is not well understood though, is roughly shown in Fig. 1.4.

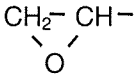

Figure 1.1 Epoxide group

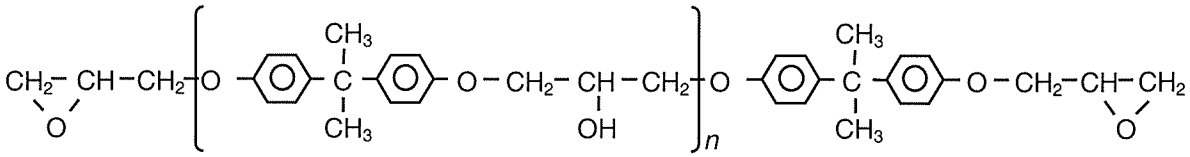

Figure 1.2 Structure of DGEBA

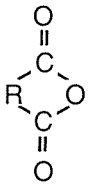

Figure 1.3 Structure of acid anhydride curing agent

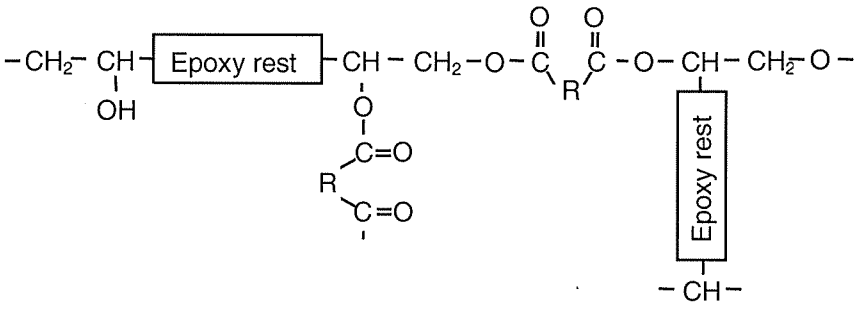

Figure 1.4 Schematic structure of acid anhydrides-cured epoxy resin

1.3 NETWORK MORPHOLOGY

1.3.1 Degree of cross-linking reaction

The network morphology of cured epoxy resin is governed by the curing process.

In general, it is characterized by the degree of the cross-linking reaction, which is estimated from the variation of physical properties related to this chemical reaction, such as the glass transition temperature, T_g. The T_g can be easily obtained in several ways such as thermo mechanical analysis and differential scanning calorimetry.

Bunn[1.3] considered that the energy level of a conformer at the ends of a chain is considerably higher than that of a similar conformer in the interior of the chain. The chain end can be alternatively described as having a larger free volume. For a linear polymer, the decreases of T_g that occur with the lowering of the molecular weight are quantitatively attributed to the increase in the number of chain ends for a given mass. Matsuoka[1.4] has reported that whenever an epoxide group reacts with a curing agent, a certain amount of free volume is lost and T_g rises incrementally.

In the early stage of the curing reaction, T_g increases slowly with the degree of cross-linking reaction, and then increases monotonically.[1.5-1.7] The last stage of the curing reaction slows as a molecular motion becomes restricted in the highly cross-linked network of polymer molecules.[1.8] In fact, when the curing reaction proceeds to a certain extent and approaches its maximum, the reaction becomes 80 to 90 percent of the ideal reaction rate and T_g saturates at a constant value[1.7,1.9] A number of researchers have demonstrated that there is a unique relationship between T_g and the degree of cross-linking for epoxy resins.[1.9-1.13] The relationship has been derived from the equations based on thermodynamic consideration, which are independent of curing process.[1.5,1.10,1.14,1.15]

The T_g is closely related to the degree of cross-linking and is therefore one of the most important parameters to identify the network morphology of epoxy resins.

1.3.2 Heterogeneity of cross-link density

Several researchers have obtained found that amorphous polymers are heterogeneous with respect to the density distribution in the range of 10 to 10^2 nm.[1.9,1.16-1.20]

The studies of the heterogeneity of epoxy resins have mainly relied on observations by electron microscopy and partly on thermal behavior analyses near T_g. Racich[1.16] observed a nodular morphology with node sizes ranging from 10-60 nm on free surfaces and fracture surfaces of epoxy resins of widely different cure and chemistry. Stevens et al.[1.19] revealed, based on his static light-scattering studies, that there are some heterogeneities 20-70 nm in size already existing in epoxy resins derived from DGEBA. Lunak et al.[1.9] found nodular structures, i.e., heterogeneous structures, in the fracture surfaces of epoxy resin and other amorphous polymers and that there is no correlation between the heterogeneous structures and

the cross-linking degree within a series of DGEBA samples cured with diamines and anhydrides. Dusek et al. [1.17] observed globular structures 20-40 nm in size by electron microscopy and small-angle X-ray scattering (SAXS). Kong[1.20], based on his SAXS results, expressed the epoxy resins by using a network model with a very non-uniform cross-link density; there are regions of higher cross-link density are embedded in a matrix of lower cross-link density of the order of 4-7 nm.

The heterogeneity of amorphous materials is interpreted by Adam and Gibbs et al. [1.21,1.22] as follows: There are some regions in glass-forming materials where molecules must move cooperatively. These "cooperatively rearranging regions" make a material heterogeneous, which probably causes the wide distribution of molecular relaxation time. Dusek et al.[1.17] pointed out, based on their experimental results, that a complicated system with heterogeneity might be caused either by thermodynamic incompatibility or by some non-alternating mechanisms in the curing reaction.

The fragility parameter, m, which was proposed by Angell[1.23] has recently attracted much attention as a parameter related to the density heterogeneity of amorphous materials. He proposed m as a basis for classifying supercooled materials according to the variations in their dynamic properties at temperatures above T_g based on the concept of intermolecular cooperativity. Kanaya et al.[1.24,1.25] found that the heterogeneity is correlated with the fragility for amorphous polymers based on incoherent elastic scattering data. The m and the cooperativity have been used as parameters to represent the heterogeneity of various amorphous materials and applied to characterize cross-linked polymers.[1.8,1.26-1.30]

The fragility, m, could be related to the physical heterogeneity of the network density in the nanometer to micrometer scale, while the glass transition temperature, T_g, represents the degree of chemical cross-linking reaction in a macro-scale; therefore, m could be a complementary parameter with T_g and together they may enable us to identify the network morphology of epoxy resins.

1.4 THERMO-VISCOELASTICITY

The mechanical behavior of polymers is known to be thermo-viscoelastic. The behavior of thermo-viscoelastic materials strongly depends on experimental scale of the time, t, and temperature, T, due to molecular relaxation. Each molecular time-relaxation displays a characteristic temperature dependence. Assuming that the material exhibits only one or one active molecular transition, the materials behavior is "thermo-rheologically simple," meaning that all relaxation times have the same temperature dependence. Many thermo-viscoelastic polymers are known to be thermo-rheologically simple materials that obey the time-temperature equivalence principle. Schwarzl and Staverman[1.31] first showed that the observation of a pure time shift is sometimes used to identify thermo-rheologically simple

material behavior. Leaderman[1.32] proposed the principle of time-temperature equivalence principle with a reduced time, ξ, and a shift factor, a_T, to describe this behavior.

The time-temperature equivalence principle is briefly illustrated in Fig. 1.5. First, viscoelastic property, for example relaxation modulus shown in the fugure, is measured at various temperatures in the same time range. On the basis of the time dependence of the modulus at the standard temperature, T_R, all moduli measured at different temperatures are shifted horizontally so as to superpose the curves each other. A curve produced by this superposition is called master curve and the amount of time shift for each temperature is called a shift factor, a_T. The new time axis for the master curve is called the reduced time, ξ, at T_R. Thus, this principle states that viscoelastic data obtained at different temperatures can be superposed onto a master curve only by a horizontal shift along the logarithmic time (or frequency) axis. Conversely, the viscoelastic property in a broad time range at T_R can be obtained in the reverse way. The broad temperature dependence of the viscoelastic property at a standard time (or frequency) can also be obtained in a similar way.

For the great majority of relaxations, a_T is generally given one of two equations. One is the Williams-Landel-Ferry (WLF) equation[1.33]

$$\log a_T = \frac{-C_1(T - T_r)}{C_2 + T - T_r}, \qquad (1.1)$$

where C_1 and C_2 are constants, and T_r is the reference temperature. The WLF equation is almost always applicable to glass-rubber relaxation. The other is the Arrhenius equation[1.34]

$$\ln a_T = \frac{\Delta H}{R}\left(\frac{1}{T} - \frac{1}{T_r}\right), \qquad (1.2)$$

where ΔH is an apparent activation energy and R the universal gas constant, and which assumes that the relaxation phenomenon is the thermal activation process. Typical a_T and ΔH as Arrhenius plots are shown in Fig. 1.6.

The relaxation phenomenon of epoxy resins is attributed to the movement and interaction of network chains, so that the thermo-viscoelastic behavior can be attributed to the network morphology, i.e., the cross-linking degree and the heterogeneity.

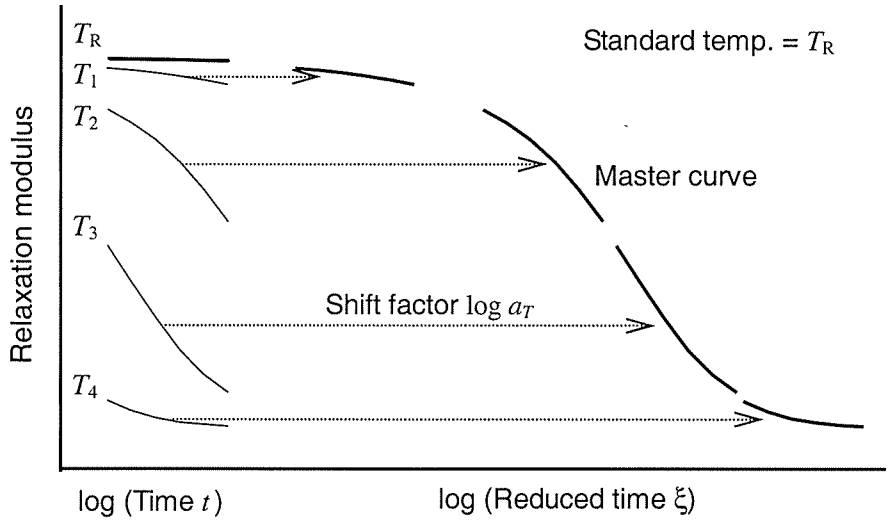

Figure 1.5 Time-temperature equivalence principle

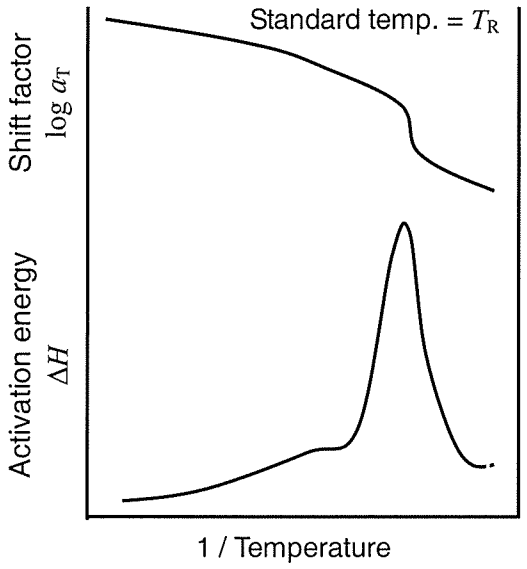

Figure 1.6 Arrhenius plots of shift factor and apparent activation energy

1.5 FRACTURE TOUGHNESS

1.5.1 Fracture toughness and network morphology

It is known that the mechanical properties of epoxy resins, such as Young's modulus, and yield stres,[1.36,1.37] depend on the degree of cross-linking reaction. Shimbo et al. [1.37,1.38] showed that the tensile modulus, tensile strength, and elongation in glassy state are correlated with the cross-linking degree in DGEBA systems. Ogata et al.[1.39] showed that the coefficient of thermal expansion increases in glassy state but that decreases in rubbery state with increasing a degree of cross-linking reaction, which is related to T_g. Also, we know experimentally that insufficiently cured epoxy resins have low T_g and poor mechanical properties because of the low cross-linking degree and the existence of unreacted monomers.

Several studies have examined the relationship between the cross-linking degree and fracture properties of the epoxy resins.[1.35,1.40-1.44] Pearson and Yee[1.40] found that epoxy resins with high molecular weight have low T_g and high fracture toughness. Similar results were reported for epoxy resins with different reactant ratios and molecular weights.[1.35,1.41-1.43] In contrast, Min et al.[1.44] showed that the fracture toughness increases with T_g for epoxy resins cured at different temperatures even when the prepolymer system is the same. They also suggested, based on comparisons with previous studies where the reactant ratio or molecular weight of epoxy prepolymers was varied,[1.42,1.43] that the cross-link density is not always a strong determining factor for fracture toughness and that other structural parameters, such as free volume, chain flexibility, and the degree of intermolecular packing, are more likely to be responsible.

The relationship between the fracture properties and the heterogeneity of the network morphology has been discussed in several papers.[1.45-1.47] Kim et al.[1.45] showed that the fracture toughness, impact strength, and tensile energy are quite sensitive the heterogeneity with respect to stoichiometry but that the tensile strength, the modulus, and the ultimate elongation are relatively insensitive to it. Mijovic and Koutsky[1.46] showed that the fracture toughness of epoxy resins depends on the nodule size, which were induced by the concentration of curing agent. Kelley and Trainor[1.47] clarified the correlation between the fracture toughness and the heterogeneity with respect to cross-link density distribution for cross-linked polystyrene and suggested the possibility of a similar correlation for epoxy resins.

The fracture toughness of epoxy resin is likely to be related to the network morphology; not only the cross-linking degree but also the heterogeneity. However, no effective quantitative parameter for determining the heterogeneity related to fracture behavior has been suggested. Parameters for evaluating the network morphology of epoxy resins will be useful in estimating fracture toughness and thus in determining curing conditions. Most papers on fracture toughness have dealt with mode I fracture; however, fractures generally initiate at preexisting flaws oriented at arbitrary angles to the farfield loading direction, so

mode II and also multiaxial mode fractures should be also considered.

1.5.2 Fracture toughness with time-temperature dependence

The time-temperature equivalence principle has been applied to examine fracture properties in a way similar to how it is used to viscoelastic properties.[1.48-1.50] Bueche[1.48] and Kasamori et al.[1.49] reported that the principle is valid for strength data and its master curves can be obtained by using the a_T of the viscoelastic properties. Recently, several studies[1.51-1.61] has that the fracture toughness has the time and temperature dependence just like the viscoelastic properties do. Popelar et al.[1.51] and Adachi et al.[1.59,1.60] found that the fracture toughness has the same shift factor as the viscoelastic properties. Frassine at al.[1.54,1.55,1.57] obtained the master curve of the fracture toughness from the a_T of the yield stress. Lim et al.[1.52] reported that the fracture toughness has the same a_T as the tensile strength.

Epoxy materials have been experimentally proved to be thermo-rheologically simple ones.[1.59,1.60,1.62,1.63] As for the fracture properties of epoxy materials[1.59,1.64], Miyano et al.[1.62] have studied the flexural strength of the fiber-reinforced epoxy resins and obtained its master curve. Adachi et al.[1.58] showed that the fracture toughness of epoxy composites has the time and temperature dependence and follows the principle.

The time-temperature dependence of fracture toughness must therefore be taken into account in examining the fracture behavior of thermo-viscoelastic materials such as epoxy resins. If the time-temperature equivalence principle can be applied to fracture toughness, the broad time or temperature dependence of the fracture toughness could be easily obtained by using it. Moreover, the relaxation phenomena attributed to the network morphology could greatly affect the time-temperature dependence of fracture toughness, so that the effect of the network morphology should be examined.

1.5.3 Fracture initiation in thermo-viscoelastic media

Many papers have treated the thermo-mechanical behaviors of viscoelastic materials.[1.65,1.66] Fundamental studies were carried out in the 1960s. Morland and Lee[1.67] proposed a constitutive law for thermo-rheologically simple media. Muki and Sternberg[1.68] analyzed the transient temperature and stress fields in simple geometries with a plate or polar symmetry.

The fracture phenomenon in viscoelastic media with pre-existing cracks has been theoretically and numerically studied in the past decade. Schapery[1.69-1.71] and Christensen[1.72,1.73] respectively researched fracture criteria for crack initiation and growth for viscoelastic materials. Their criteria were based on an energy balance theory, and the fracture initiation time could be predicted according to each criterion by using the inherent fracture energy, which is assumed to be constant. Moreover, in attempts to find a fracture criterion for

thermo-viscoealstic media, many researchers have theoretically extended these criteria and numerically analyzed various fracture problems.[1.74-1.78]

Most researchers have analyzed fracture behaviors, allowing for stress fields with the thermo-viscoelastic property; however, the time-temperature dependence of fracture toughness has rarely been taken into account. The time-temperature dependence of the stress field as well as that of the fracture toughness should be considered in addressing the fracture problems of thermo-viscoelastic media as such epoxy materials.

1.6 PURPOSE

As mentioned above, the fracture toughness of epoxy resin is likely related to the network morphology (not only to the cross-linking degree but also to the heterogeneity) and could have both time and temperature dependence because of the thermo-viscoelastic relaxation attributed to the network morphology. Therefore, in addressing for the fracture problems, the time-temperature dependence of the fracture toughness and also the stress field should be considered.

However, the time and temperature dependences of fracture toughness have been rarely taken into account in most researches. No effective quantitative parameters for the network morphology, which is closely related to the fracture behavior with time-temperature dependence, have been suggested. Moreover, not only mode I fractures but also mode II and multiaxial mode fractures should be considered, although most papers have only dealt with mode I fracture toughness. In most analyses of fracture behavior in thermo-viscoelastic materials, the time-temperature dependence of fracture toughness has not been taken into account even when the stress field was assumed to be thermo-viscoelastic.

The purpose of this dissertation is to clarify the thermo-viscoelastic effects on the fracture toughness of epoxy resin. In the present study, I deal with a system consisting of DGEBA, acid anhydride curing agent, and tertiary amine accelerator, which is most general one in the use for electric products.

Particularly, I have three objectives: One is to clarify the relationship between the fracture toughness and the network morphology, which is closely related to thermo-viscoelasticity. Parameters for the network morphology will be useful for estimating fracture toughness and also for determining curing conditions. The second one is to clarify the time-temperature dependence of the fracture toughness due to the thermo-viscoelastic relaxation. If the time-temperature equivalence principle can be applied to fracture toughness, the broad time-temperature dependence of the fracture toughness could be easily obtained using it. The third one is to propose a method for predicting fracture initiation in thermo-viscoelastic materials, allowing for the time-temperature dependences of the fracture toughness as well as that of the stress field.

1.7 CONTENTS

In Chapter 2, "Mode I fracture toughness at room temperature," I discuss the effects of network morphology on mode I fracture toughness at room temperature for a bisphenol-A type epoxy resin and silica particulate-filled epoxy composite. Network morphologies of the epoxy resins and the composites cured under various time and temperature conditions are identified by the glass transition temperature, T_g, and fragility parameter, m, which are derived from the thermo-viscoelasticity. The specimens are examined using a laser Raman spectrophotometer, a differential interference microscope, an atomic force microscope, and a scanning electron microscope. Also I perform a three-point bendint test at room temperature to obtain mode I fracture toughness, K_{Ic}. I discuss the relationships between T_g, m, and K_{Ic}, based on the results of these examinations.

In Chapter 3, "Time-temperature dependence of mode I fracture toughness," I discuss the time-temperature dependence of K_{Ic} for the bisphenol A-type epoxy resin and silica particulate-filled epoxy composite, allowing for the effects of the network morphology. The network morphologies of the epoxy resins and composites cured under various conditions are identified by the T_g and m derived from the thermo-viscoelasticity measurement, as is done in Chapter 2. I first conduct a three-point bending test under various conditions of displacement rate and temperature to clarify the time-temperature dependence of K_{Ic} for each material. Based on the results, I examine the applicability of time-temperature equivalence principle to K_{Ic}. Then, I discuss the relationship between T_g, m, and the time-temperature dependence of K_{Ic}.

In Chapter 4, "Time-temperature dependence of mode II fracture toughness," I discuss the time-temperature dependence of mode II fracture toughness for the epoxy resin allowing for the effects of the network morphology. An asymmetric four-point bending test at room temperature was carried out to obtain mode II fracture toughness, K_{IIc}, for specimens cured under various conditions. Based on the results, the relationship between the network morphology and K_{IIc} at the room temperature is briefly discussed. Then, I conduct the fracture test under various displacement rate and temperature conditions to investigate time-temperature dependence of K_{IIc}. From these results, I examine the applicability of time-temperature equivalence principle to K_{IIc}. Then, I discuss the time-temperature dependence of K_{IIc} compared with that of K_{Ic}.

In Chapter 5, "Mixed mode I/II fracture toughness at room temperature," I discuss a fracture criterion of the epoxy resins for mixed mode I/II at the room temperature. Epoxy resins with different T_g are examined in order to clarify the effect of T_g on the mixed mode I/II fracture toughness. I compare the experimental results with common four fracture criteria: maximum hoop stress criterion, minimum strain energy density criterion, maximum stress release rate criterion, and Richard's empirical criterion. Based on the results, I discuss the

onset of fracture and the direction of crack initiation for epoxy resins with different T_g and the thermo-viscoelastic effects on fracture criteria for thermo-viscoelastic materials such as epoxy materials.

In Chapter 6, "Prediction of fracture initiation in thermo-viscoelastic media," I propose a method for predicting fracture initiation time for thermo-viscoelastic media with time-temperature dependent properties. First, I analyze thermal stress on a thermo-viscoelastic hollow cylinder with temperature-dependent thermal properties. The cylinder is heated gradually at the inner surface and kept at the initial temperature at the outer surface. The material of the cylinder is thermo-rheologically simple and has a temperature-dependent coefficient of linear thermal expansion, thermal conductivity, and thermal diffusivity (and/or specific heat). Based on the analysis results, I discuss the effects of thermo-viscoelasticity and temperature-variable thermal properties on the stress field. Next, I propose the method for predicting fracture initiation time for thermo-viscoelastic media from such stress field and the fracture toughness, allowing for both time-temperature dependences. I explain the concept of the method through the use of master curves of the stress intensity factor and fracture toughness derived according to the time-temperature equivalence principle. Then, as concrete examples, I analyze stress intensity factors in a thermo-viscoelastic cylinder with a crack under various conditions of temperature and crack length to explain the prediction process.

In Chapter 7, I summarize the conclusion drawn in each chapter and state overall conclusion of this dissertation. I finally show views for the future concerning this dissertation.

REFERENCES

1.1 M. Shimbo, Epoxy resin. In *Handbook of Epoxy Resins* (Ed. M. Shimbo), Nikkan Kogyo Shinbunsha, Tokyo, 19-131 (1987). (in Japanese)

1.2 S. Muroi and H. Ishimura, Outline of epoxy resin. In *Epoxy Resin*, Koubunshi Kankoukai, Kyoto, 1-21 (1988). (in Japanese)

1.3 C.W. Bunn, The melting points of chain polymers, J. Polym. Sci. 16, 323-343 (1955).

1.4 S. Matsuoka, Related topics. In *Relaxation Phenomena in Polymers,* Oxford University Press, New York, 239-249 (1992).

1.5 J.P. Pascault and R.J.J. Williams, Glass transition temperature versus conversion relationships for thermosetting polymers, J. Polym. Sci. 28, 85-95 (1990).

1.6 J.H. Lee, J.W. Lee, Kinetic parameters estimation for cure reaction of epoxy based vinyl ester resin, Polym. Eng. Sci. 34, 742-749 (1994).

1.7 F.Y.C. Boey, W. Qiang, Glass-transition temperature-conversion relationship for an epoxy –hexahydro-4-methylphthalic anhydride system, J. Appl. Polym. Sci. 78, 511-516 (2000).

1.8 S. Matsuoka, X. Quan, H.E. Bair, and D.J. Boyle, A model for the curing reaction of epoxy resins, Macromol. 22 4093-4098 (1989).

1.9 S. Lunak, J. Vladyka, and K. Dusek, Effect of diffusion control in the glass transition region on critical conversion at the gel point during curing of epoxy resins, Polym. 19, 931-933 (1978).

1.10 E. Lawrence and L.E. Nielsen, Cross-linking – Effect on physical properties of polymers, J. Macromol. Sci. Revs. Macromol. Chem. C3, 69-103 (1969).

1.11 I. Havlicek, K. Dusek, Kinetics of curing reaction of epoxy-amine systems in the glass transition region, a theoretical approach. In *Crosslinked Epoxies* (Eds.B. Sedlacek and J. Kahovec), Walter de Gruyter & Co., New York, 417-424 (1987).

1.12 S.L. Simon and J.K. Gillham, Reaction kinetics and TTT cure diagrams for off-stoichiometric ratios of a high-Tg epoxy/amine system, J. Appl. Polym. Sci., 46, 1245-1270 (1992).

1.13 X. Wang and J.K. Gillham, Analysis of crosslinking in amine-cured epoxy systems: The one-to-one relationship between Tg and conversion, J. Appl. Polym. Sci., 45 2127 (1992).

1.14 H.E. Adabbo and R.J.J. Williams, The evolution of thermosetting polymers in a conversion-temperature phase diagram, J. Appl. Polym. Sci., 27, 1327-1334 (1982).

1.15 J.B. Enns, and J.K. Gillham, Time-temperature-transformation (TTT) cure diagram: Modeling the cure behavior of thermosets, J. Appl. Polym. Sci., 28, 2567-2591 (1983).

1.16 J.L. Ricich, J.A. Koutsky, Nodular structure in epoxy resins, J. Appl. Polym. Sci. 20, 2111-2129 (1976).

1.17 K. Dusek, J. Plestil, F. Lednicky, and S. Lunak, Are cured epoxy resins inhomogeneous?, Polym. 19, 393-397 (1978).

1.18 D.R. Uhlmann, Electron microscopy and SAXS studies of amorphous polymers, Faraday Discussions of the Chemical Sciety 68, 87-95 (1979).

1.19 G.C. Stevens , J. V. Champion, P. Liddell, Investigation of local order in unreacted DGEBA epoxy resin monomers by light scattering, J. Polym. Sci. Polym. Phys. Ed. 20, 327-344 (1982).

1.20 E.S-W. Kong, Physical aging in epoxy matrices and composites, Adv. Polym. Sci. 80, 125-171 (1986).

1.21 G. Adam, J.H. Gibbs, On the temperature dependence of cooperative relaxation properties in glass-forming liquids, J. Chem. Phys. 43, 139-146 (1965).

1.22 E. Donth, the size of cooperatively rearranging regions at the glass transition, J. Non-Cryst. Solids 53, 325-330 (1982).

1.23 C.A. Angell, Perspective on the glass transition, J. Phys. Chem. Solid 49, 863-871 (1988).

1.24 T. Kanaya, T. Kawaguchi, and K. Kaji, Fast process of amorphous polystyrene below and above the glass transition temperature Tg as studied by quasielastic neutron scattering, J. Chem. Phys. 104, 3841-3850 (1996).

1.25 T. Kanaya, I. Tsukushi, and K. Kaji, Non-Gaussian parameter and heterogeneity of amorphous polymers, Prog. Theoretical Phys. Suppl. 126, 133-140 (1997).

1.26 C.M. Roland, Constraint on Local segmental motion in poly(vinylethylene) networks, Macromol. 27, 4242-4247 (1994).

1.27 B. Fitz, S. Andjelic, and J. Mijovic, Reorientational dynamics and intermolecular cooperativity of reactive polymers, 1, model epoxy-amine systems, Macromol. 30, 5227-5238 (1997).

1.28 S. Andjelic, B. Fitz, and J. Mijovic, Reorientational dynamics dynamics and intermolecular cooperativity of reactive polymers, 2, multifunctional epoxy-amine systems, Macromol. 30, 5239-5248 (1997).

1.29 D.M. Colucci, G.B. McKenna, Fragility of polymeric liquids: Correlations between thermodynamic and dynamic properties, Mat. Res. Soc. Symp. Proc. 455, 171-176 (1997).

1.30 E. Hempel, G. Hempel. A. Hensel, C. Schick, and E. Donth, Characteristic length of dynamic glass transition near Tg for a wilde assortment of glass forming substances, J. Phys. Chem. B 104, 2460-2466 (2000).

1.31 F. Schwarzl, A.J. Staverman, Mechanical properties of polymers, J. Appl. Phys., 23, 838-843 (1952).

1.32 H. Leaderman, *Elastic and Creep Properties of Filamentous Materials and Other High Polymers*, Textile Foundation, Washington D.C., 175-182 (1943).

1.33 N.G. McCrum, B.E. Read, and G. Williams, *Anelastic and Dielectric Effects in Polymeric Solids*, Wiley, London (1967).

1.34 J.D. Ferry, *Viscoelastic Polymers*, Wiley, New York (1980).

1.35 J.D. Lemay, B.J. Swetlin, and F.N. Kelley, Structure and fracture of highly cross-linked networks, ACS Symp. Series 243, 165-183 (1984).

1.36 M. Shimbo, Basic properties of cured material. In *Handbook of Epoxy Resin* (Ed. M. Shimbo), Nikkan Kogyo Shinbunsha, Tokyo, 299-325 (1987). (in Japanese)

1.37 M. Shimbo, M. Iwakoshi, and M. Ochi, Properteis of cured epoxide resins, The Adhesion Society of Japan 10, 161-168 (1974). (In Japanese)

1.38 M. Simbo, N. Nishitani, T. Takahama, Mechanical properties of acid-cured epoxide resins with different network structures, J. Appl. Polym. Sci. 29, 1709-1721 (1984).

1.39 M. Ogata, T. Kawata, N. Kinjo, Relationship between crosslinking densities and physical properties of phenolic cured epoxides, Japanese J. Polym. Sci. Tech. 44, 193-199 (1987). (In Japanese)

1.40 R.A. Pearson, A.F. Yee, Toughening mechanisms in elastomer-modified epoxies, J. Mater. Sci. 24, 2571-2580 (1989).

1.41 V.T. Truong, Y.B. Truong, and B.C. Ennis, Mechanical properties, fracture toughness and microstructures of a crosslinked epoxy, Polym. Communications 32, 275-278 (1991).

1.42 G. Levita, S.D. Petris, A. Marchetti, and A. Lazzeri, Crosslink density and fracture toughness of epoxy resins, J. Mater. Sci. 26, 2348-2352 (1991).

1.43 A. Murakami, T. Ioku, D. Saunders, H. Aoki, T. Toshiki, S. Murakami, O.Watanabe, M. Saito, and H. Inoue, Fracture behaviour of epoxy resin containing thermoplastics and their composites, Proc. Benibana Int. Symp., 65-71 (1990).

1.44 B.G. Min, J.H. Hodgkin, and Z.H. Stachurski, The dependence of fracture properties on cure temperature in a DGEBA/DDS epoxy system, J. Appl. Poly, Sci. 48, 1303-1312 (1993).

1.45 S.L. Kim, M.D. Skibo, J.A. Manson, R.W. Hertzberg, and J. Haniszewski, Tensile, impact and fatigue behavior of an amine-cured epoxy resin, Polym. Eng. Sci. 18, 1093-1100 (1978).

1.46 J. Mijovic, J.A. Koutsky, Correlation between nodular morphology and fracture properties of cured epoxy resins, Polym. 20, 1095-1107 (1979).

1.47 F.N. Kelley, D.R. Trainor, Model glassy inhomogeneous polymer networks, Polym. Bull. 7, 369-376 (1982).

1.48 F. Bueche, Tensile strength of plastics above the glass temperature, J. Appl. Phys. 26, 1133-1140 (1955).

1.49 M. Kasamori, T. Ohtsuka, M. Shimbo, and Y. Miyano, J. Soc. Mat. Sci., Japan 41, 465-469 (1992). (in Japanese)

1.50 M. Miwa, A. Takeno, T. Yokoi, A. Watanabe, Strain rate and temperature dependence of shear properties of epoxy resin with various molecular weight between cross-linkings, J. Mater. Sci. 34, 5489-5495 (1999).

1.51 S.F. Popelar, M.K. Chengalva, C.H. Popelar, and V.H. Kenner, Accelerated performance evaluation for polyimide films, Time-Dependent Failure of Polymers: Experimental Studies 155, 15-22 (1992).

1.52 Lim, W.W., Mizumachi, H. Fracture toughness of adhesive joints. II. temperature and rate dependencies of mode I fracture toughness and adhesive tensile strength, *J. Appl. Polym. Sci.* 1995, 57, 55-61.

1.53 Han, Y., Yang, Y., Li, B., Wang, X. and Feng, Z. Fracture toughness of phenolphthalein polyether ketone, J. Appl. Polym. Sci., 1995, 57, 655-661.

1.54 R. Frassine, A. Pavan, Viscoelastic effects on the interlaminar fracture behaviour of thermoplastic matrix composites: I. rate and temperature dependence in unidirectional PEI/carbon-fibre laminates, Comp. Sci. Tech. 54, 193-200, (1995).

1.55 F R. Frassine, M. Rink, A. Pavan, Viscoelastic effects on the interlaminar fracture behaviour of thermoplastic matrix composites: II. rate and temperature dependence in unidirectional PEEK/carbon-fibre laminates, Comp. Sci. Tech. 56, 1253-1260 (1996).

1.56 L. Castellani, R. Frassine, A. Pavan, and M. Rink, Rate and temperature dependence of fracture toughness in ABS resins in relation to dispersed-phase structure, Polym. 37, 1329-1338 (1996).

1.57 F. Massa, R. Piques, and A. Laurent, Rapid crack propagation in polyethylene pipe: combined effect of strain rate and temperature on fracture toughness, J. Mater. Sci. 32, 6583-6587 (1997).

1.58 S. Yoneyama, K. Ogawa, A. Misawa, and M. Takashi, Evaluation of time-dependet fracture mechanics parameters of a moving crack in a viscoelastic strip, JSME Int. J. Series A 42, 624-630 (1999).

1.59 T. Adachi, T. Iketaki, M. Gamou, and A. Yamaji, Time-temperature dependence of fracture toughness of silica particulate-filled epoxy composite, Proc. the Fourth Int. Cong. on Thermal Stresses, 65-68 (2001).

1.60 T. ADACHI, M. OSAKI, A. YAMAJI, and M. GAMOU, Time-temperature dependence of the fracture toughness of a poly (phenylene sulphide) Polymer, Proc. Inst. Mech. Eng. Pt L, J. Mater.: Design and Appl. 217, 29-34 (2003).

1.61 R. Fracasso, M. Rink, A. Pavan, and R. Frassine, The effect of strain-rate and temperature on the interlaminar fracture toughness of interleaved PEEK/CF composites, Comp. Sci. Tech. 61, 57-63 (2001).

1.62 D.J. Plazek, I.C. Choy, F.N. Kelley, E. Meerwall, and L.J. Suş, Viscoelasticity and tearing energy of fluorinated hydrocarbon elastomers, Rubber Chem. Tech. 56, 866-882 (1982).

1.63 Plazek, D.J., Choy, I.C., The physical properties of bisphenol-A-based epoxy resins during and afrer curing. II., creep behavior above and below the glass transition temperature, J. Polym. Sci. Pt. B 27, 307-324 (1989).

1.64 Y. Miyano, M.K. McMurray, N. Kitade, M. Nakada, and M. Mohri, Loading rate and temperature dependence of flexural behaviour of unidirectional pitch-based CFRP laminates, Comp. 26, 713-717 (1995).

1.65 T.G. Rogers, E.H. Lee, The cylinder problem in viscoelastic stress analysis, Quaterly of Appl. Math. 22, 117-120 (1964).

1.66 E.C. Ting, Stress analysis for linear viscoelastic cylinder, *AIAA* J. 8, 18-22 (1969).

1.67 L.W. Morland, E.H. Lee, Stress Analysis for Linear Viscoelastic materials with temperature variation, Trans. Soc. Rheol. 4, 233-263 (1960).

1.68 R. Muki, E. Sternberg, On Transient thermal stresses in viscoelastic materials with temperature-dependent properties, Trans. ASME. J. Appl. Mech. 28, 193-207 (1961).

1.69 R.A. Schapery, A theory of crack initiation and growth in viscoelastic media – Parts I, Int. J. Frac. 11, 141-159 (1975).

1.70 R.A. Schapery, A theory of crack initiation and growth in viscoelastic media – Parts II, Int. J. Frac. 11, 369-388 (1975).

1.71 R.A. Schapery, A theory of crack initiation and growth in viscoelastic media – Parts III, Int. J. Frac. 11 ,549-562 (1975).

1.72 R.M. Christensen, A rate-dependent criterion for crack growth, Int. J. Frac. 15, 3-21(1979).

1.73 R.M. Christensen, E.M. Wu, A theory of crack growth in viscoelastic materials, Eng. Frac. Mech. 14, 215-225 (1981).

1.74 R. Frassine and A. Pavan, An application of viscoelastic fracture criteria to steady crack propagation in a polymeric material under fixed deformation, Int. J. Frac. 43, 303-317 (1990).

1.75 J.R. Masuero and G.J. Creus, Finite elements analysis of viscoelastic fracture, Int. J. Frac. 60, 267-282 (1993).

1.76 D. Gamby and J. Chaoufi, Application of viscoelastic fracture criteria to progressive crack propagation in polymer matrix composites, Int. J. Frac. 100, 379-399 (1999).

1.77 F. Dubois, C. Chazal, and C. Petit, Viscoelastic crack growth process in wood timbers: An approach by the finite element method for mode I fracture, Int. J. Frac. 113, 367-388 (2002).

1.78 J.A.F. Harvey and D. Cebon, Failure mechanisms in viscoelastic films, J. Mater. Sci. 38, 1021-1032 (2003).

Chapter 2

Mode I fracture toughness at room temperature

2.1 INTRODUCTION

Network morphology of epoxy resins depends on used material types of epoxide resin and curing agent, their combination, and curing conditions. Mechanical properties of cured epoxy resins and their composites are governed by the network morphology.

In general, a degree of the curing reaction is used for estimating the network morphology, and it is well known that the mechanical properties such as Young's modulus, yield stress and so on depend on the cross-linking degree.[2.1-2.5] As for fracture properties, however, different relationships between the cross-linking degree and the fracture properties of epoxy resins have been reported.[2.6-2.11] This means that the cross-linking density is not always a strongly determining factor for fracture properties. An alternative parameter for setting the curing conditions, thus, is needed to estimate the fracture property.

The purpose of the present chapter is to clarify the effect of the morphology on the fracture toughness of a bisphenol-A type epoxy resin and silica particulate-filled epoxy composite, using glass transition temperature, T_g, and a fragility parameter, m. The former is closely related to the degree of the cross-linking reaction.[2-12-2.24] The latter is proposed by Angell[2.25] as a basis for classifying of supercooled materials according to the variations in their dynamic properties at temperature above T_g, based on the concept of intermolecular

cooperativity. Also it has attracted much attention as a parameter related to the density heterogeneity of thermoplastic resins.[2.26,2.27] The fragility parameter of the concept of cooperativity has been also applied to cross-linked polymers,[2.28-2.32] which have a heterogeneous microstructure.[2.13, 2.33-2.38]

First, we derive the parameters, T_g and m, from the thermo-viscoelasticity in order to characterize the epoxy resins and composites cured under various conditions. Also the specimens are examined using a laser Raman spectrophotometer. Then, a mode I fracture toughness, K_{Ic}, is measured at room temperature, and fracture surfaces are observed with a differential interference microscope, an atomic force microscope, and a scanning electron microscope. The relationships between T_g, m, and K_{Ic} are discussed based on the results of these observation.

2.2 EXPERIMENTAL PROCEDURE

2.2.1 Specimen

The epoxy resin used in the experiment was a blend of bisphenol-A type epoxide resin (Epikote 828, Japan Epoxy Resin) with 3,4-metyl-1,2,3,6-tetrahydro-phthalic anhydride as a curing agent (HN-2200R, Hitachi Chemical) and 2-4-6 tris (dimethylaminomethyl) phenol as an accelerator (Daitocurar HD-Acc43, Daito Sangyo). The weight ratio of the resin, the curing agent and the accelerator was 100:80:0.5. The filler was fused silica particle (Fuselex ZA-30, Tatsumori), with an average diameter of 5.5 μm. The volume fractions of the silica particles were 0 % (Epoxy), 26 % (Composite A), 35 % (Composite B), and 42 % (Composite C).

The raw material mixture was cast in an aluminum mold coated with a Teflon sheet. After it was agitated and degassed in vacuum, then cured in a thermostatic oven. The dimensions of the mold in length, width, and depth were 260, 5, and 180 mm, respectively.

The curing was performed in two steps: pre-curing for gelation, post-curing for promotion of the cross-linking reaction. A preparatory experiment demonstrated that the pre-curing conditions negligibly affect the mechanical properties of the cured material. The specimens were thus made under fixed pre-curing conditions, at 353 K for 3 hours, and under various post-curing conditions, at 353 to 433 K for 3 to 15 hours, as summarized in Table 2.1. The heating rate from pre-curing to post-curing was a constant 72 K/h for each process.

2.2.2 Thermo-viscoelasticity measurement

The thermo-viscoelastic properties of the cured epoxy resins and composites were examined with a dynamic viscoelastometer (Rheovibron DDV-III-EA, Orientec). Tensile vibrations at 3.5, 11, 35, and 110 Hz were applied to the specimen every 2 K from 123 to 523 K to measure dynamic storage and loss moduli, E' and E''. The specimens were 90 mm long, 5 mm wide, and 3 mm thick. The span length was 70 mm long.

Epoxy resin and its composite are known as thermo-viscoelastic materials that depend on both temperature and time. Their master curves of E' were made from the temperature dependence curves of E' shifted along the frequency axis according to the temperature-time equivalence principle[2.39] with a shift factor, a_T.

2.2.3 Raman spectroscopic analysis

A laser micro-Raman spectrometer (NRS-1000, JASCO) was used at room temperature (293 K) to determine the cross-linking degree of the specimens. The epoxy specimens and the epoxy resin matrix of the composites were examined with a space resolution of 2 μm. A green laser with wavelength 532.3 nm and power 100 mW were used, and a spectral slit was 40 μm wide. The exposure time was 420 s for the epoxy resins and 600 s for the composites. The specimens were less than 500 μm thick and their surfaces were polished smoothly in order to reduce background stray light.

2.2.4 Mode I fracture toughness test

A tensile test of a double edge-cracked plate was performed to measure the mode I fracture toughness. The specimens were 250 mm long, 25 mm wide, and 5 mm thick. Pre-cracks, 5 mm long, were induced on both sides of the middle position of the specimen. The test was carried out at a deformation rate of 2 μm/s and a temperature of 293 K with a universal material testing machine (8501, Instron).

The load-deformation curve of each specimen was linear until brittle breaking occurred, meaning that the stress field near the crack tip was small scale yielding. Therefore, the method of linear elastic fracture mechanics could be applied to the experimental results to determine the fracture toughness. A mode I stress intensity factor, K_I, is given by:[2.40]

$$K_I = \frac{P}{BW}\sqrt{\pi a}\cdot f(\varsigma), \qquad (2.1)$$

where

$$f(\varsigma) = \frac{1.122 - 0.561\varsigma - 0.205\varsigma^2 + 0.471\varsigma^3 - 0.190\varsigma^4}{\sqrt{1-\varsigma}}, \quad \varsigma = \frac{2a}{W}.$$

The P, W, B, and a are the load, width, thickness, and crack length. Substituting of the maximum load P_{max} into P in Eq. (2.1), I can determine a mode I fracture toughness, K_{Ic}. I took the average value of five results as K_{Ic} for each specimen.

2.2.5 Fractographic analysis

After the fracture toughness test, I observed the fractured surface to evaluate the microstructure of the specimens visually and quantitatively.

For the epoxy resin, the overall fractured surface was observed with a differential interference microscope. And also, the surfaces were finely investigated with an atomic force microscope (SPI3800, Seiko Instruments). Then an average surface roughness, R_a, was estimated to quantify the microscopic observation of the fractured surfaces. It was defined similar to that in JIS B0601 (1994):

$$R_a = \frac{1}{S_0}\int_{S_0} |z|\, dS\,, \tag{2.2}$$

where S and S_0 are the actual surface area and the area projected from the actual surface to the flat plane; z denotes the distance from the projected plane to the actual surface. The R_a was estimated in an area 5 μm × 5 μm, which is sufficiently large to determine the microscopic roughness of the fractured surface.

For the observation of the fractured surfaces of the composites, a scanning electron microscope (JSM-T200, JOEL) was used at an accelerating voltage of 5 kV.

2.3 PARAMETERS CHARACTERIZING NETWORK MORPHOLOGY

The glass transition temperature, T_g, increases monotonically with the cross-linking degree until the reaction saturates.[2.17, 2.24, 2.34] The fragility parameter, m, suggested by Angell,[2.25] has attracted much attention as a parameter related to the density heterogeneity of resins. Thus, T_g and m were used to classify the epoxy resins and its composites post-cured under various conditions. These parameters were obtained from the measured thermo-viscoelasticity as follows.

The temperature at the maximum value of the *apparent* thermal activation energy, given by an Arrhenius plot of a_T, was defined as T_g.

By definition, m is obtained from the slope at T_g of the viscosity or the relaxation time in an Arrhenius plot, where the abscissa is scaled to T_g of the material. Böhmer et al. expressed m as:[2.41]

$$m = \frac{\mathrm{d}(\log\tau)}{\mathrm{d}(T_g/T)} \quad \text{at } T = T_g\,, \tag{2.3}$$

where τ and T are the relaxation time and absolute temperature, respectively. Epoxy resin and its composite have been experimentally shown to be a themorheologically simple material,[2.42-2.44] so that a_T can be expressed as:[2.45]

$$a_T = \frac{\tau(T)}{\tau(T_R)}\,, \tag{2.4}$$

where T_R is a standard temperature. Substitution of Eq. (2.4) into Eq. (2.3) enables m to be expressed using a_T:

$$m = \frac{d(\log a_T)}{d(T_g / T)} \quad \text{at } T = T_g . \tag{2.5}$$

Hence, m can be derived from the slope of a_T, with the reciprocal of the temperature normalized by T_g, which is essentially equal to the *apparent* activation energy.

Table 2.1 Epoxy and composite specimens (Continued)

(a) Epoxy (Volume fraction of particle: 0%)

Post-curing temp (K)	Post-curing time (h)	Glass transition temperature (K)	Fragility
353	3	343	75
353	9	373	54
353	15	373	49
373	3	377	57
373	9	399	97
373	15	399	62
393	3	387	97
393	9	413	103
393	15	407	53
413	3	389	58
413	9	413	90
413	15	411	46
433	3	391	177
433	9	415	101
433	15	405	53

Table 2.1 Epoxy and composite specimens

(b) Composite A (Volume fraction of particle: 26%)

Post-curing temp (K)	temp (K)	Glass transition temperature (K)	Fragility
353	3	341	117
373	3	395	108
393	3	397	121
413	15	413	107
433	3	411	106

(c) Composite B (Volume fraction of particle: 35%)

Post-curing temp (K)	temp (K)	Glass transition temperature (K)	Fragility
353	3	351	58
373	3	395	65
393	3	407	80
413	15	413	97
433	3	405	73

(d) Composite C (Volume fraction of particle: 42%)

Post-curing temp (K)	temp (K)	Glass transition temperature (K)	Fragility
373	3	391	41
393	3	409	42
413	15	409	54
433	3	411	48

2.4 RESULTS AND DISCUSSION

2.4.1 Thermo-viscoelasticity

Typical temperature dependences of the dynamic moduli, E' and E'', measured at 3.5 Hz are shown in Fig. 2.1. Also typical temperature dependences of E' with various frequencies are shown in Fig. 2.2. It was clearly seen that E' and E'' of every specimen depend on both the temperature and the frequency. Then, the master curves of E' and E'' and the shift factors, a_T, were derived for each specimen with time-temperature equivalence principle. Typical master curve of E', which were derived from Fig. 2.2, is shown in Fig. 2.3. And typical shift factors, a_T, with reciprocal of T normalized T_g at the standard temperature $T_R = T_g$ is shown in Fig. 2.4. The slope of a_T at T_g in Fig. 2.4 represents the fragility, m.

2.4.2 Glass transition temperature and fragility

The T_g and m for each specimen are summarized in Table 2.1. The relationship between T_g, m, and the post-curing condition is shown in Fig. 2.5. The T_g of the epoxy resins and composites increased as the post-curing temperature and time increased. It approached to approximately 400 K when the post-curing temperature was more than 400 K. The m of each epoxy resins was low, about 50, after being post-cured for 15 hours at every post-curing temperature. The m of the composites strongly depended on the volume fraction of silica particles. There was no direct correlation between T_g and m for any specimen; in particular m of the epoxy resins varied considerably even after T_g saturated at approximately 400 K.

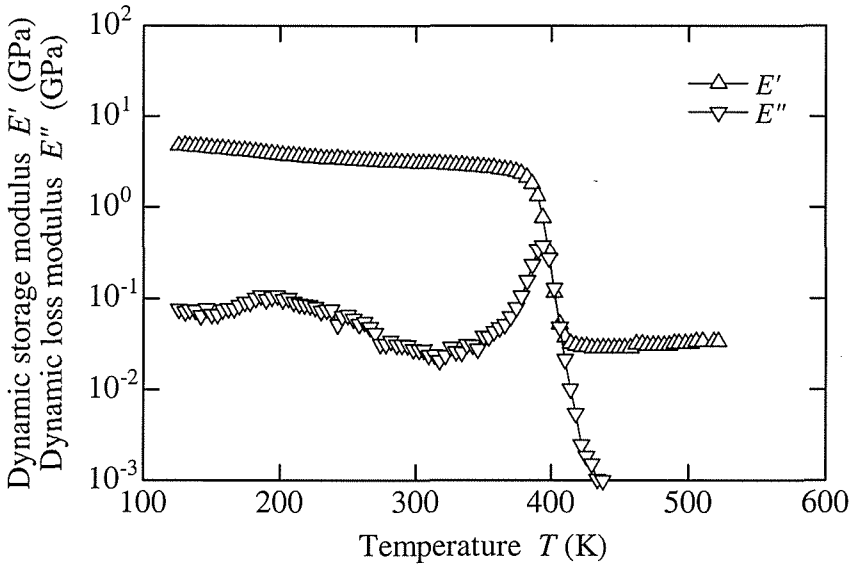

(a) Epoxy

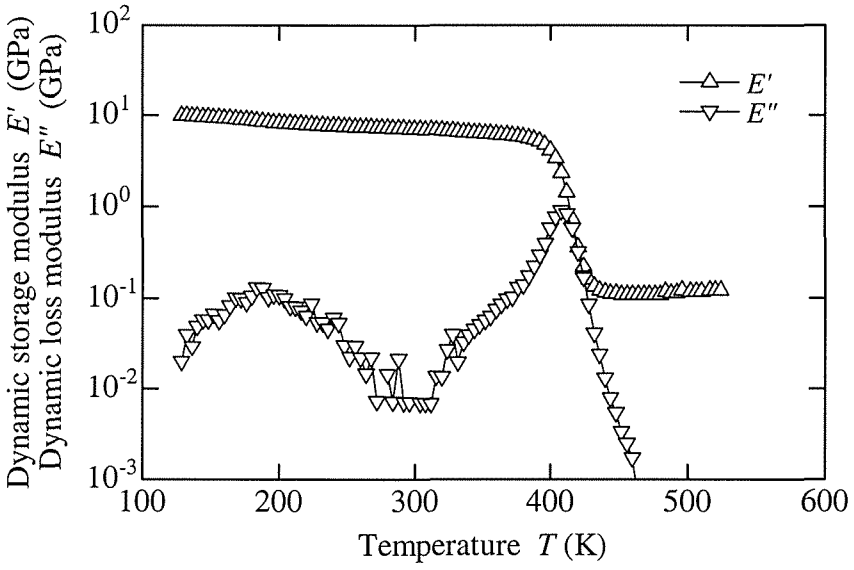

(b) Composite A

Figure 2.1 Dynamic moduli
(Post-curing condition is 433 K - 3 h; Measuring frequency is 3.5 Hz.)

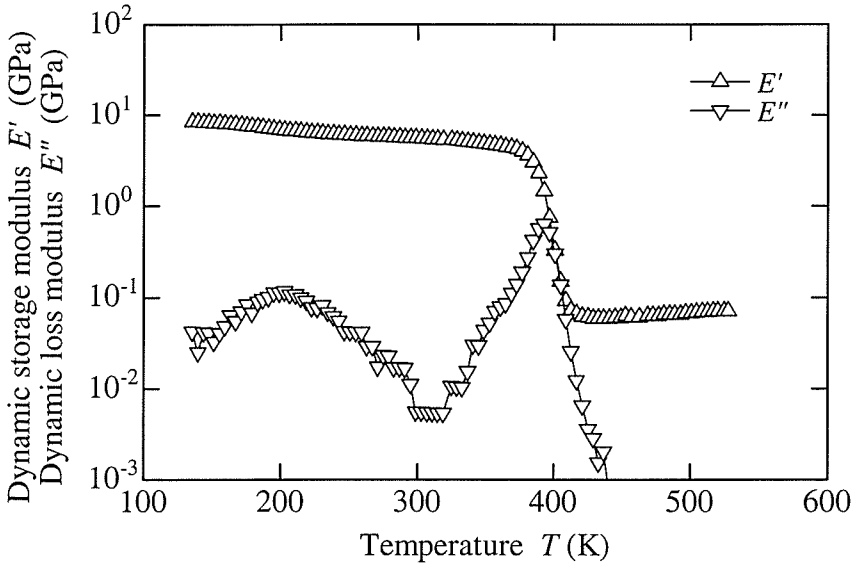

(c) Composite B

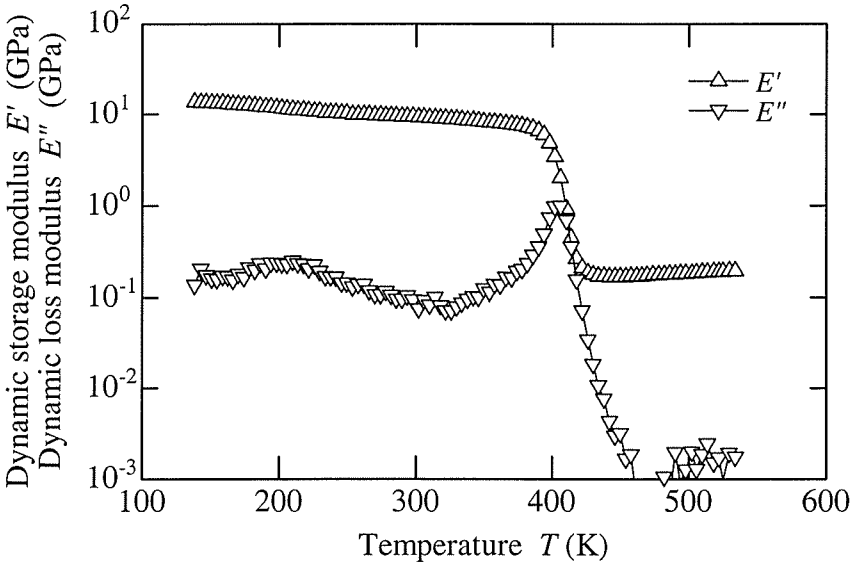

(d) Composite C

Figure 2.1 Dynamic moduli
(Post-curing condition is 433 K - 3 h; Measuring frequency is 3.5 Hz.)

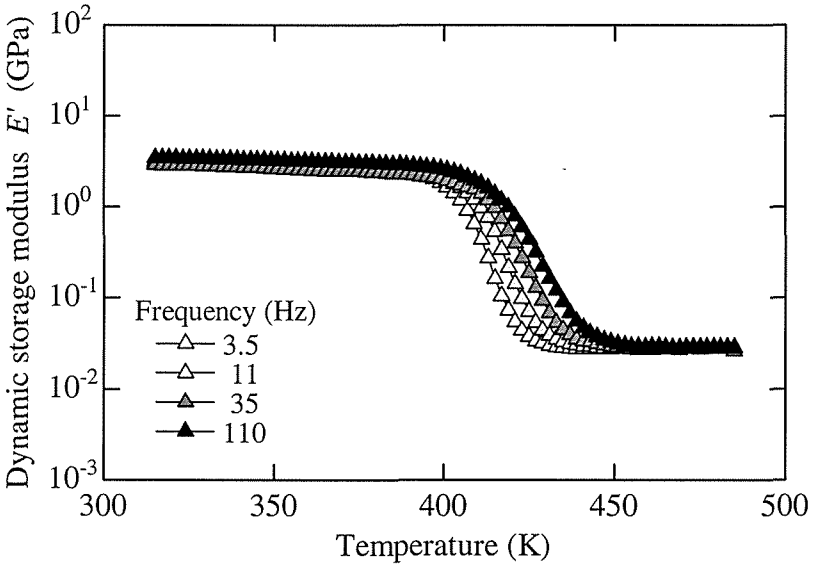

Figure 2.2 Dynamic storage modulus
(Epoxy. Post-curing condition is 393 K - 15 h.)

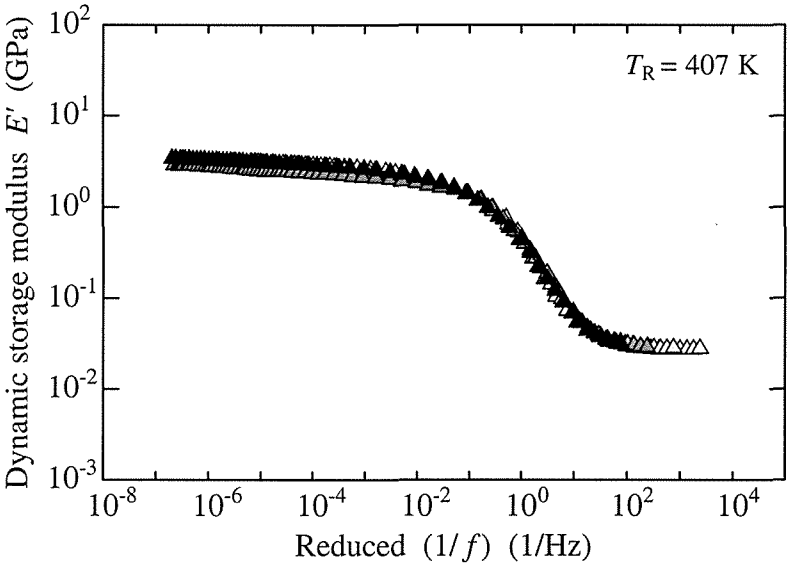

Figure 2.3 Master curve of dynamic storage modulus
(Epoxy. Post-curing condition is 393 K - 15 h.)

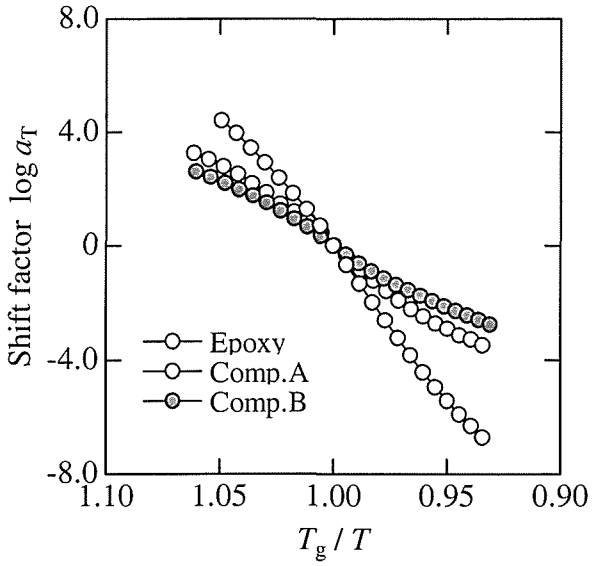

(a) Post-cured at 353 K for 3 h

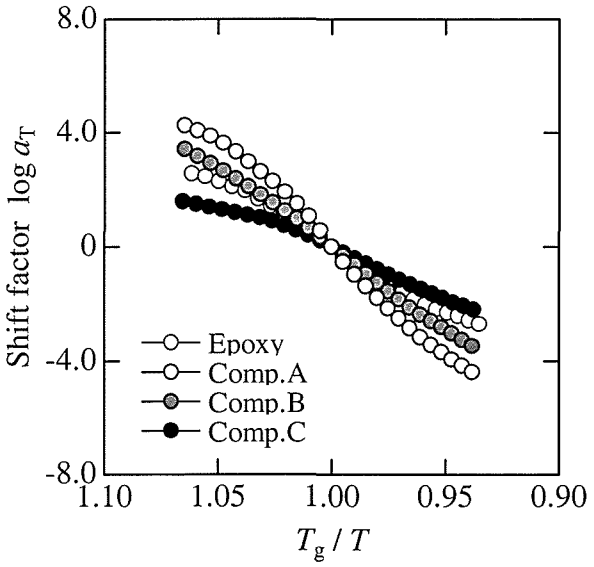

(b) Post-cured at 373 K for 3 h

Figure 2.4 Shift factor
(Standard temperature is glass transition temperature.) (Continued)

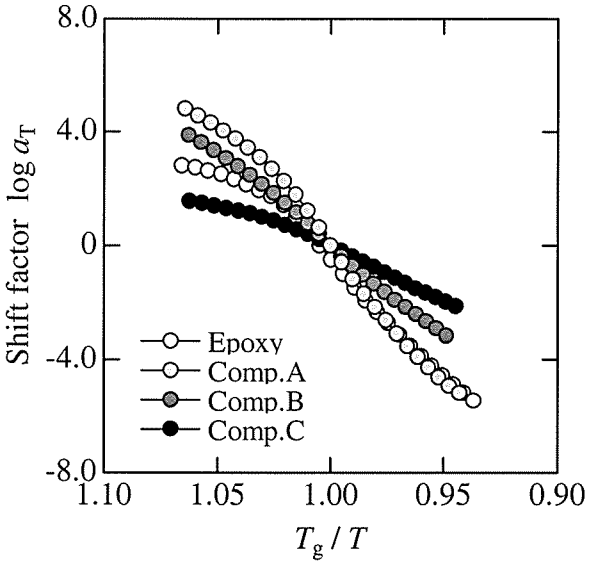

(c) Post-cured at 393 K for 3 h

Figure 2.4 Shift factor
(Standard temperature is glass transition temperature.)

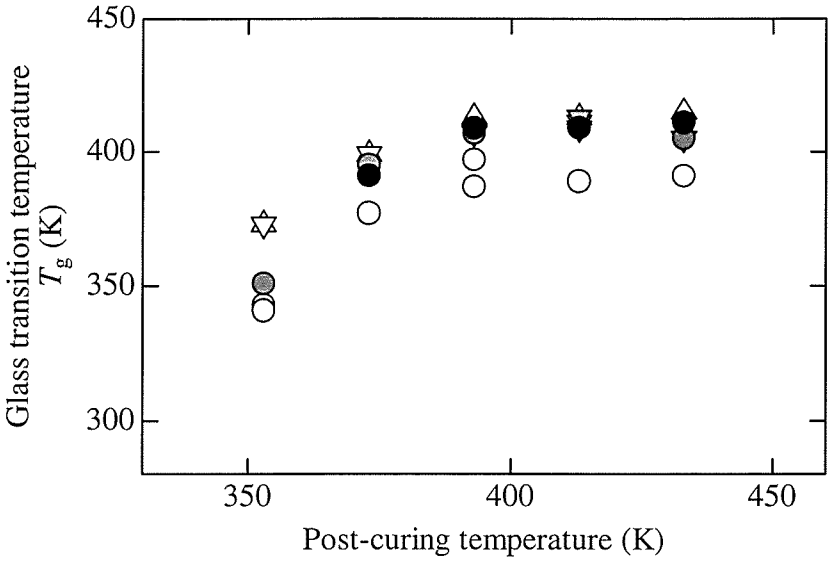

(a) Glass transition temperature

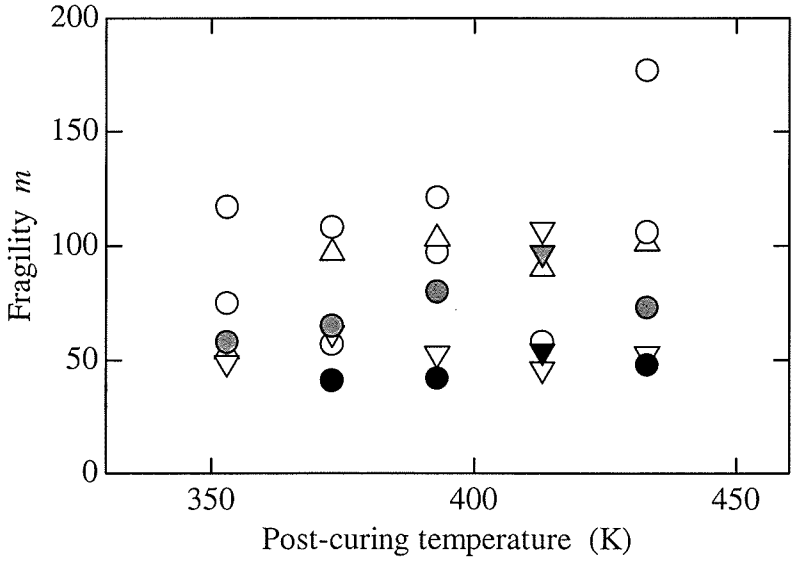

(b) Fragility

Figure 2.5 Parameters characterizing network morphology
(Post-curing time (h): Epoxy ○ 3, △ 9, ▽ 15;
CompA ○ 3, ▽ 15; CompB ◍ 3, ▼ 15; CompC ● 3, ▼ 15)

2.4.3 Raman spectroscopic analysis

Figure 2.6 shows typical Raman spectra of the biphenol-A type epoxide resin (DGEBA), the epoxy resin and the epoxy resin matrix of the composites for the 600-1800 cm^{-1} spectral region. All the specimens had common spectral features in the range 300-4000cm^{-1}. The Raman spectra at about 2800-3200cm^{-1} and 1500-1800cm^{-1} are attributed to CH and CH_2 stretching, CH_2 deformation vibration, respectively.[2.46-2.48] The peaks at 1123 and 1196 cm^{-1} are associated with bisphenol-A backbone vibrations.[2.48-2.50] The bands at 835, 927, and 1256 cm^{-1} are associated with the epoxide ring vibration (denoted by black triangles in Fig. 2.6). The intensity of these bands decreases as the cross-linking reaction proceeds.[2.49,2.50] The intensity of the 1256 cm^{-1} band, I_{epo}, was used to determine the cross-linking degree of the specimens. And the intensity of the 1186 cm^{-1} band, I_{ref}, was chosen as an internal standard because the bands associated with the bisphenol-A backbone do not depend on the curing reaction.

The relationship between the normalized intensity of the epoxide ring, I_{epo}/ I_{ref}, and T_g is shown in Fig. 2.7(a). The cross-linking degrees of the epoxy resins and the matrix of the composites had a good correlation with the T_g of them. These results show that the T_g derived from the thermo-viscoelasticity expresses the cross-linking degree of the epoxy resin and the matrix resin of the composite, and that the T_g of the composite primarily depends on the thermo-viscoelastic property of the matrix resin. In contrast, the m of the specimens did not have any relation to the cross-linking reaction as shown in Fig. 2.7(b). therefore it is possible that the m is due to a physical structure.

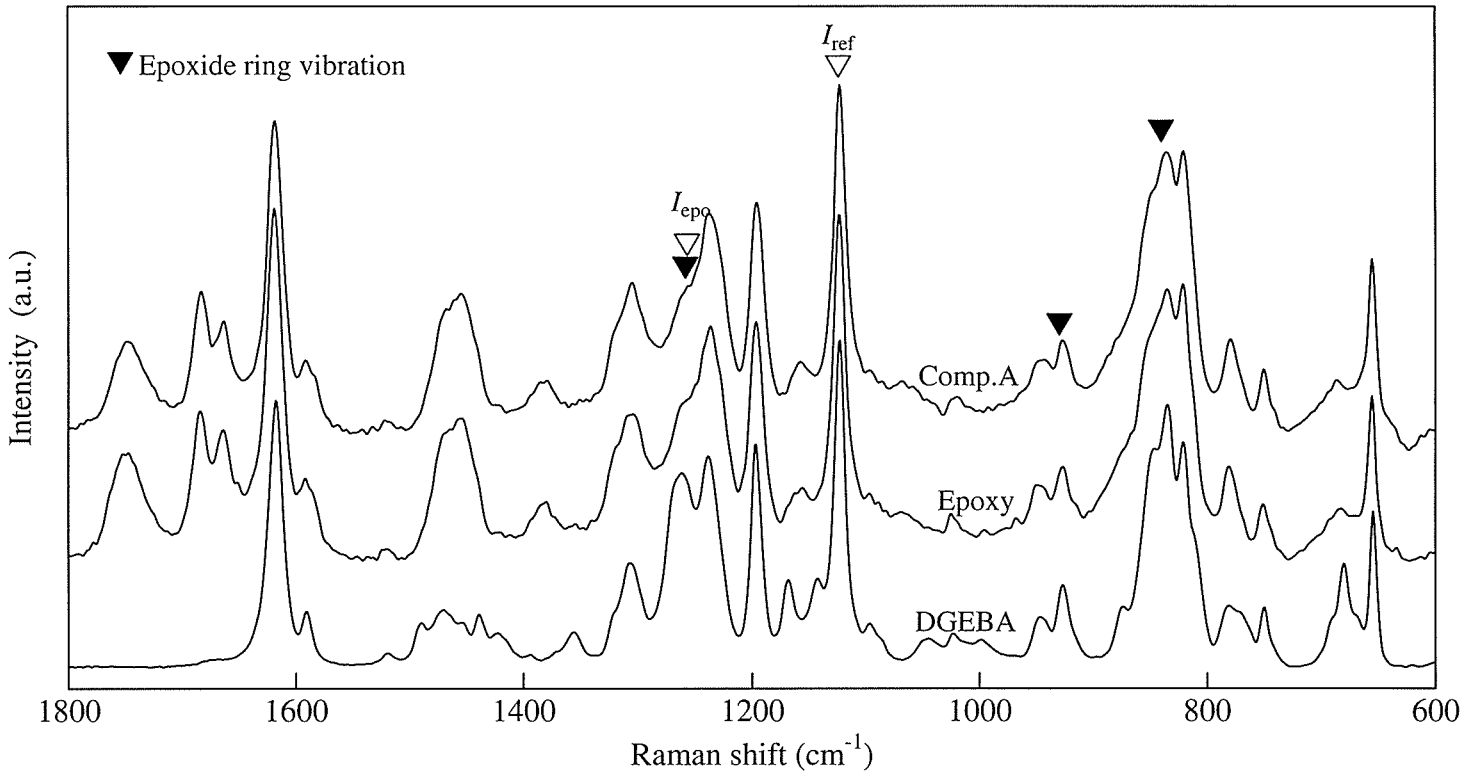

Figure 2.6 Raman spectra

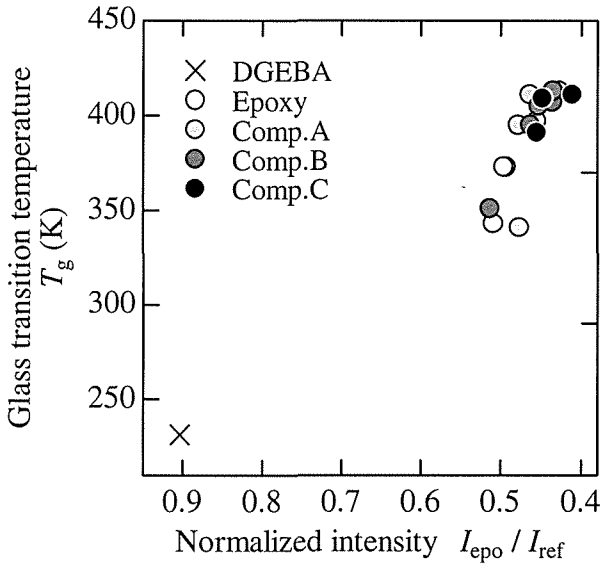

(a) Glass transition temperature

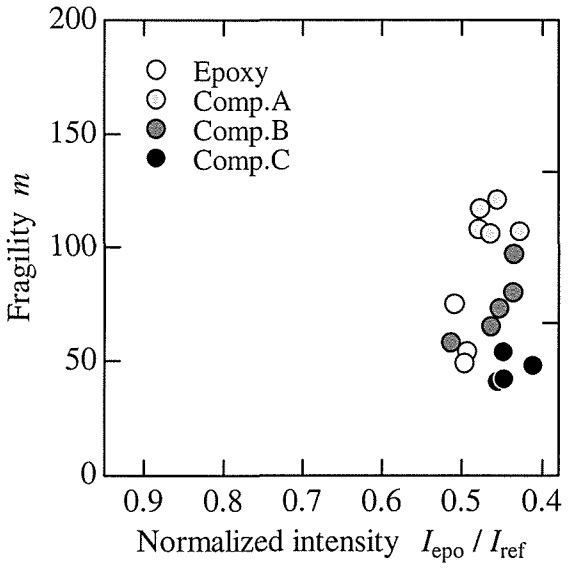

(b) Fragility

Figure 2.7 Cross-linking degree

2.4.4 Mode I fracture toughness

The relationship between T_g, m and K_{Ic} is shown in Fig. 2.8. Figure 2.8(a) shows that K_{Ic} of each composite increased with T_g, although that of the epoxy resin was not directly related to it. For example, K_{Ic} of Composites A increased from 1.1 to 1.6 MPa$\cdot$m$^{1/2}$ as T_g increased from 340 to 410 K, while that of the epoxy resins varied from 0.6 to 1.1 MPa$\cdot$m$^{1/2}$ even when T_g were approximately the same. Figure 2.8(b) shows that K_{Ic} of the epoxy resin depended on m when T_g was saturated at approximately 400 K. As the m decreased from 180 to 50 when T_g was about 400 K, K_{Ic} of the epoxy increased from 0.6 to 1.1 MPa$\cdot$m$^{1/2}$. Comparison of the three kinds of composites demonstrated that K_{Ic} of Composites C, which generally had a higher volume fraction and lower m than the other composites, showed a higher value.

2.4.5 Fractography for epoxy resin

Figure 2.9 shows the appearance of typical surfaces of general surfaces of the epoxy resins observed using the differential interference microscope. These specimens had approximately the same T_g of 400 K, but different values of m. The specimens both had a smooth, mirror-like surface near the initial crack tip. As the crack propagated, small pits began to appear on the surface and developed into parabolic patterns, so that the surface gradually became rough. As the crack propagates further, the parabolic patterns are superposed on each other and the surface became rougher. The source of the parabolic pattern, which is obviously the pits, greatly depended on the microstructure of the epoxy resin. The region where the pits appeared was finely observed using the atomic force microscope and the results were quantified using the average surface roughness, R_a. Typical images are shown in Fig. 2.10, and the relationship between R_a and T_g is shown in Fig. 2.11(a). Even though T_g was approximately the same, R_a varied from 5 to 13 nm; i.e., there was no correlation between R_a and T_g. This is probably because T_g is the parameter used to express the average cross-linking degree of the cured epoxy resin. The relationship between R_a and m is shown in Fig. 2.11(b). R_a decreased as m increased at constant T_g.

The morphology of fractured surface is related to network heterogeneity on a scale of several nm to μm in cross-linked resins,[2.13, 2.33-2.38] and this heterogeneity affects the fracture property.[2.51-2.53] Kanaya et al.[2.26,2.27] reported that m expresses the density heterogeneity of the thermoplastic resins. Previous research and our experimental results, therefore, suggest that m expresses the density heterogeneity of cross-linking in the epoxy resin. This hypothesis explains well the relationship between K_{Ic} and m of the epoxy resin shown in Fig. 2.8(b).

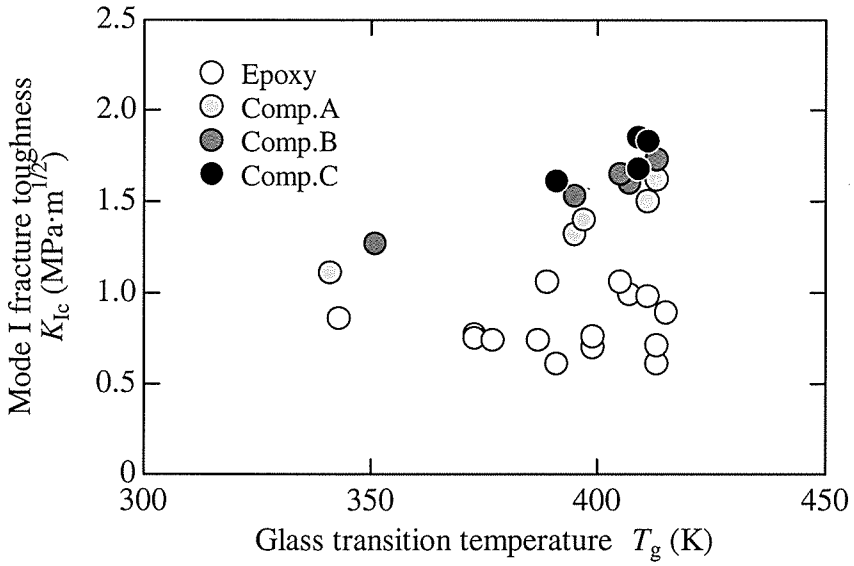

(a) Glass transition temperature

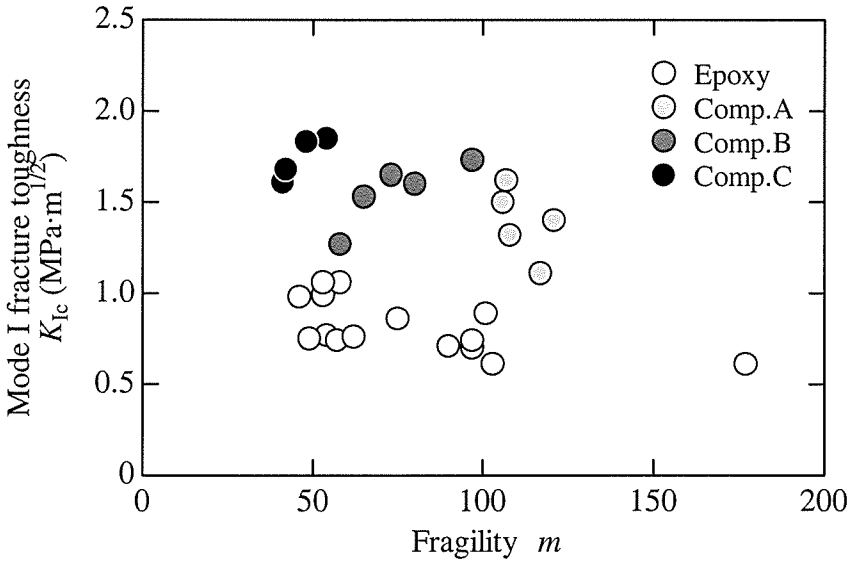

(b) Fragility

Figure 2.8 Mode I fracture toughness at room temperature.

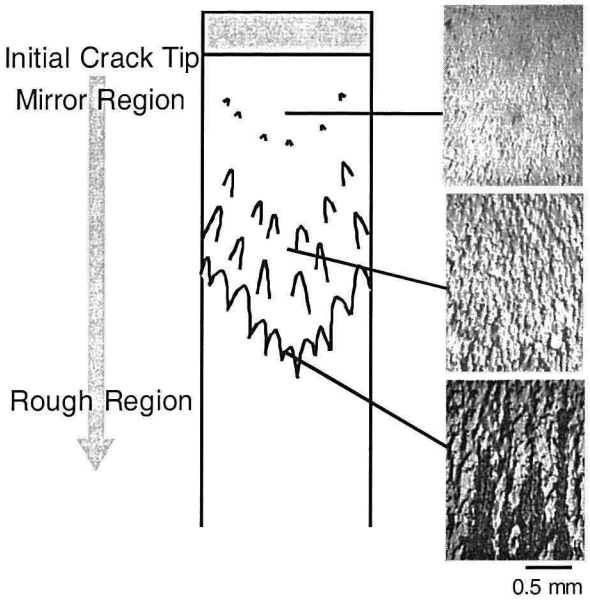

(a) Post-curing condition 393 K, 15 h ($T_g = 407$ K, $m = 53$)

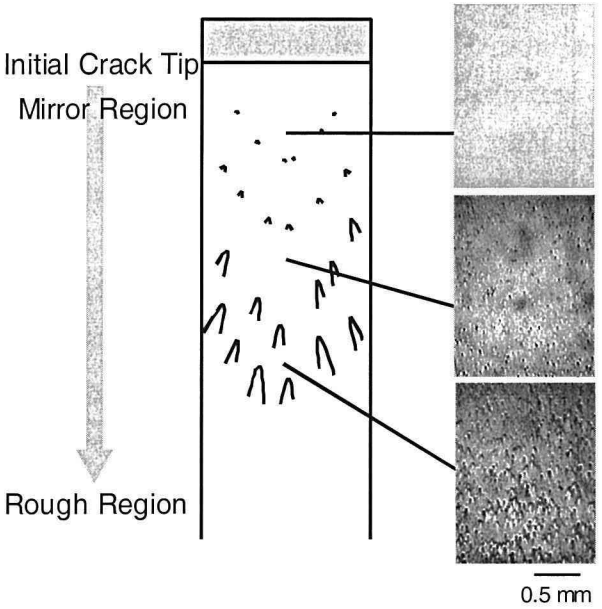

(b) Post-curing condition 413 K, 9 h ($T_g = 413$ K, $m = 90$)

Figure 2.9 Fracture surface of epoxy resin observed by differential interference microscope

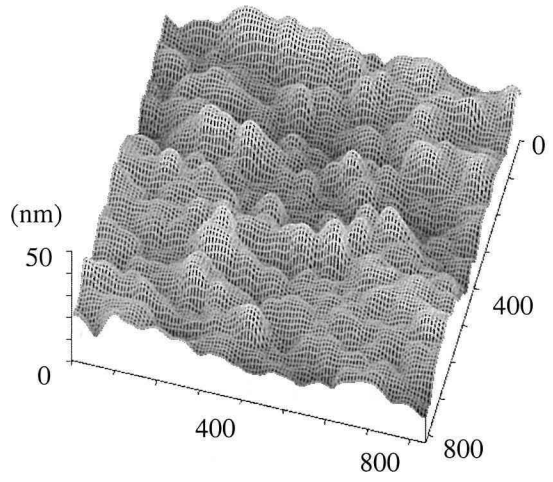

(a) Post-curing condition 393 K, 15 h ($T_g = 407$ K, $m = 53$)

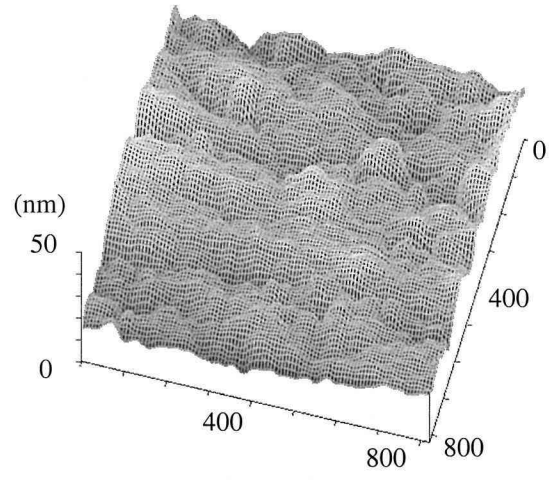

(b) Post-curing condition 413 K, 9 h ($T_g = 413$ K, $m = 90$)

Figure 2.10 Fracture surface of epoxy resin observed by atomic force microscope

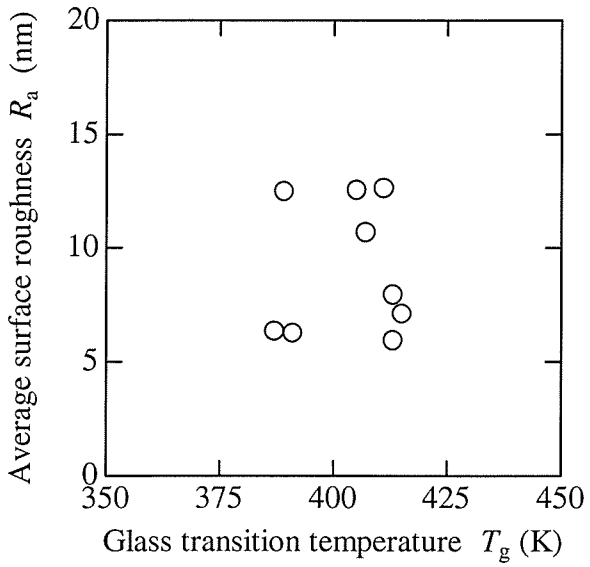

(a) Glass transition temperature

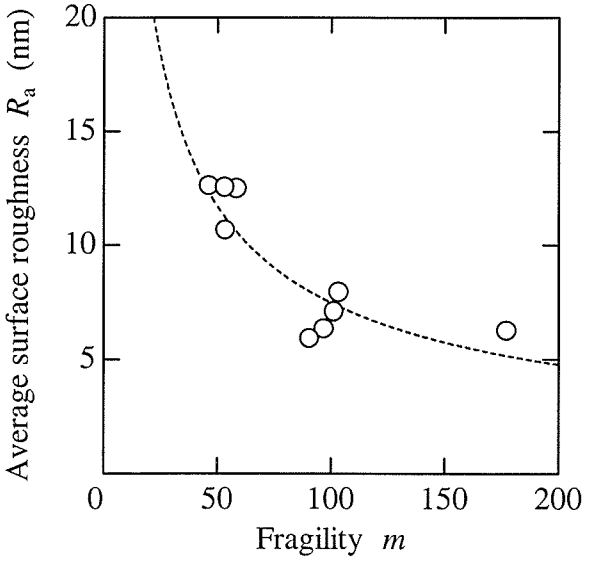

(b) Fragility

Figure 2.11 Average surface roughness

2.4.6 Fractography for composite

Figure 2.12 shows typical surfaces of the epoxy composites observed using the scanning electron microscope. The fracture surface of the composite was mostly rough due to many steps compared with that of the epoxy resin. Such steps have been attributed to silica particles and the interpaticle spacing, and the creation of the steps requires energy to form the fracture surface. The specimens shown in Fig. 2.12(a)~(c) had the same volume fraction but different T_g values. The number of the steps increased with increasing T_g, when the volume fraction was the same. The steps of the composite were strongly influenced by the filled particles when the cross-linking reaction of the matrix had sufficiently proceeded. The specimens shown in Fig. 2.12(c)~(e) had approximately the same T_g but different volume fractions. The number of steps increased with increasing volume fraction when T_g was almost the same. This is because the composite with a high volume fraction had a small interparticle spacing. Since the composites with a high T_g and high volume fraction, such as Composite C cured at 413 K for 15 h, had many steps on their fracture surface, they had high K_{Ic}.

2.4.7 Discussion

These experimental results showed that the epoxy resins have a high K_{Ic} when T_g is about 400 K and a low m. The K_{Ic} of the epoxy resin increases with the increaseing heterogeneity of the microstructure, when the cross-linking reaction has almost finished. The results also indicate that the epoxy composites with a high T_g and low m have a high K_{Ic}. The m of the composite depended on the volume fraction of the silica particles, because the viscosity of the composite may be mainly dominated by not the matrix resin but the interaction between the matrix and the particles, which primarily depends on the volume fraction. The filling of the particles increased the energy required to form the fracture surface, so the K_{Ic} increases with decreasing m. When the volume fraction was constant, a change in the interaction, following the proceeding of the cross-linking reaction in the matrix, may greatly affect the fracture properties.

2.5 CONCLUSION

In the present chapter, I discussed the relationships between the network morphology and the mode I fracture toughness, K_{Ic}, at room temperature for bisphenol-A type epoxy resins and silica particulate-filled epoxy composites. The glass transition temperature, T_g, and the fragility parameter, m, derived from the thermo-viscoelasticity were used in order to characterize the epoxy resins and the composites post-cured under various conditions and different volume fractions of silica particles.

Raman spectroscopic analysis proved that T_g expresses the degree of the cross-linking reaction of the epoxy resins and the matrix resins in the composites. The fractography results

showed that m of the epoxy resin depends on the heterogeneous microstructure but that m of the composite was dominated by the volume fraction of the silica particle. The K_{Ic} of the epoxy resins increased as m decreased when T_g saturated at approximately 400 K. The K_{Ic} of the composites with a high T_g and low m was high. For the epoxy resins and the composites, therefore, the specimen with higher T_g and also lower m has a higher K_{Ic} value. I conclude, based on the experimental results, that T_g and m are very useful for characterizing these materials and estimating mode I fracture toughness at the room temperature.

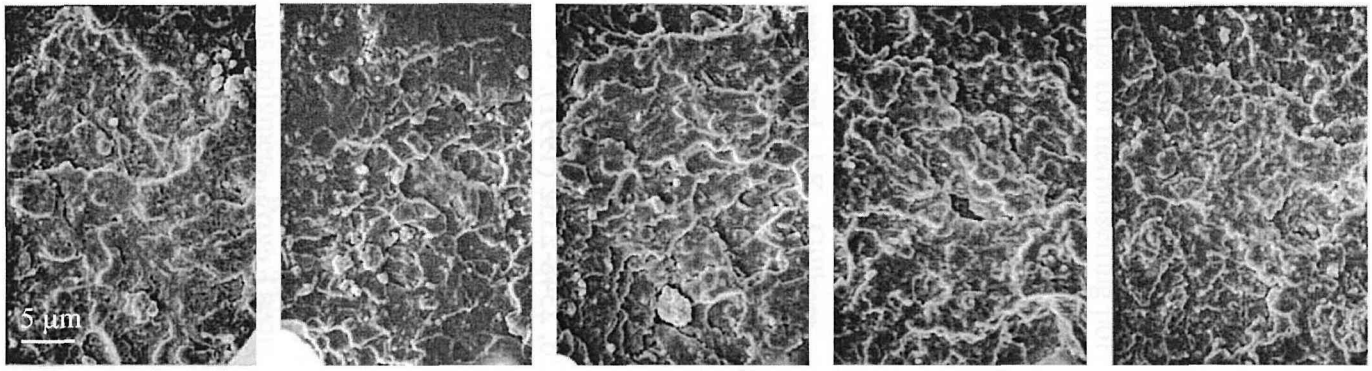

(a) Comp.A	(b) Comp.A	(c) Comp.A	(d) Comp.B	(e) Comp.C
PC : 353K, 3h	PC: 393 K, 3 h	PC: 413 K, 15 h	PC: 413 K, 15 h	PC: 413 K, 15h
T_g: 341 K	T_g: 397 K	T_g: 413 K	T_g: 413 K	T_g: 409 K
m: 117	m: 121	m: 107	m: 97	m: 54
K_{Ic}: 1.11 MPa·m$^{1/2}$	K_{Ic}: 1.40 MPa·m$^{1/2}$	K_{Ic}: 1.62 MPa·m$^{1/2}$	K_{Ic}: 1.73 MPa·m$^{1/2}$	K_{Ic}: 1.85 MPa·m$^{1/2}$

Figure 2.12 Fracture surface of epoxy composite observed by scanning electron microscope (PC means post-curing condition.)

REFERENCES

2.1 M. Shimbo, M. Iwakoshi, and K. Ochi, Properties of cured epoxide resins, The Adhesion Society of Japan 10, 161-168 (1974). (In Japanese)

2.2 M. Simbo, N. Nishitani, T. Takahama, Mechanical properties of acid-cured epoxide resins with different network structures, J. Appl. Polym. Sci. 29, 1709-1721 (1984).

2.3 J.D. Lemay, B.J. Swetlin, and F.N. Kelley, Structure and fracture of highly cross-linked networks, ACS Symp. Series 243, 165-183 (1984).

2.4 M. Ogata, T. Kawata, N. Kinjo, Relationship between crosslinking densities and physical properties of phenolic cured epoxides, Japanese J. Polym. Sci. Tech. 44, 193-199 (1987). (In Japanese)

2.5 M. Shimbo, Basic properties of cured material. In *Handbook of Epoxy Resins* (Ed. M. Shimbo), Nikkan Kogyo Shinbunsha, Tokyo, 299-325 (1987).

2.6 J.D. Lemay, B.J. Swetlin, and F.N. Kelley, Structure and fracture of highly cross-linked networks, ACS Symp. Series 243, 165-183 (1984).

2.7 R.A. Pearson, A.F. Yee, Toughening mechanisms in elastomer-modified epoxies, J. Mater. Sci. 24, 2571-2580 (1989).

2.8 V.T. Truong, Y.B. Truong, and B.C. Ennis, Mechanical properties, fracture toughness and microstructures of a crosslinked epoxy, Polym. Communications 32, 275-278 (1991).

2.9 G. Levita, S.D. Petris, A. Marchetti, and A. Lazzeri, Crosslink density and fracture toughness of epoxy resins, J. Mater. Sci. 26, 2348-2352 (1991).

2.10 B.G. Min, J.H. Hodgkin, and Z.H. Stachurski, The dependence of fracture properties on cure temperature in a DGEBA/DDS epoxy system, J. Appl. Poly, Sci. 48, 1303-1312 (1993).

2.11 A. Murakami, T. Ioku, D. Saunders, H. Aoki, T. Toshiki, S. Murakami, O.Watanabe, M. Saito, and H. Inoue, Fracture behaviour of epoxy resin containing thermoplastics and their composites, Proc. Benibana Int. Symp., 65-71 (1990).

2.12 E. Lawrence and L.E. Nielsen, Cross-linking – Effect on physical properties of polymers, J. Macromol. Sci. Revs. Macromol. Chem. C3, 69-103 (1969).

2.13 S. Lunak, J. Vladyka, and K. Dusek, Effect of diffusion control in the glass transition region on critical conversion at the gel point during curing of epoxy resins, Polym. 19, 931-933 (1978).

2.14 H.E. Adabbo and R.J.J. Williams, The evolution of thermosetting polymers in a conversion-temperature phase diagram, J. Appl. Polym. Sci., 27, 1327-1334 (1982).

2.15 J.B. Enns, and J.K. Gillham, Time-temperature-transformation (TTT) cure diagram: Modeling the cure behavior of thermosets, J. Appl. Polym. Sci., 28, 2567-2591 (1983).

2.16 I. Havlicek, K. Dusek, Kinetics of curing reaction of epoxy-amine systems in the glass transition region, a theoretical approach. In *Crosslinked Epoxies* (Eds.B. Sedlacek and J. Kahovec), Walter de Gruyter & Co., New York, 417-424 (1987).

2.17 M. Ochi, M. Morimura, and M. Shimbo, Curing mechanism of acid and acid-anhydride cured epoxy system, Proc. Thermosetting Plastics Symposium Japan, 129-132 (1987). (In Japanese)

2.18 S. Matsuoka, X. Quan, H.E. Bair, and D.J. Boyle, A model for the curing reaction of epoxy resins, Macromol. 22, 4093-4098 (1989).

2.19 J.P. Pascault and R.J.J. Williams, Glass transition temperature versus conversion relationships for thermosetting polymers, J. Polym. Sci. 28, 85-95 (1990).

2.20 S. Matsuoka, Related Topics. In Relaxation phenomena in polymers, Oxford university press, New York, 239-249 (1992).

2.21 X. Wang and J.K. Gillham, Analysis of crosslinking in amine-cured epoxy systems: The one-to-one relationship between Tg and conversion, J. Appl. Polym. Sci. 45 2127 (1992).

2.22 S.L. Simon and J.K. Gillham, Reaction kinetics and TTT cure diagrams for off-stoichiometric ratios of a high-Tg epoxy/amine system, J. Appl. Polym. Sci. 46, 1245 (1992).

2.23 J.H. Lee, J.W. Lee, Kinetic parameters estimation for cure reaction of epoxy based vinyl ester resin, Polym. Eng. Sci. 34, 9, 742-749 (1994).

2.24 F.Y.C. Boey, W. Qiang, Glass-transition temperature-conversion relationship for an epoxy –hexahydro-4-methylphthalic anhydride system, J. Appl. Polym. Sci. 78, 511-516 (2000).

2.25 C.A. Angell, Perspective on the glass transition, J. Phys. Chem. Solid 49, 863-871 (1988).

2.26 T. Kanaya, I. Tsukushi, and K. Kaji, Non-Gaussian parameter and heterogeneity of amorphous polymers, Prog. Theoretical Phys. Suppl. 126, 133-140 (1997).

2.27 T. Kanaya, T. Kawaguchi, and K. Kaji, Fast process of amorphous polystyrene below and above the glass transition temperature Tg as studied by quasielastic neutron scattering, J. Chem. Phys. 104, 3841-3850 (1996).

2.28 S. Matsuoka, X. Quan, H.E. Bair, and D.J. Boyle, A model for the curing reaction of epoxy resins, Macromol. 22 4093-4098 (1989).

2.29 C.M. Roland, Constraint on Local segmental motion in poly(vinylethylene) networks, Macromol. 27, 4242-4247 (1994).

2.30 D.M. Colucci, G.B. McKenna, Fragility of polymeric liquids: Correlations between thermodynamic and dynamic properties, Mat. Res. Soc. Symp. Proc. 455, 171-176 (1997).

2.31 B. Fitz, S. Andjelic, and J. Mijovic, Reorientational dynamics and intermolecular cooperativity of reactive polymers, 1, model epoxy-amine systems, Macromol. 30, 5227-5238 (1997).

2.32 S. Andjelic, B. Fitz, and J. Mijovic, Reorientational dynamics dynamics and intermolecular cooperativity of reactive polymers, 2, multifunctional epoxy-amine systems, Macromol. 30, 5239-5248 (1997).

2.33 J.L. Ricich, J.A. Koutsky, Nodular structure in epoxy resins, J. Appl. Polym. Sci. 20, 2111-2129 (1976).

2.34 S. Lunak, J. Vladyka, and K. Dusek, Effect of diffusion control in the glass transition region on critical conversion at the gel point during curing of epoxy resins, Polym. 19, 931-933 (1978).

2.35 K. Dusek, J. Plestil, F. Lednicky, and S. Lunak, Are cured epoxy resins inhomogeneous?, Polym. 19, 393-397 (1978).

2.36 D.R. Uhlmann, Electron microscopy and SAXS studies of amorphous polymers, Faraday Discussions of Chem. Soc. 68, 87-95 (1979).

2.37 G.C. Stevens , J.V. Champion, P. Liddell, Investigation of local order in unreacted DGEBA epoxy resin monomers by light scattering, J. Polym. Sci. Polym. Phys. Ed. 20, 327-344 (1982).

2.38 E.S-W. Kong, Physical aging in epoxy matrices and composites, Adv. Polym. Sci. 80, 125-171 (1986).

2.39 H. Leaderman, *Elastic and Creep Properties of Filamentous Materials and Other High Polymers*, Textile Foundation, Washington D.C., 175-182 (1943).

2.40 J.P. Benthem, W.T. Koiter, Asympototic approximations to crack problems. In *Mechanical Fracture Vol. 1. Methods of analysis and solutions of crack problems* (Ed. G.C. Sih), Noordhoff International Publishing, Leyden, 155-158 (1975).

2.41 R. Böhmer, K.L. Ngai, C.A. Angell, and D.J. Plazek, Nonexponential relaxations in strong and fragile glass formers, J. Chem. Phys. 99, 4201-4209 (1993).

2.42 D.J. Plazek, I.C. Choy, F.N. Kelley, E. Meerwall, and L.J. Suş, Viscoelasticity and Tearing Energy of Fluorinated Hydrocarbon Elastomers, Rubber Chem. Tech. 56, 866-882 (1982).

2.43 D.J. Plazek, I.C. Choy, The Physical Properties of Bisphenol-A-Based Epoxy Resins During and Afrer Curing. II., Creep Behavior Above and Below the Glass Transition Temperature, J. Polym. Sci. Pt. B 27, 307-324 (1989).

2.44 T. Adachi, T. Iketaki, M. Gamou, and A. Yamaji, Time-temperature dependence of fracture toughness of silica particulate-filled epoxy composite, Proc. Fourth Inter. Cong. on Thermal Stresses, 65-68 (2001).

2.45 F. Schwarzl, A.J. Staverman, Mechanical properties of polymers, J. Appl. Phys. 23, 838-843 (1952).

2.46 H. Hamaguchi, A. Hirakawa and Y. Ozaki, Appendix d. In *Raman spectroscopy* (Eds. H. Hamaguchi and A. Hirakawa), Center for academic Publications Japan, Tokyo, 189-249. (1988). (In Japanese)

2.47 T. Kitagawa and A.T. Tu, Molecular vibrations. *Introduction to Raman spectroscopy*, Kagaku-Dojin Publishing, Kyoto, 39-55 (1988). (In Japanese)

2.48 F.R. Dollish, W.G. Fateley, and F.F. Bentley, Heterocyclic compounds-Three and four membered rings. In *Characteristic Raman Frequencies of Organic Compounds*, Chapter 4, John Wiley & Sons, New York (1974).

2.49 M. Younes, S. Wartewig, D. Lellinger, B. Strehmel, and V. Strehmel, The curing of epoxy resins as studied by various methods, Polym. 35, 5269-5278 (1994).

2.50 R.E. Lyon, K.E. Chike, and S.M. Angel, in situ cure monitoring of epoxy resins using giber-optic Raman spectroscopy, J. Appl. Polym. Sci. 53, 1805-1812 (1994).

2.51 S.L. Kim, M.D. Skibo, J.A. Manson, R.W. Hertzberg, and J. Haniszewski, Tensile, impact and fatigue behavior of an amine-cured epoxy resin, Polym. Eng. Sci. 18, 1093-1100 (1978).

2.52 J. Mijovic, J.A. Koutsky, Correlation between nodular morphology and fracture properties of cured epoxy resins, Polym. 20, 1095-1107 (1979).

2.53 F.N. Kelley, D.R. Trainor, Model glassy inhomogeneous polymer networks, Polym. Bull. 7, 369-376 (1982).

Chapter 3

Time-temperature dependence of mode I fracture toughness

3.1 INTRODUCTION

Epoxy resins and their composites are used over a wide range of temperatures in various engineering fields, so estimating the temperature characteristics of mechanical properties, such as fracture toughness, is very important.

Epoxy resin is a thermo-viscoelastic material and its viscoelastic properties depend on the temperature, as shown in Chapter 2. Both dependences of time and temperature must be taken into account based on the time-temperature equivalence principle.[3.1] It is known that the strength, and the yield stress have the same equivalent factor, namely the shift factor, a_T, as the viscoelastic properties. Recent studies on the time-temperature dependence of fracture toughness have indicated that fracture toughness has also the same shift factor.[3.2-3.11]

In Chapter 2, I have showed that glass transition temperature, T_g, and Angell's fragility parameter, m, are very effective in estimating the mode I fracture toughness, K_{Ic}, of the epoxy resins and their composites at the room temperature. The temperature-time dependence of K_{Ic} might also be related to these two parameters.

The purpose of Chapter 3 is to clarify the time-temperature dependences of K_{Ic} for the bisphenol A-type epoxy resin and silica particulate-filled epoxy composite. In this chapter, as is done in Chapter 2, T_g and m are derived from the thermo-viscoelasticity measurement in

order to characterize the network morphology of epoxy resins and composites cured under various conditions. I first clearify the time-temperature dependences of fracture toughness of each material. Then, I discuss the relationship between T_g, m, and the time-temperature dependence of K_{Ic}.

3.2 EXPERIMENTAL PROCEDURE

3.2.1 Specimen

I prepared specimens composed of epoxy resin and composite. The materials used in this chapter were the same ones as used in Chapter 2. The blend was cast in a mold with 260 mm long, 10 mm thick, and 180 mm wide. The specimen was 5 mm thicker than that used in Chapter 2. Curing was done in two steps. First, all specimens were maintained at 353 K for 4 hours to gel the resin in pre-curing. Then, in post-curing, which greatly affects cross-linking reaction of the resin, the specimens were maintained under the conditions, shown in Table 1. Epoxies A and B were post-cured at 413 K for 10 hours and at 453 K for 6 hours with quenching, respectively, and Composite C, which had 26 % volume fraction of the silica particles, was post-cured at 433 K for 4 hours. The heating rate from pre-curing to post-curing was a constant 50 K/h for each process.

3.2.2 Thermo-viscoelasticity measurement

The thermo-viscoelastic properties of the cured epoxy resins and composites were examined with a dynamic viscoelastometer (Rheovibron DDV-III-EA, Orientec) as the same way as done in the previous chapter. After the measurement, the glass transition temperature, T_g, and the fragility parameter, m, were derived from the measurement results in order to characterize the specimen by the same procedure in Chapter 2. Also the master curve and the shift factor, a_T, were obtained according to the time-temperature equivalence principle.

3.2.3 Mode I fracture toughness test

I conducted a three-point bending test on a pre-cracked specimen to measure the mode I fracture toughness of each specimen, based on ASTM standards D5045-95. The specimen was 90 mm long, 20 mm wide, and 10 mm thick. The lengths of the pre-crack and the span were 10 and 80 mm. The tests were carried out under a constant displacement rate, from 1 to 300 μm/s at the loading point using a universal testing machine (8501, Instron), at different environmental temperatures ranged from 298 to 373 K in the thermostatic oven (3119-007, Instron). Either brittle or ductile fractures occurred depending on the combination of temperature and displacement rate. In brittle fractures, stress intensity factor, K_I, was used,

$$K_I = \frac{SP}{BW^{3/2}} \cdot f(\varsigma) \ , \qquad (3.1)$$

where

$$f(\varsigma)=\frac{3\varsigma^{1/2}\left\{\ 1.99-\varsigma(1-\varsigma)(2.15-3.93\varsigma+2.7\varsigma^2)\ \right\}}{2(1+2\varsigma)(1-\varsigma)^{3/2}}\ ,$$

$$\varsigma=\frac{a}{W}\ ,$$

and P is load. S, B, W, and a are the span length, thickness, width, and pre-crack length of the specimen. Substituting the maximum load P_c to P in Eq. (3.1), the mode I fracture toughness K_{Ic} was determined.

3.3 RESULTS AND DISCUSSION

3.3.1 Glass transition temperature and fragility

Figure 3.1 shows the Arrheniux plot for shift factor, a_T, of each specimen with the reciprocal of normalized T by T_g at standard temperature, $T_R = T_g$. The T_g and m are summarized in Table 3.1. Epoxies A and B have almost the same T_g, but different m. Composite C has a little higher T_g and lower m than them.

3.3.2 Time-temperature dependence of mode I fracture toughness

Figure 3.2 shows typical load-deflection curves for the specimens. The curve for Epoxy A at a rate of 60 μm/s at 373 K was linear until a brittle fracture occurred (Fig. 3.2(a)). When the displacement rate decreased, the maximum load increased and the curve exhibited a slightly non-linear relation. At much lower rates, ductile fractures occurred and the maximum load decreased. Then the fractures transferred from brittle to ductile. The transition was related to both temperature and rate. Composite C with a higher stiffness than Epoxy A had a similar curve to Epoxy A (Fig. 3.2(b)). The K_{Ic} in this chapter was evaluated from the load-deflection curve calculated from Eq. (3.1) for brittle fractures.

Figure 3.3 shows the temperature dependence of K_{Ic} under various displacement rates for Epoxy A and Composite C. Figure 3.4 shows the relationship between fracture toughnesses, K_{Ic}, and fracture initiation time, t_f, for Epoxy A and Composite C. The fracture initiation time, t_f, denotes the duration of loading until brittle fractures occurred. The value of K_{Ic} greatly varied with both temperature and t_f, although the correlation between temperature, t_f, and K_{Ic} is not clear in these figures.

3.3.3 Master curve of mode I fracture toughness

I plotted the master curves for K_{Ic} with a_T derived from the time-temperature dependence of dynamic storage modulus, E'. The t_f was used as a time parameter instead of displacement rate.[3.2,3.11,3.12] I examined the mode I fracture toughness characteristics of epoxy

resins and their composites using the master curves. Figure 3.5 has the master curve for K_{Ic} comparing E' and E'' in standard time 100 s. As shown in Fig. 3.5(a), E' of Epoxy A gradually decreased as the temperature was increased to 380 K, and then sharply decreased at around 390 K. The E'' was almost constant below 300 K, and then increased monotonously until about 390 K, where it peaked. Above 390 K, E'' decreased sharply. An α-relaxation phenomena can be seen near 390 K in both E' and E''. The K_{Ic} in Fig. 3.5(b) was approximately 1.3 $MPa \cdot m^{1/2}$ at around 300 K and decreased slightly from 310 to 350 K. At higher temperatures, K_{Ic} increased dramatically. At 370 K, brittle-ductile transition clearly occurred and K_{Ic} hit a maximum value of 2.5 $MPa \cdot m^{1/2}$. The K_{Ic} decreased above the brittle-ductile transition. The variations in K_{Ic} were mainly caused by the relaxation phenomena. The brittle-ductile temperature of K_{Ic} was about 20 K lower than the peak temperature of E''. The reason for this is that K_{Ic} was affected not only by the relaxation phenomena but also by the complicated crack tip configuration.

Table 3.1 Epoxy and composite specimens

	Post-curing temp, K	Post-curing time, h	Glass transition temperature, K	Fragility
Epoxy A	413	10	392	98
Epoxy B	453	6	388	85
Composite C	433	4	419	65

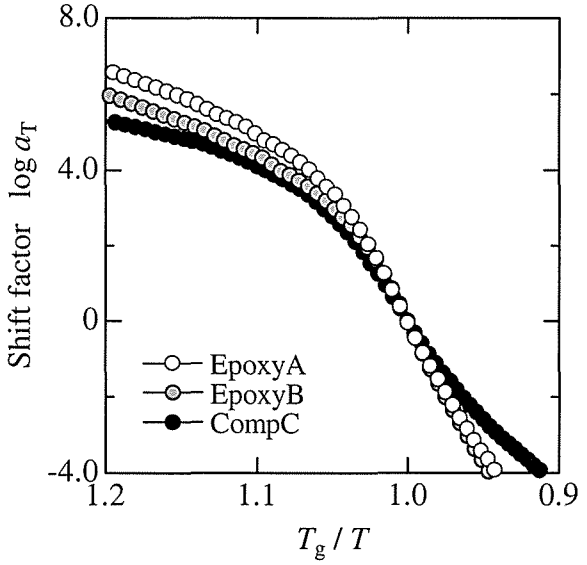

Figure 3.1 Shift factor
(Standard temperature is glass transition temperature.)

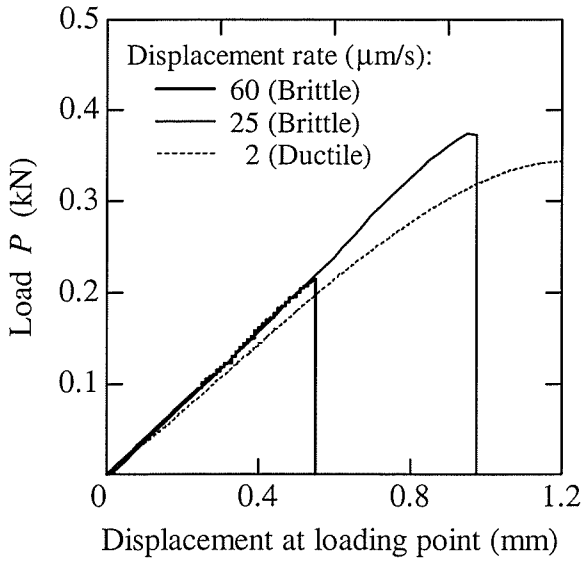

(a) Epoxy A

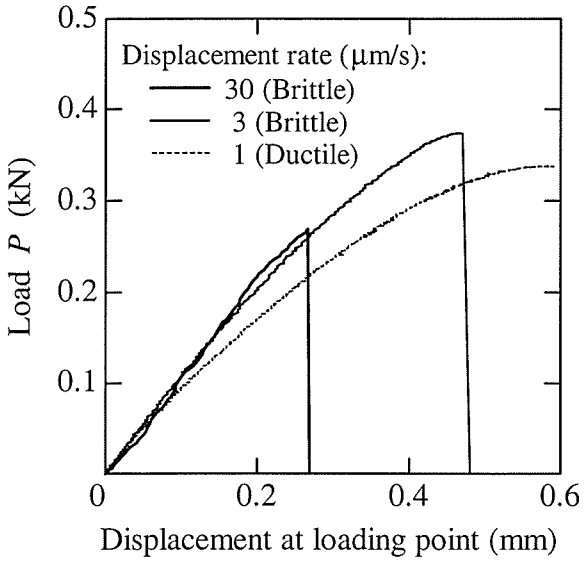

(b) Composite C

Figure 3.2 Load-displacement curve
(Test temperature is 373 K.)

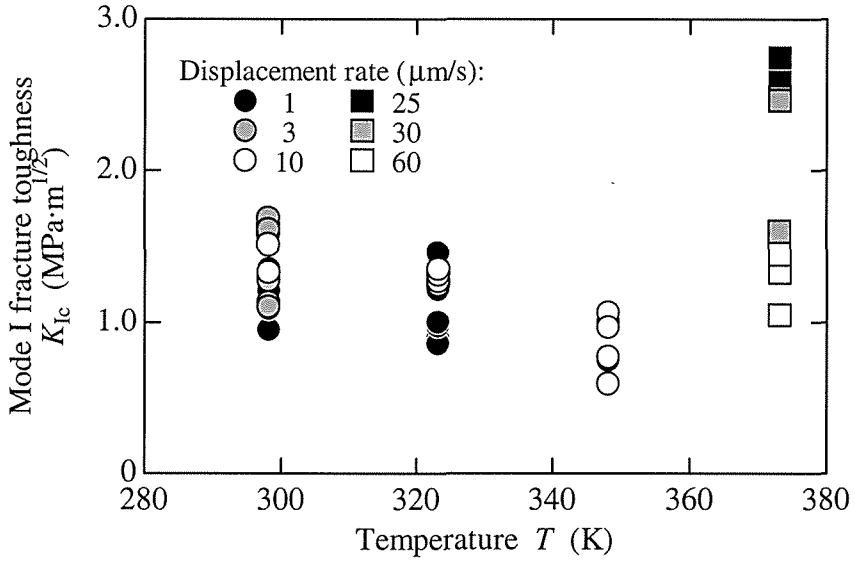

(a) Epoxy A

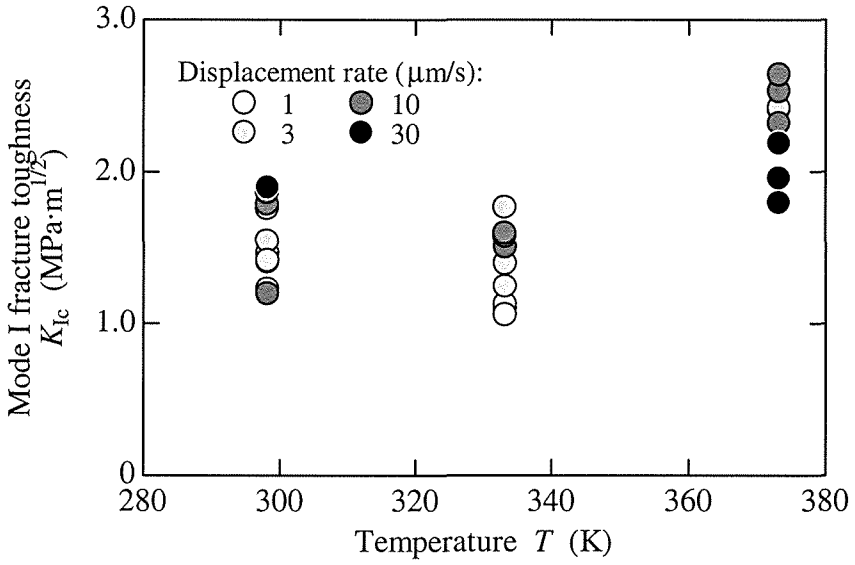

(b) Composite C

Figure 3.3 Temperature dependence of Mode I fracture toughness

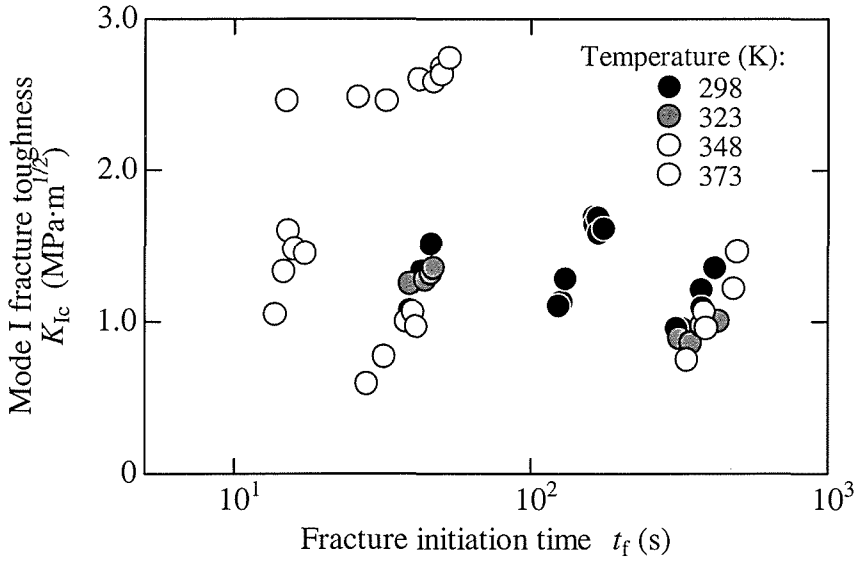

(a) Epoxy A

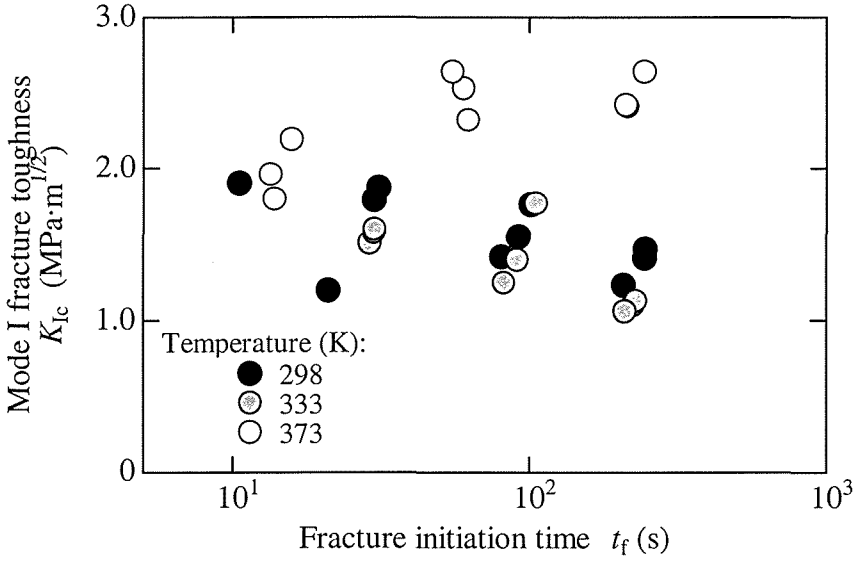

(b) Composite C

Figure 3.4 Time dependence of Mode I fracture toughness

3.3.4 Discussion

I considered the relationship between T_g, m, and the time-temperature dependence of K_{Ic} by comparing the master curves of K_{Ic} for the specimens. There was no clear m dependence for the values of K_{Ic} at around 300 K, as shown in Fig. 3.5. The K_{Ic} of Epoxy A with m = 98 increased rapidly at about 370 K, while that of Epoxy B with m = 85 increased gradually from 350 to 370 K. The K_{Ic} of Composite C with m = 65 increased more gradually. The brittle-ductile transition temperature of Epoxy A agreed with that of Epoxy B at approximately 370 K. The transition temperature of Composite C was about 400 K, because the brittle-ductile transition temperature depends on T_g.

3.4 CONCLUSION

In the present chapter, I discussed the relationships between the network morphology and the time-temperature dependence of mode I fracture toughness, K_{Ic}, for the bisphenol-A type epoxy resins and silica particulate-filled epoxy composites. First, the time-temperature dependence of K_{Ic} was investigated in the epoxy resins and the composites. The T_g and m were then used to characterize them.

It was found that K_{Ic} of the epoxy resin and composite depends on both temperature and time and that K_{Ic} follows the time-temperature equivalence principle. The time-temperature dependence behavior of K_{Ic} was affected by m: K_{Ic} of the epoxy resin with a smaller m increased from lower temperatures to the brittle-ductile transition temperature than that of resin with a larger m when their T_g saturated at approximately 400 K. The composite had smaller m than the epoxy resins so that K_{Ic} increased from a much lower temperature. In contrast, the brittle-ductile transition was governed by α-relaxation phenomena expressed by T_g, independent of m. I conclud that T_g and m are useful parameters not only for characterizing these epoxy materials but also for estimating the time-temperature dependence of mode I fracture toughness.

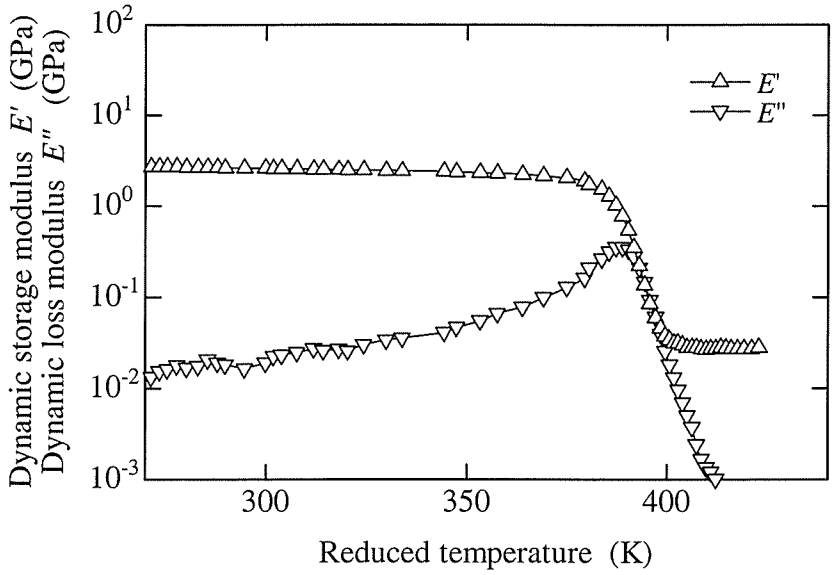

(a) Dynamic moduli of Epoxy A

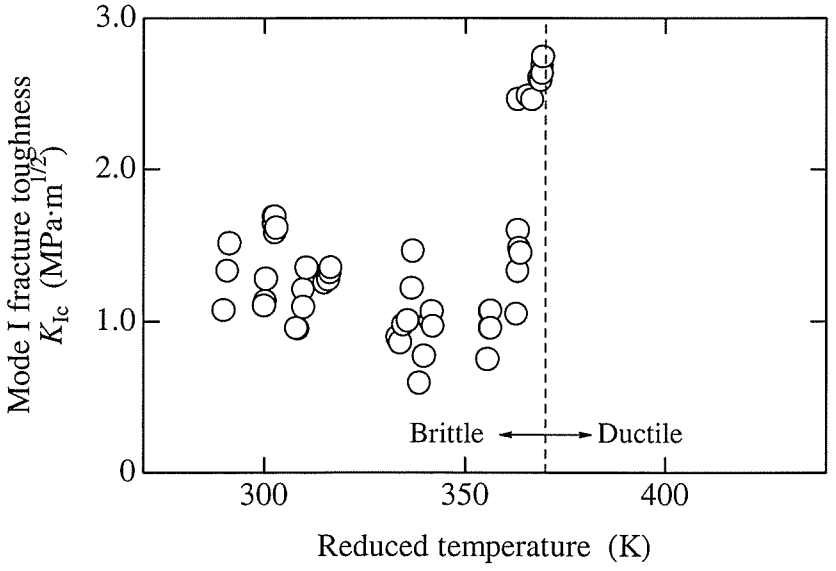

(b) Mode I fracture toughness of Epoxy A

Figure 3.5 Master curves of dynamic moduli and mode I fracture toughness (Standard time is 100 s.) (Continued)

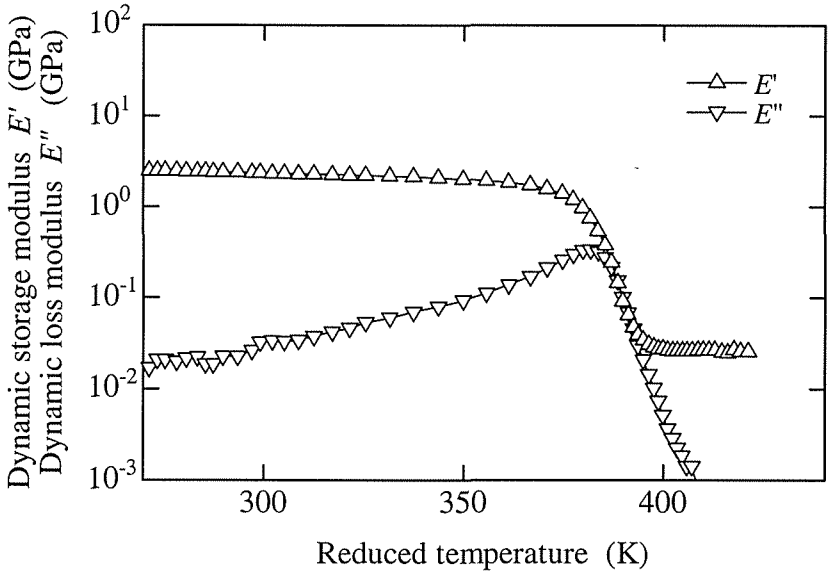

(c) Dynamic moduli of Epoxy B

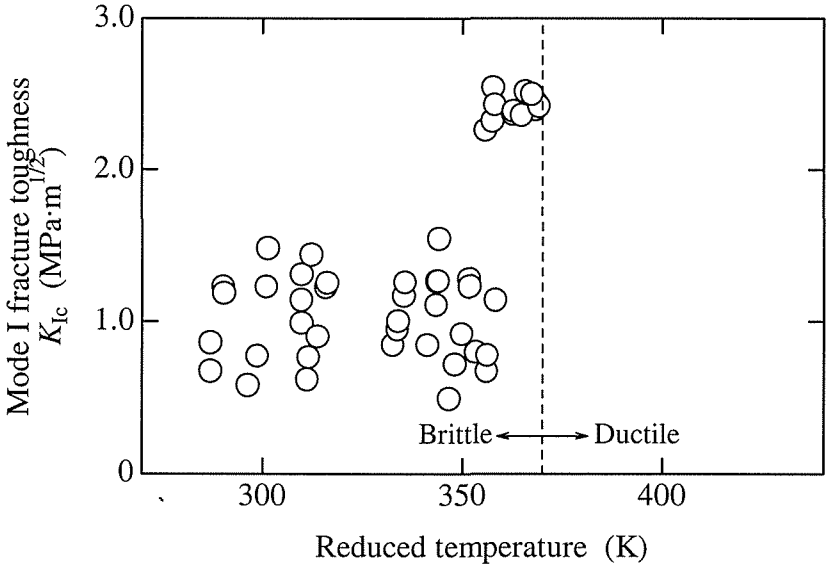

(d) Mode I fracture toughness of Epoxy B

Figure 3.5 Master curves of dynamic moduli and mode I fracture toughness (Standard time is 100 s.) (Continued)

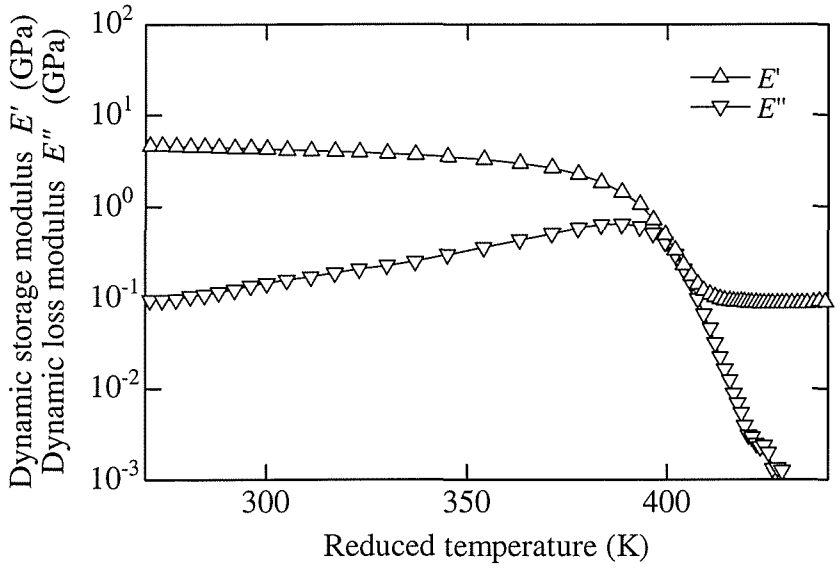

(e) Dynamic moduli of Composite C

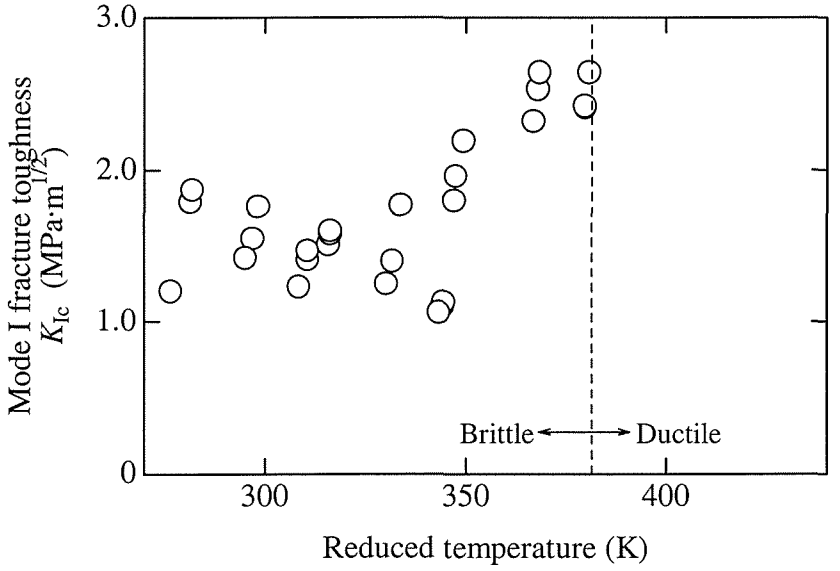

(f) Mode I fracture toughness of Composite C

Figure 3.5 Master curves of dynamic moduli and mode I fracture toughness (Standard time is 100 s.)

REFERENCES

3.1 H. Leaderman, *Elastic and Creep Properties of Filamentous Materials and Other High Polymers*, Textile Foundation, Washington D.C., 175-182 (1943).

3.2 S.F. Popelar, M.K. Chengalva, C.H. Popelar, and V.H. Kenner, Accelerated performance evaluation for polyimide films, Time-Dependent Failure of Polymers: Experimental Studies 155, 15-22 (1992).

3.3 Lim, W.W., Mizumachi, H. Fracture toughness of adhesive joints. II. temperature and rate dependencies of mode I fracture toughness and adhesive tensile strength, J. Appl. Polym. Sci. 57, 55-61, (1995).

3.4 Y. Han, Y. Yang, B. Li, X. Wang, and Z. Feng, Fracture toughness of phenolphthalein polyether ketone, J. Appl. Polym. Sci. 57, 655-661, (1995).

3.5 R. Frassine, A. Pavan, Viscoelastic effects on the interlaminar fracture behaviour of thermoplastic matrix composites: I. rate and temperature dependence in unidirectional PEI/carbon-fibre laminates, Comp. Sci. Tech. 54, 193-200 (1995).

3.6 L. Castellani, R. Frassine, A. Pavan, and M. Rink, Rate and temperature dependence of fracture toughness in ABS resins in relation to dispersed-phase structure, Polym. 37, 1329-1338 (1996).

3.7 R. Frassine, M. Rink, A. Pavan, Viscoelastic effects on the interlaminar fracture behaviour of thermoplastic matrix composites: II. rate and temperature dependence in unidirectional PEEK/carbon-fibre laminates, Comp. Sci. Tech. 56, 1253-1260 (1996).

3.8 F. Massa, R. Piques, and A. Laurent, Rapid crack propagation in polyethylene pipe: combined effect of strain rate and temperature on fracture toughness, J. Mater. Sci. 32, 6583-6587 (1997).

3.9 S. Yoneyama, K. Ogawa, A. Misawa, and M. Takashi, Evaluation of time-dependet fracture mechanics parameters of a moving crack in a viscoelastic strip, JSME Int. J. Series A 42, 624-630 (1999).

3.10 T. Adachi, T. Iketaki, M. Gamou, and A. Yamaji, Time-temperature dependence of fracture toughness of silica particulate-filled epoxy composite, Proc. the Fourth Int. Cong. on Thermal Stresses, 65-68 (2001).

3.11 R. Fracasso, M. Rink, A. Pavan, and R. Frassine, The effect of strain-rate and temperature on the interlaminar fracture toughness of interleaved PEEK/CF composites, Comp. Sci. Tech. 61, 57-63 (2001).

3.12 K. Ogawa, M Takashi, and A. Misawa, Crack growth mechanism below Tg in an epoxy strip. In *Experimental Mechanics* (Ed. I.M. Allison) Balkema, Rotterdam, 1141-1146 (1998).

Chapter 4

Time-temperature dependence of mode II fracture toughness

4.1 INTRODUCTION

In Chaps. 2 and 3, I discussed the relationship between the network morphology and mode I fracture toughness, allowing for the time and temperature dependences of the mode I fracture toughness. In the present chapter, I discuss the mode II fracture toughness for the epoxy resin.

Most of studies on mode II (in-plane shear) fracture toughness have dealt with composite laminates.[4.1-4.3] The mode II interlaminar fracture toughness of the laminates has been conventionally examined by end-notched flexible (ENF) or end-notched shearing (ELS) tests. Few studies of on the mode II fracture toughness of pure epoxy resin at room temperature have been reported;[4.4,4.5] what is more, the time-temperature dependence of the mode II fracture toughness of the epoxy resin has not as yet been clarified.

The purpose of the present chapter is to clarify the time-temperature dependence of mode II fracture toughness, K_{IIc}. First, an asymmetric four-point bending test at room temperature for the epoxy resins post-cured under various conditions are carried out to obtain K_{IIc}. I also measure the thermo-viscoelasticity and derived the glass transition temperature, T_g, and the fragility, m of each specimen from the measurement results in order to characterize the network morphology of epoxy resins. The relationship between T_g, m, and K_{IIc} are

discussed briefly. Then, I conduct the fracture test under various temperature and rate conditions and discuss the time-temperature dependence of K_{IIc}.

4.2 EXPERIMENTAL PROCEDURE

4.2.1 Specimen

I prepared specimens composed of the epoxy resin. The materials used in this chapter were the same ones as used in Chaps. 2 and 3. The blend was cast in a mold with 260 mm long, 5 mm thick, and 180 mm wide.

The specimens were made under fixed pre-curing conditions, at 353 K for 3 hours, and under various post-curing conditions, at 393 to 433 K for 3 to 30 hours, as summarized in Table 4.1. The heating rate from pre-curing to post-curing was a constant 72 K/h for each process.

4.2.2 Thermo-viscoelasticity measurement

The thermo-viscoelastic properties of the cured epoxy resins were examined with a dynamic viscoelastometer (Rheovibron DDV-III-EA, Orientec) as the same way as done in Chapters 2 and 3. Note, however, that the thickness of specimen was 2 mm. After the measurement, the glass transition temperature, T_g, and the fragility parameter, m, were derived from the measurement results in order to characterize the specimen in the same way as Chapter 2.

4.2.3 Mode II fracture toughness test

I conducted an asymmetric four-point bending test of a pre-cracked specimen to measure mode II fracture toughness, K_{IIc}.[4.6] The geometry and the size of the specimens are shown in Fig. 4.2 and Table 4.2, respectively. For the case of a/W $\approx$ 0.75 in this test, a stress field around a crack tip becomes pure in-plane shearing, and that induces mode II fracture behavior.

The tests were conducted with a universal material testing machine (8501, Instron) under various constant displacement rates from 1 to 30 μm/s at the loading point, at different temperatures from 123 K to 348 K in a thermostatic oven (3119-007, Instron). I performed the tests to investigate the temperature and time dependence of mode II fracture toughness. I measured the histories of the load and displacement at the loading point. The displacement was calibrated based on measured local deformations of the epoxy specimen at supporting and loading points, according to ASTM standards D5045-95. Deformation of the stainless steel jig could be neglected since the stiffness of the jig was sufficiently larger than that of the specimen.

If the load-displacement curve of each specimen is almost linear until breaking, the

stress field near the crack tip is regarded as small scale yielding. Therefore, linear elastic fracture mechanics can be applied to determine fracture toughness. The stress intensity factor for mode II, K_{II}, is given by

$$K_{II} = F_{II}(\varsigma)\sigma\sqrt{\pi a} \quad , \tag{4.1}$$

where

$$F_{II}(\varsigma) = -0.2915 + 6.3229\varsigma - 9.1199\varsigma^2 + 6.0570\varsigma^3,$$

$$\sigma = \frac{P_1 - P_2}{WB},$$

$$P_1 = \frac{S_1}{S}P, \quad P_2 = \frac{S_2}{S}P,$$

$$\varsigma = \frac{a}{W} \ .$$

Figure 4.1 defines S, S_1, S_2, W, B, and a. Substituting the maximum load at fracture P_c into P in Eq. (4.1) determines the fracture toughness, K_{IIc}.

After the fracture toughness test, I observed the fractured surfaces with an optical microscope (SZH-ILLD, Olympus Optical) and a scanning electron microscope (JSM-T200, JOEL) at an accelerating voltage of 5 kV.

4.3 RESULTS AND DISCSSION FOR ROOM TEMPERATURE TEST

The relationship between T_g, m, and the post-curing condition is shown in Fig. 4.2. The T_g was almost the same, approximately 400 K. According to the results in Chap. 2, it was probably that the cross-linking reaction of these specimens was almost saturated. Also m changed slightly around 80 and was independent of the post-curing conditions.

Then I conducted the asymmetric four-point test at the room temperature under the constant rate condition of 3 μm/s. Figure 4.3 shows the relationship between T_g, m and K_{IIc}. The values of K_{IIc} were drastically varied among 1.5 to 3.0 MPa·m$^{1/2}$ in spite of both T_g and m were almost constant. Moreover, unlike the case of the mode I fracture toughness, any clear relationships between T_g, m and K_{IIc} were not obtained.

Table 4.1 Epoxy specimens

Post-Curing		Glass Transition	Fragility
Temp, K	Time, h	Temp, K	
393	3	383	72
393	9	391	84
393	15	393	86
413	9	387	81
413	15	387	83
433	3	381	70
433	9	387	81
433	15	395	87
433	30	403	91

Table 4.2 Sizes for asymmetric four-point bending test (Unit: mm)

S	S_1	S_2	W	B	a	R_1	R_2
36	30	6	12	5	9	10	5

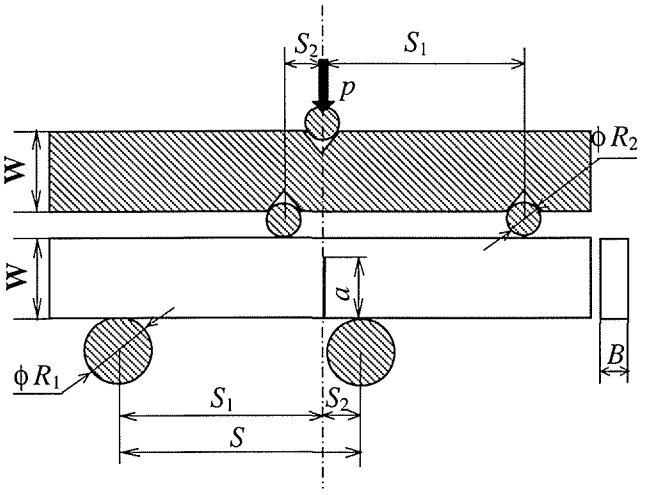

Figure 4.1 Asymmetric four-point bending test

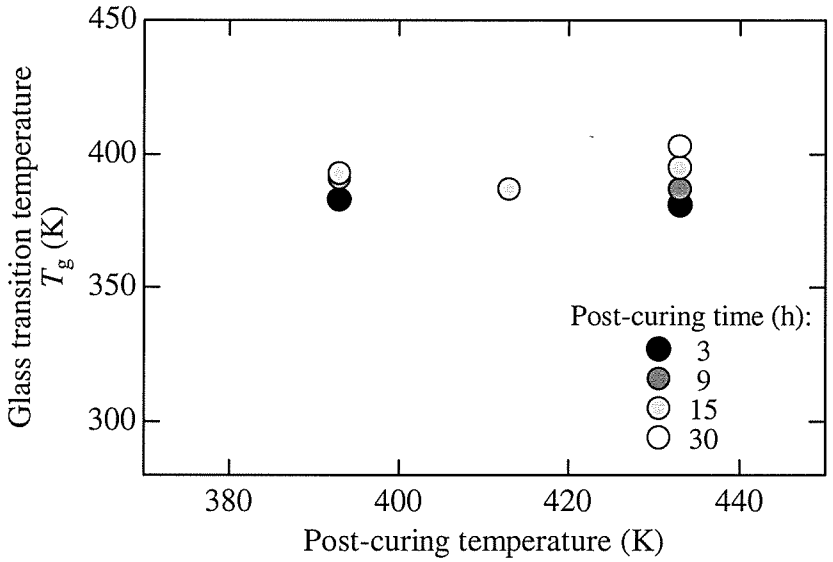

(a) Glass transition temperature

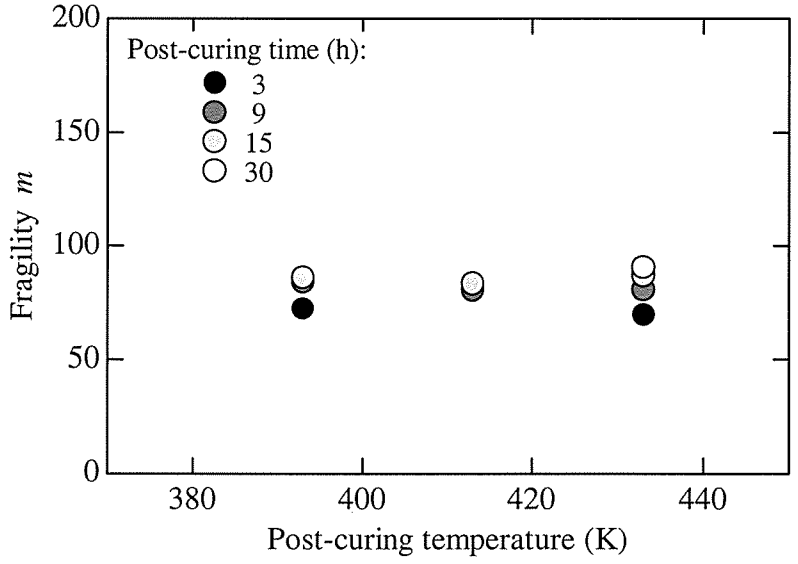

(b) Fragility

Figure 4.2 Parameters characterizing network morphology

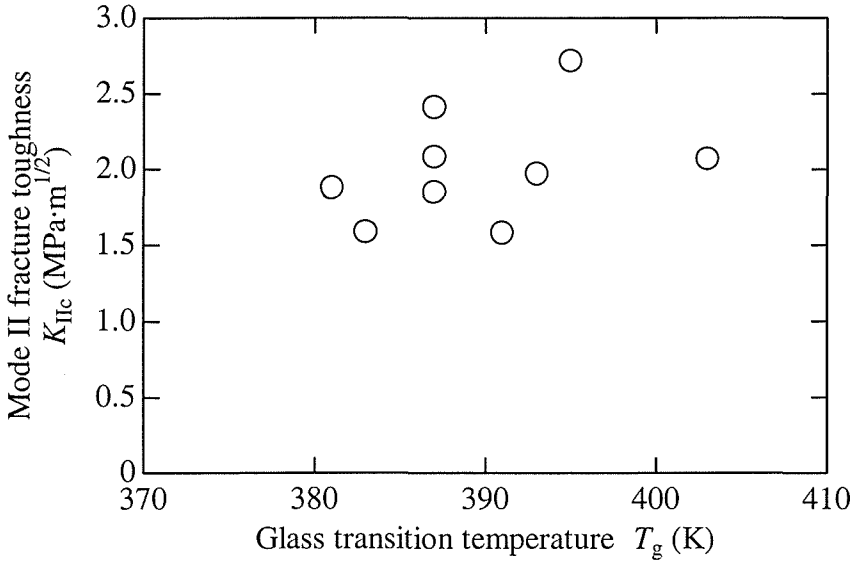

(a) Glass transition temperature

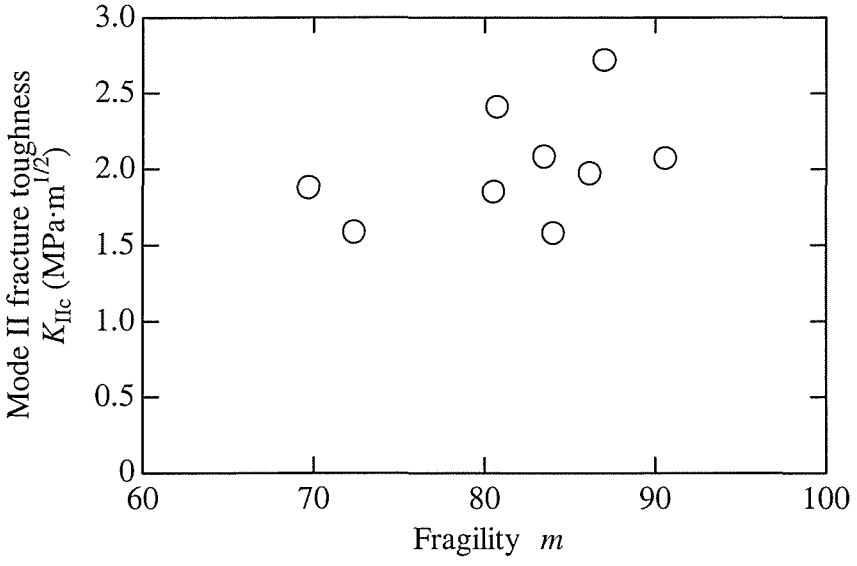

(b) Fragility

Figure 4.3 Mode II fracture toughness

4.4 RESULTS AND DISCUSSION FOR TIME-TEMPERATURE DEPENDENCE

4.4.1 Load-displacement curve

I selected the specimen post-cured at 433 K for 15 h and precisely investigated the time and temperature dependence of the mode II fracture toughness of the epoxy resin. Figures 4.4 shows typical load-displacement curves of the specimens for the rate of 1 μm/s under various temperature conditions. Whenever the temperature was less than 298 K, the load-displacement curves were linear until fracture. The slopes were almost the same, and the maximum load increased with the temperature. At 323 K, the maximum load became larger and the curve exhibited a slightly non-linear relation just before brittle fracture due to insufficient ductility. The curve for 348 K denoted a more non-linear relationship, and the maximum load was smaller than that for 323 K. Hereafter, I call such a brittle fracture accompanied with slightly non-linear stiffness, such as the cases of 323 K and 348 K "quasi-brittle" fractures.[4.7] Whenever temperature was more than 348 K, a ductile fracture occurred for any displacement rate within the present experimental conditions. In this study, the K_{IIc} values were evaluated from the maximum value of each load-displacement curve according to Eq. (4.1) for brittle and quasi-brittle fractures.

4.4.2 Fractography

The overall features of the fractured surface as observed with the optical microscope are shown in Fig. 4.5, where each specimen corresponds to that used to obtain the results shown in Fig. 4.4.

The typical features for brittle fracture[4.8,4.9] are shown in Fig. 4.5(a) and (b). They both show a smooth, mirror-like surface near the initial crack tip. As the crack propagated, pits began to appear on the surfaces and developed into parabolic patterns, so that the surfaces gradually became rough. As the crack propagated further, the parabolic patterns superimposed and the surface became rougher. The surface of the specimen tested at 298 K was rougher than that at 253 K, when the maximum load at 298 K was larger than that at 253 K, as shown in Fig. 4.4. The feature of fracture surfaces for mode II was similar to that for mode I which was obtained in Chapter 2.

Figure 4.5(c) and (d) show quasi-brittle fracture. Figure 4.6 presents the details of Fig. 4.6(d), as observed with the scanning electron microscope. The ductile crack propagation[4.10] appeared near the initial crack tip, prior to a mirror-like surface. (See Fig. 4.6(a)) After that, as is the case with the brittle fracture, the pits on the smooth surface developed into the parabolic patterns shown in Fig. 4.6(b). These parabolic patterns superposed, and then the surface became rough as is shown in Fig. 4.6(c). The region of the ductile crack propagation at 348 K was larger than that at 323 K, when the maximum load at 348 K was smaller than that at 323 K, as is shown in Fig. 4.4.

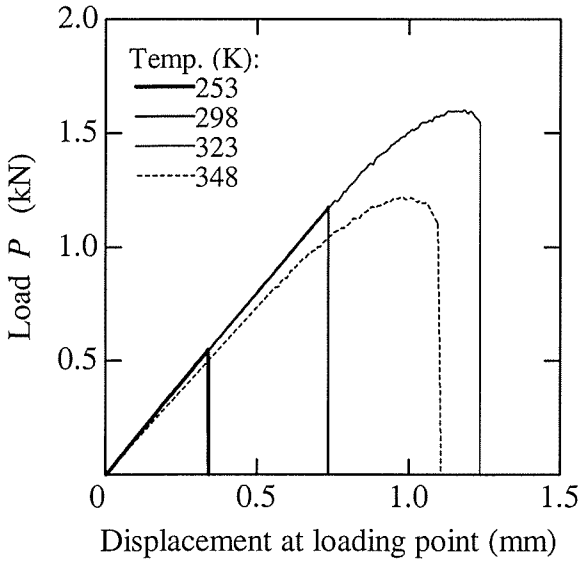

Figure 4.4 Load-displacement curve
(Displacement rate is 1 μm/s.)

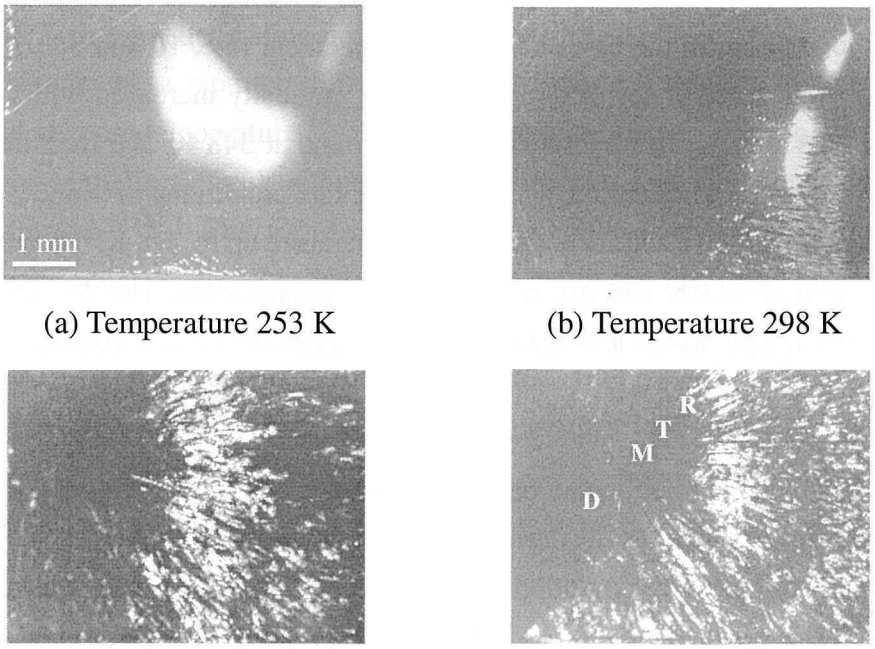

(a) Temperature 253 K (b) Temperature 298 K

(c) Temperature 323 K (d) Temperature 348 K

Figure 4.5 Fractured surface observed with optical microscope
(Initial crack exists at the far left and crack propagates from left to right in each picture. Displacement rate is 1mm/s. In Fig. 4.5(d), **D**: Ductile crack propagation, **M**: Mirror-like region, **T**: Transition region from mirror-like to rough surface, **R**: Rough region.)

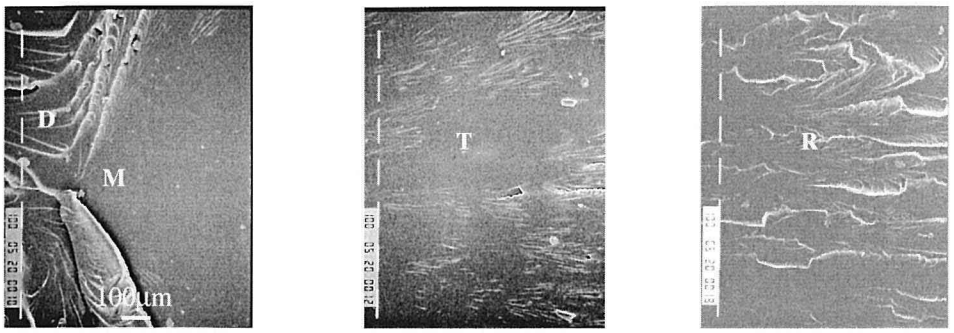

(a) **D** and **M** regions (b) **T** region (c) **R** region

Figure 4.6 Fractured surface observed with scanning electron microscope
(Initial crack exists at the far left of Fig. 4.6(a) and crack propagates from left to right. In each picture, **D**: Ductile crack propagation, **M**: Mirror-like region, **T**: Transition region from mirror-like to rough surface, **R**: Rough region.)

4.4.3 Time-temperature dependence of mode II fracture toughness

Figure 4.7 shows temperature dependence of mode II fracture toughness under various rate conditions. In the cases of a fast displacement rate, 10 and 30 μm/s, the fracture toughness K_{IIc} was small at lower temperature and gradually increased with the temperature up to 348 K. The quasi-brittle fracture appeared around at 348 K, and then the fracture form transferred from brittle to ductile. Under the slower rate conditions of 1 and 3 μm/s, K_{IIc} was small at lower temperature and increased with temperature up to 298 K. Then the quasi-brittle fracture appeared at 323 K and K_{IIc} decreased with temperature. The K_{IIc} was less than 2.0 MPa·m$^{1/2}$ at any temperatures less than 253 K regardless of the rate conditions, although the values at 298 K and 323 K were greatly scattered from 1.0 to 4.0 MPa·m$^{1/2}$. At 348 K, K_{IIc} was almost 3.0 MPa·m$^{1/2}$.

Figure 4.8 shows the relationship between the fracture toughness K_{IIc} and the fracture time, t_f. The fracture time, t_f, denotes the duration of loading until brittle fracture. The K_{IIc} increased with t_f under any temperature conditions except 348 K. For 348 K, when quasi-brittle fracture occurred in all the specimens, K_{IIc} slightly decreased with t_f. Thus, I found that the mode II fracture toughness K_{IIc} greatly depends on both temperature and time.

4.4.4 Master curve of mode II fracture toughness

To summarize the aforementioned dependences of K_{IIc}, I made the master curves of K_{IIc} data with the shift factor a_T derived from the time-temperature dependence of the dynamic storage modulus, E'. The t_f was used as a time parameter instead of the displacement rate, as is done in Chapter 3. The master curve of K_{IIc} compared with E' and E'' at standard temperature T_R= 298 K, is shown in Fig. 4.9. As shown in Fig. 4.9(a), E' decreased gradually as the reduced time increased to 10^5 s, and then sharply decreased. The E'' exhibited a small peak around 10^{-5} s and, after that, increased until about 10^5 s, where it peaked fully. After 10^5 s, E'' decreased sharply. An α-relaxation phenomena can be seen at 10^5 s in both E' and E''.

In Fig. 4.9(b), K_{IIc} was approximately 1.0 MPa·m$^{1/2}$ near 10^{-2} s. The K_{IIc} increased drastically for the time being, after that, a quasi-brittle fracture appeared and K_{IIc} hit a maximum value of about 3.5 MPa·m$^{1/2}$ at around 10^4 s, and then a ductile fracture appeared from 10^5 s. The variation of K_{IIc} was also caused by the relaxation phenomena. The increase in K_{IIc} seemed to be similar to that in E'' and the brittle-to-ductile fracture transition appeared near the peak of E'' (ξ= 10^5 s).

4.4.5 Discussion

It should be noted that, compared with K_{Ic} as shown in Chap. 3, the time of a brittle-ductile fracture transition in K_{IIc} is almost the same as the maximum time of E'', though K_{Ic} has its brittle-ductile transition when E'' has not peaked yet. Moreover, the behavior of K_{IIc}

is really variable even at the room temperature although K_{Ic} is almost constant under the same conditions. As is shown in Fig. 4.7, the values of K_{IIc} varied from 1.0 to 4.0 MPa·m$^{1/2}$ at room temperature 298 K strongly depending on the displacement rate.

Some studies have reported different values of mode II fracture toughness of epoxy resins measured at room temperature.[4.4,4.5] It was pointed out that evaluating mode II fracture toughness was essentially difficult although lots of methods and techniques for evaluation have been examined.[4.11,4.12] The significant time-temperature dependence of the mode II fracture toughness could make its value unstable and cause the difficulty in measuring it at room temperature.

Unobvious relationships between T_g, m, and K_{IIc} in Fig. 4.3 also should be attributed to this strong rate dependence of K_{IIc} at room temperature in Fig. 4.7, because K_{IIc} was measured under the constant rate condition of 3 μm/s at room temperature. The further experiments and discussion should be needed to clarify the relationships at room temperature.

4.5 CONCLUSION

In the present chapter, I discussed the mode II fracture toughness, K_{IIc}, of the bisphenol A-type of epoxy resin at room temperature and its time-temperature dependence. I performed an asymmetric four-point bending test under various conditions of temperature and displacement rate to investigate time-temperature dependence of K_{IIc}.

It was found, from the test results conducted at the room temperature under a constant displacement rate, that K_{IIc} strongly depended on the displacement rate and the temperature even at the room temperature due to the thermo-viscoelastic effect and also that there was no clear correlation between T_g, m, and K_{IIc}. The test results under various temperature and rate conditions showed that K_{IIc} followed the time-temperature equivalence principle in regard to the fracture time. The time-temperature dependence of K_{IIc} was similar to that of dynamic loss modulus, E'', and the transition from brittle to ductile fractures occurred nearly simultaneously when E'' peaked. I conclude that the time-temperature dependence of K_{IIc} must be considered in order to evaluate K_{IIc} and obtain the relationships between T_g, m, and K_{IIc} even at room temperature for the epoxy resins. I also suggested that a similar result could go for other thermo-viscoelastic materials.

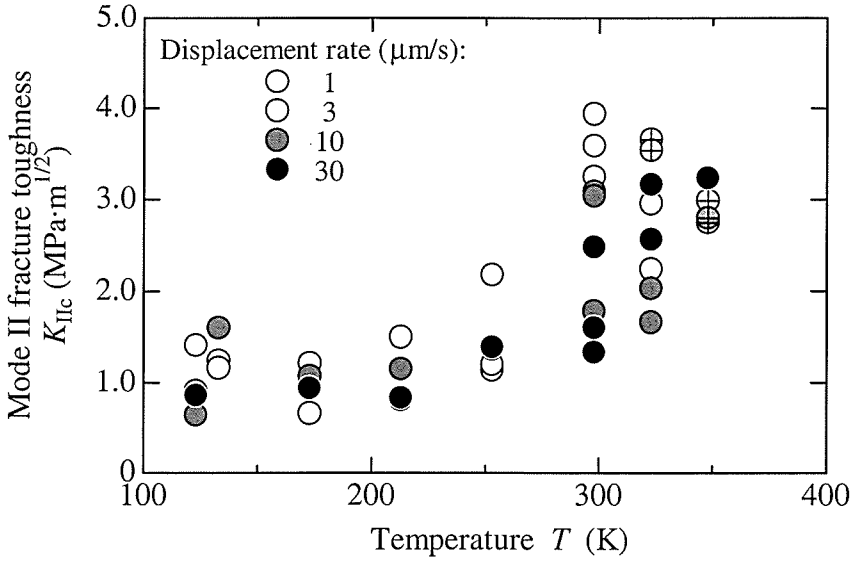

Figure 4.7 Temperature dependence of mode II fracture toughness

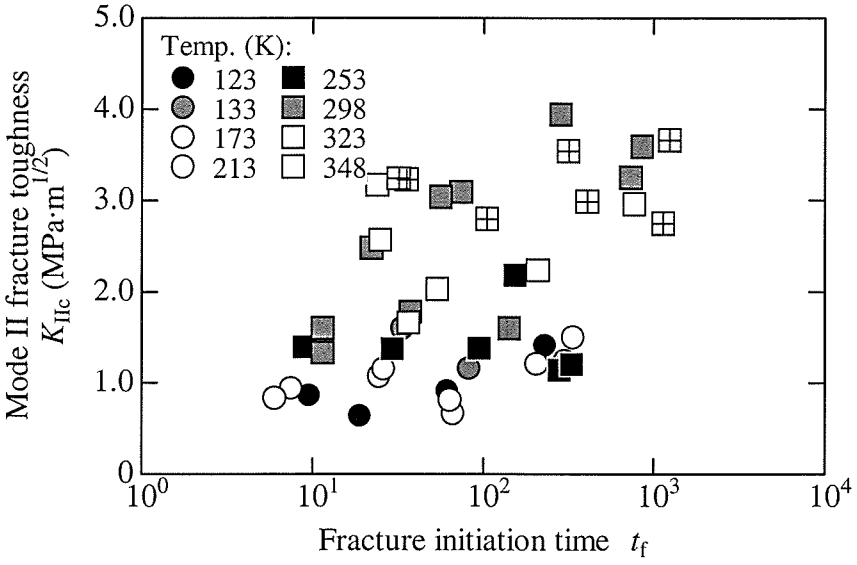

Figure 4.8 Time dependence of mode II fracture toughness
(+ with each legend represents quasi-brittle fracture.)

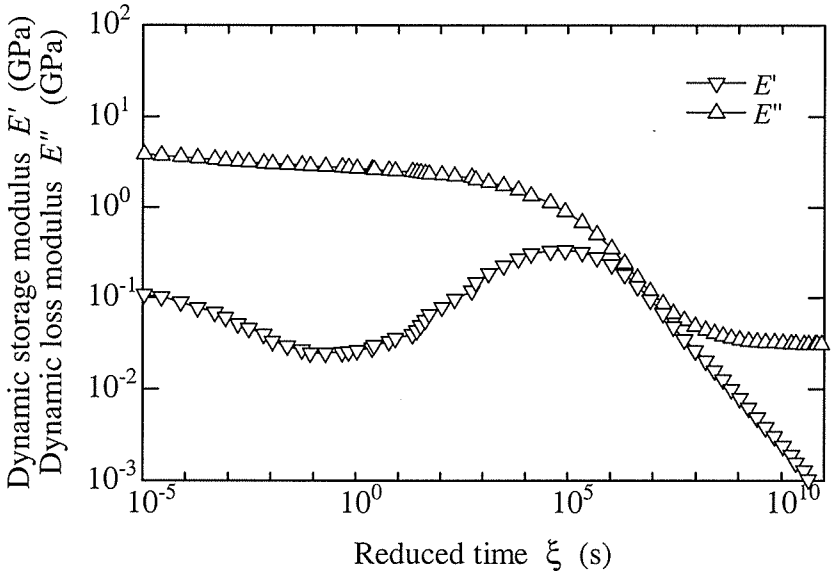

(a) Dynamic moduli

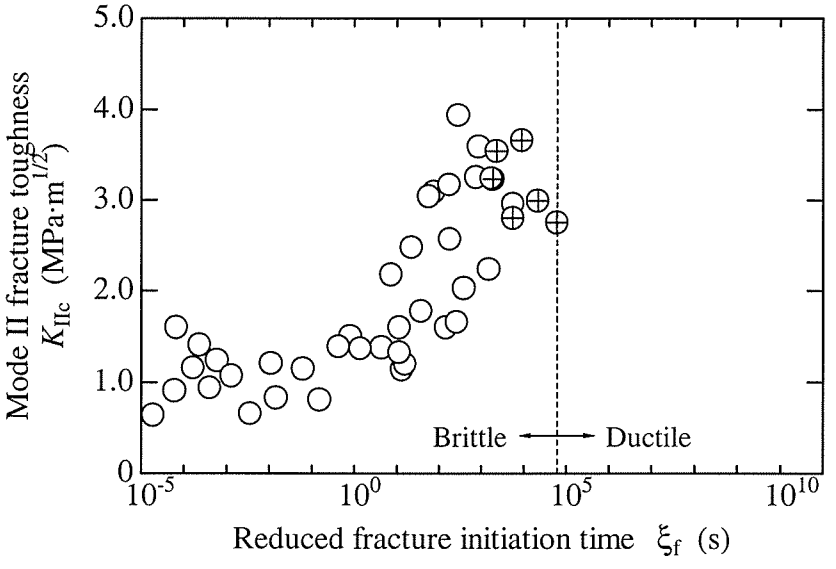

(b) Mode II fracture toughness

Figure 4.9 Master curves of dynamic moduli and mode II fracture toughness
(Standard temperature is 298 K. + with each legend represents quasi-brittle fracture.)

REFERENCES

4.1 S. Singh, I.K. Partridge, Mixed-mode fracture in an interleaved carbon-fibre/epoxy composite, Comp. Sci. Tech. 55, 319- 327 (1995).

4.2 B.R.K. Blackman, J.P. Dear, A.J. Kinloch, H. Macgillivray, Y. Wang, J.G. Williams, P. Yayla, The failure of fibre composites and adhesively bonded fibre composites under high rates of test. III. Mixed-mode I/II and mode II loadings, J. Mater. Sci. 31, 4467-4477 (1996).

4.3 W.X. Wang, Y. Takao, T. Matsubara, and H.S. Kim, Improvement of the interlaminar fracture toughness of composite laminates by whisker reinforced interlamination, Comp. Sci. Tech. 62, 767-774 (2002).

4.4 H.S. Kim, P. Ma, Mode II fracture mechanisms of PBT-modified brittle epoxies, J. Appl. Polym. Sci. 69, 405-415 (1998).

4.5 C. Liu, Y. Huang, and M.G. Stout, Enhanced mode-II fracture toughness of an epoxy resin due to shear banding, Acta Mater. 46, 5647-5641 (1998).

4.6 *Stress Intensity Factors Handbook* (Ed. Y. Murakami), Pargamon, Oxford, 941 (1987).

4.7 T. Adachi, M. Osaki, A. Yamaji, and M. Gamou, Time-temperature dependence of the fracture toughness of a poly(phenylene sulphide) polymer, Proc. Instn. Mech. Eng. Pt. L: J Mater.: Design and Appl. 217, 29-34 (2003)

4.8 L. Plangsangmas, J.J. Mecholsky Jr., and A.B. Brenman, Determination of fracture toughness of epoxy using fractography, J. Appl. Polym. Sci. 72, 257-268 (1999).

4.9 J.R.M. d'Almeida, G.W. Menezes, and S.N. Monteiro, Ageing of the DGEBA/TETA epoxy system with off-stoichiometric compositions, Mater. Res. 6, 415-420 (2003).

4.10 R.J. Gaymans, M.J.J. Hamberg, and J.P.F. Inberg, The brittle-ductile transition temperature of polycarbonate as a function of test speed, Polym. Eng. Sci. 40, 256-262 (2000).

4.11 D.K. Shetty, A.R. Rosenfield, and W.H. Duckworth, Mixed-mode fracture in biaxial stress state: application of the diametral-compression (Brazilian disk) test, Eng. Frac. Mech. 26, 825-840 (1987).

4.12 S.Suresh, C.F. Shih, A. Morrone, and N.P.O'Dowd, Mixed-mode fracture toughness of ceramic materials, J. Am. Ceram. Soc. 73, 1257-1267 (1990).

Chapter 5

Mixed mode I/II fracture toughness at room temperature

5.1 INTRODUCTION

It is widely recognized that fractures generally initiate at preexisting flaws oriented at arbitrary angles to the farfield loading direction, so that the flaws in material of practical structures are seldom subjected to pure mode I or II loading. Clarifying fracture criteria under multiaxial loading condition are a very important issue. Many different theoretical criteria have been suggested for mixed-mode fractures to determine fracture onset and the direction of crack initiation.[5.1-5.7] The validity of the criteria has been discussed for various materials.[5.8-5.11] Most criteria predict that a crack will propagate in the direction along which stress[5.1,5.2], strain[5.3], energy[5.4,5.5], and so on, have (or will have) a maximum value, when the parameter attains its inherent critical value, which are independent of mode mixity.

Some researchers, however, pointed out that these critical values depend on the mode mixity[5.12-5.16] and that phenomenon of mode II fracture is essentially independent of that of mode I fracture.[5.12,5.14,5.15] Liu et al.[5.13] experimentally showed that mode II fracture toughness of epoxy composites strongly depended on a loading rate while the mode I fracture toughness is hardly sensitive to it. They also reported in another paper[5.14] the difference of fracture mechanism between mode I and mode II fracture for epoxy resins. Awaji and Kato[5.15] suggested a extended fracture criterion for mixed mode I/II fracture by postulating that the

fracture energy depends on the area of a frontal process zone at a crack tip, which varies with mode mixity, based on Griffith[5.17] energy criterion. Almost all research of fracture criteria is done on elastic and plastic materials.

In Chapter 2 to 4, I discussed the pure mode I and II fracture toughnesses. The purpose of the present chapter is to clear a fracture criterion of the epoxy resin for the mixed mode I/II at the room temperature. In particular, the epoxy resins with different glass transition temperatures are used in order to investigate the effect of the glass transition temperature, T_g, on the mixed mode fracture toughness. Also I examine common four fracture criteria such as maximum hoop stress criterion[5.1], minimum strain energy density criterion[5.6], maximum stress release rate criterion[5.4], and Richard's empirical criterion[5.18], to compare with the experimental results. Based on the results, I discuss the onset of fracture and the direction of crack initiation of the epoxy resin with different T_g.

5.2 EXPERIMENTAL PROCEDURE

5.2.1 Specimen

I prepared specimens of epoxy resin. The materials used in this chapter were the same ones as used in Chapter 2. The blend was cast in a mold with 260 mm long, 5 mm thick, and 180 mm wide, which was the same size as that used in Chapter 2.

First, for pre-curing, the material was kept at 353 K for 3 hours to gel the matrix resin. Then, for post-curing, which affects the cross-linking reaction of the resin, the specimen was kept at 433 K for 3 or 15 hours. The material post-cured for 3 h and 15 h were hereafter called Epoxy A and Epoxy B, respectively. Specimens were made from cured plates of Epoxy A or B by a diamond-cutter.

Then, I measured the glass transition temperatures T_g of the obtained materials with a dynamic viscoelastometer (Orientec, Rheovibron DDV-III-EA) by means of the same way in Chapter 2. The T_gs of Epoxy A and B were 385 and 399 K, respectively, which were almost sufficiently cross-linked as shown in Chapter 2.

5.2.2 Fracture toughness test

I conducted a three-point bending test (3PBT) of an asymmetric pre-cracked specimen to measure mixed mode I/II fracture toughness at room temperature (298K).[5.8,5.10,5.19-5.21] The geometry and the size of the specimen are shown in Fig. 5.1 and Table 5.1, respectively. The stress field around the crack tip can be changed by the distance from the center to the crack, d, as shown in Table 5.1. In the case of a symmetric pre-crack, namely $d = 0$, the crack is subject to pure tension (mode I).[5.22]

I also conducted an asymmetric four-point bending test (4PBT) of a pre-cracked specimen.[5.21-5.23] The geometry and the size are shown in Fig. 5.2 and Table 5.1, respectively.

The stress field near the crack tip can be changed by the pre-crack length, a. In the case of a/W ≈ 0.75, a pre-crack is subject to pure shearing (mode II).[5.23]

Each fracture test was conducted using a universal material testing machine (8501, Instron) at room temperature under a constant displacement rate of 3 μm/s at the loading point. The histories of the load and displacement at the loading point were measured. The displacement was calibrated based on measured local deformations of the epoxy specimen at supporting and loading points. Deformation of the stainless steel jig could be neglected since the stiffness of the jig was sufficiently larger than that of the specimen.

If the load-displacement curve of the specimen is almost linear until breaking, stress field near the crack tip is small scale yielding. Therefore, linear elastic fracture mechanics can be applicable in order to determine the mixed mode I/II fracture toughness. The stress intensity factors for each mode, K_I and K_{II}, are given by: [5.20-5.22]

$$K_I = \sigma_0 F_I \sqrt{\pi a}\,, \tag{5.1}$$

$$K_{II} = \sigma_0 F_{II} \sqrt{\pi a}\,, \tag{5.2}$$

and F_I, F_{II} for 3PBT are different from ones for 4PBT. For 3PBT,

$$\sigma_0 = \frac{3PL}{W^2 B},$$

$$F_I = F_{I3} \cdot \left(1 - \frac{a}{W}\right)^{-3/2},$$

$$F_{II} = F_{II3} \cdot \left(1 - \frac{a}{W}\right)^{-1/2},$$

for 4PBT,

$$\sigma_0 = \frac{P}{BW},$$

$$F_I = F_{I4} \cdot \left(1 - \frac{d}{L}\right),$$

$$F_{II} = F_{II4} \cdot \left(1 - \frac{d}{L}\right),$$

$$P = \frac{d}{L+d} p\,.$$

Here, F_{I3}, F_{II3}, F_{I4}, and F_{II4} are geometric functions given in references.[5.20,5.22] Substituting the maximum load at fracture P_c into P in Eqs. (5.1) and (5.2), I can determine mode I and II components of fracture toughness under the mixed mode loading, $(K_I)_c$ and $(K_{II})_c$.

In this above fracture tests, the pre-crack is subject to mixed mode loading. Therefore, the following parameter for load mixity at the vicinity of crack-tip is introduced:[5.10]

$$\phi = \frac{2}{\pi}\tan^{-1}\left\{\frac{K_{II}}{K_I}\right\}. \tag{5.3}$$

The mode mixity parameter ϕ varies from 0 (for pure mode I) to 1.0 (for pure mode II). In this chapter, ϕ was varied from 0 to 0.55 according to the crack location d for 3PBT, and ϕ was done from 0.65 to 1.0 according to the crack length a for 4PBT as shown in Fig. 5.3. After the tests, I observed the crack path with an optical microscope (SZH-ILLD, Olympus Optical) and measured the angle of the crack initiation to the plane of the pre-crack.

Table 5.1 Sizes for 3PBT and 4PBT (Unit: mm).

	L	W	**B**	**d**	a	R_1	R_2
3PBT	25	12	5	**0 ~ 22.5**	6	10	5
4PBT	30	12	5	6	**2 ~ 8**	10	5

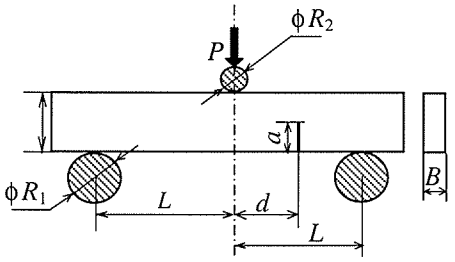

Figure 5.1 Three-point bending test (3PBT) of asymmetric pre-cracked specimen (Shaded area represents stainless steel. White area represents epoxy specimen.)

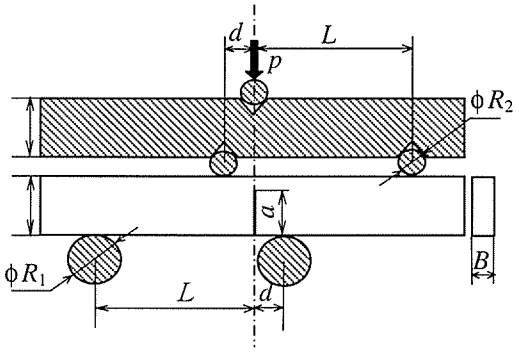

Figure 5.2 Asymmetric four-point bending test (4PBT) (Shaded area represents stainless steel. White area represents epoxy specimen.)

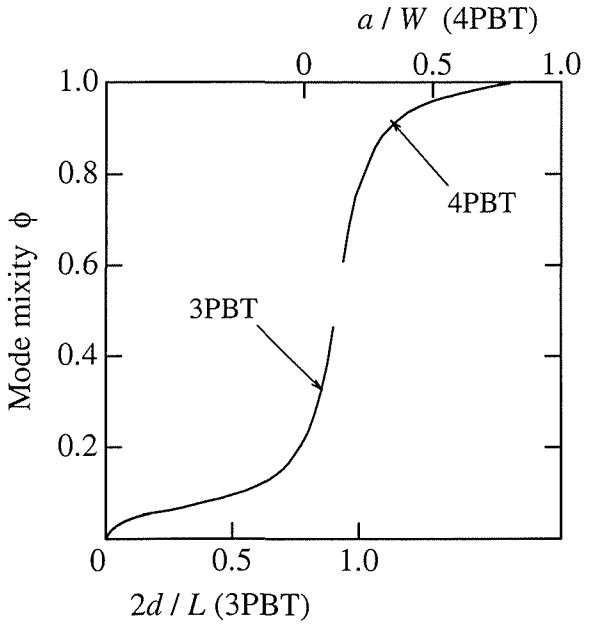

Figure 5.3 Mode Mixity

5.3 FRACTURE CRITERION FOR MIXED MODE

Over the years, several fracture criteria under the mixed mode loading condition have been suggested to predict the angle of crack initiation to the plane of the pre-crack θ_c and fracture onset. In this chapter, four typical fracture criteria for the mixed mode were examined and compared with the experimentally obtained crack initiation angle, θ_c, and the fracture locus, $(K_I)_c/K_{Ic} - (K_{II})_c/K_{Ic}$, where K_{Ic} is pure mode I fracture toughness.

5.3.1 Maximum hoop stress criterion (MHSC)

The hoop stress $\sigma_{\theta\theta}$ under mixed mode loading in plane problems is generally expressed as follows:

$$\sigma_{\theta\theta} = \frac{1}{\sqrt{2\pi r}}\left\{K_I\left(\frac{3}{4}\cos\frac{\theta}{2}+\frac{1}{4}\cos\frac{3\theta}{2}\right)-K_{II}\left(\frac{3}{4}\sin\frac{\theta}{2}+\frac{3}{4}\sin\frac{3\theta}{2}\right)\right\}, \tag{5.4}$$

where r and θ denote polar coordinates, where the origin of the coordinate is placed at the crack tip.

The MHSC[5.1] predicts that the crack will advance in the direction θ_c perpendicular to the maximum hoop stress (or principal stress) when the maximum hoop attains the critical value, $\sigma_{\theta\theta c}$, which can usually be determined from pure mode I fracture toughness, K_{Ic} $(=\sqrt{2\pi r}\sigma_{\theta\theta c})$ under the condition of $\theta_c = 0$.

5.3.2 Minimum strain energy density criterion (MEDC)

The strain energy density factor S under mixed mode loading is generally given by

$$\begin{aligned} S = {} & \frac{1}{16\pi\mu}(\kappa-\cos\theta)(1+\cos\theta)K_I^2+\frac{1}{8\pi\mu}\sin\theta\{2\cos\theta-(\kappa-1)\}K_IK_{II} \\ & +\frac{1}{16\pi\mu}\{(\kappa+1)(1-\cos\theta)+(1+\cos\theta)(3\cos\theta-1)\}K_{II}^2 \end{aligned}, \tag{5.5}$$

where

$$\kappa = \begin{cases} 3-4\nu & \text{(plane strain)} \\ (3-\nu)/(1+\nu) & \text{(plane stress)} \end{cases},$$

and μ and ν are the shear modulus and Poisson's ratio.

The MEDC[5.6] predicts that fracture will occur in the direction θ_c of minimum strain energy density when the interior minimum of the strain energy density factor reaches the critical value, S_c, which can be also determined from K_{Ic}.

5.3.3 Maximum energy release rate criterion (MERC)

The energy release rate G under mixed mode loading is generally given by

$$G=\frac{\kappa+1}{2\mu}\left(\frac{1}{3+\cos^2\theta}\right)^2\left(\frac{\pi-\theta}{\pi+\theta}\right)^{\theta/\pi}\left\{\left(1+3\cos^2\theta\right)K_I^2+8\sin\theta\cos\theta K_I K_{II}+\left(9-5\cos^2\theta\right)K_{II}^2\right\}. \quad (5.6)$$

The MERC[5.4] states that the crack will grow in the crack initiation angle θ_c along which the strain energy release rate will be a maximum, when the energy release rate reaches a critical value, G_c. The fracture locus based on MERC can be adequately approximated by the following empirical equation:[5.24]

$$\frac{K_I}{K_{Ic}}+\frac{3}{2}\left(\frac{K_{II}}{K_{Ic}}\right)^2=1. \quad (5.7)$$

5.3.4 Empirical criterion (EMPC)

Richard[5.18] proposed the following EMPC for the mixed mode;

$$\frac{K_I}{K_{IC}}+\left(\frac{K_{II}}{CK_{IC}}\right)^2=1. \quad (5.8)$$

Here, C is an empirical constant,

$$C=\frac{K_{IIc}}{K_{Ic}}.$$

K_{IIc} is the fracture toughness in pure mode II loading. Many researchers have proved that Eq. (5.8) provides good fits to experimental data.

5.4 RESULTS AND DISCUSSION

5.4.1 Crack initiation angle

Figure 5.4 shows typical fractured specimens after the test (Epoxy B). Figure 5.4(a) shows the fractured specimens for 3PBT. Every crack initiated at an angle $-\theta_c$ less than 45 degrees. In the case of 4PBT, every crack initiated at an angle $-\theta_c$ more than 45 degrees as shown in Fig. 5.4(b). In both fracture tests, the cracks finally propagated toward the nearest loading point.

Figure 5.5 shows the relationship between the mode mixity, ϕ, and the crack initiation angle $-\theta_c$ obtained in the 3PBT and 4PBT. In both specimens, $-\theta_c$ increased continuously up to 45 degree with increasing ϕ from 0 to 0.2, and then it stayed almost constant at 50 degrees between 0.2 and 0.8. For $\phi>0.8$, $-\theta_c$ increased again and reached 70 degrees at $\phi=1.0$.

From the results for Epoxy A and B, it is clear that they had almost the same initiation angle over the whole ϕ regardless of the glass transition temperature, T_g.

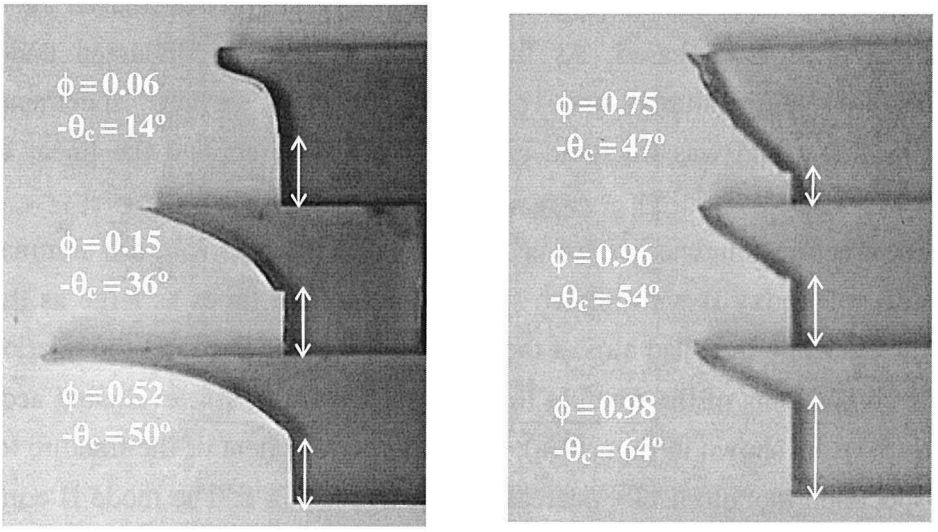

(a) 3PBT (b) 4PBT

Figure 5.4 Fractured specimen after test (Epoxy B)
(Arrow represents pre-crack.)

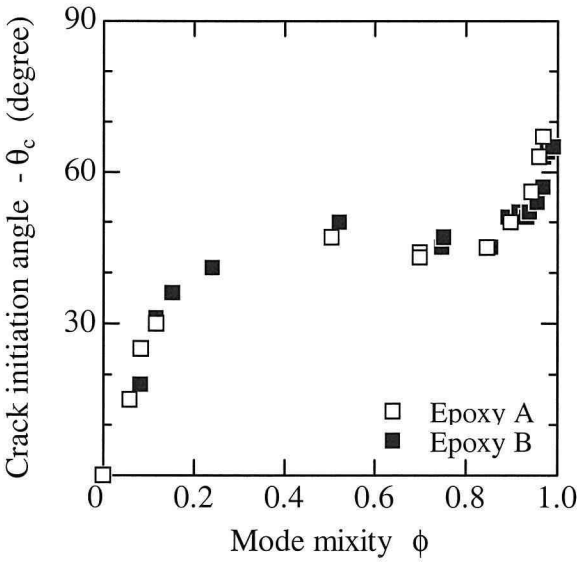

Figure 5.5 Crack initiation angle

5.4.2 Fracture toughness for mixed mode

Figures 5.6 show typical load-displacement curves (Epoxy B), which are ones shown in Fig. 5.4. In the 3PBT [Fig. 5.6(a)], the maximum load and the slope of the curve increased when ϕ increased. In the 4PBT [Fig. 5.6(b)], the slope slightly decreased and the maximum load decreased as ϕ increased. As far as both tests were conducted under the present conditions of temperatures and displacement rates, every specimen had linear load-displacement and was fractured brittlely. I therefore applied the linear elastic fracture mechanics.

The fracture toughnesses for each pure mode, K_{Ic} and K_{IIc}, are summarized in Table 5.2. The K_{IIc} of Epoxy B with higher T_g was roughly two times as large as that of Epoxy A with lower T_g, while they had almost the same K_{Ic}. Figure 5.7 shows the relationship between ϕ and the components of the fracture toughness, $(K_I)_c$ and $(K_{II})_c$, evaluated according to Eqs. (5.1) and (5.2). As shown in Fig. 5.7(a), the mode I component of the fracture toughness, $(K_I)_c$, of each specimen monotonically decreased with increasing ϕ. The mode II component, $(K_{II})_c$, in Fig. 5.7(b) gradually became larger until ϕ = 0.7, and after that, the value increased suddenly and unstably at the vicinity of $\phi = 1.0$. For Epoxy A and B, the variation of $(K_I)_c$ with ϕ was similar to each other over the whole ϕ regardless of T_g. The $(K_{II})_c$ of Epoxy B was much larger than that of Epoxy A for the case of $\phi > 0.5$, although $(K_{II})_c$ was approximately the same for $\phi < 0.5$. Figure 5.8 shows the relationship between $(K_I)_c$ and $(K_{II})_c$. It is seen that the locus of Epoxy B became larger than that of Epoxy A as the loading mode approached mode II.

Table 5.2 Glass transition temperature and fracture toughness for pure modes

	Post-cure	T_g (K)	K_{Ic} (MPa·m$^{1/2}$)	K_{IIc}(MPa·m$^{1/2}$)	K_{IIc} / K_{Ic}
Epoxy A	433 K, 3 h	385	1.94	1.52*1	0.78
Epoxy B	433 K, 15 h	399	1.99	2.77*2	1.40

(*1. $\phi = 0.97$, *2. $\phi = 0.99$)

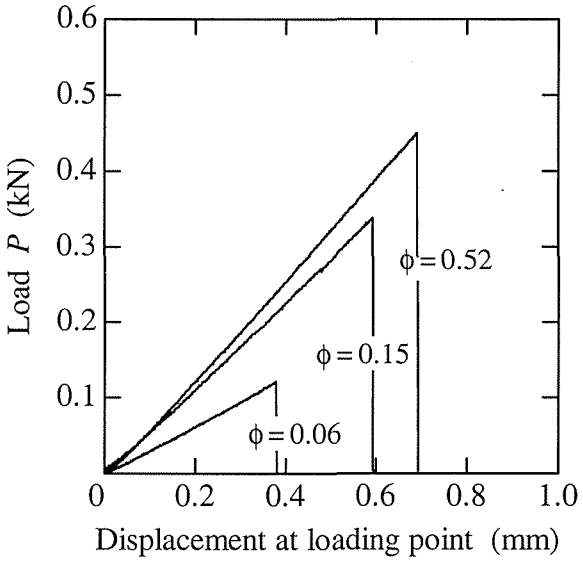

(a) 3PBT

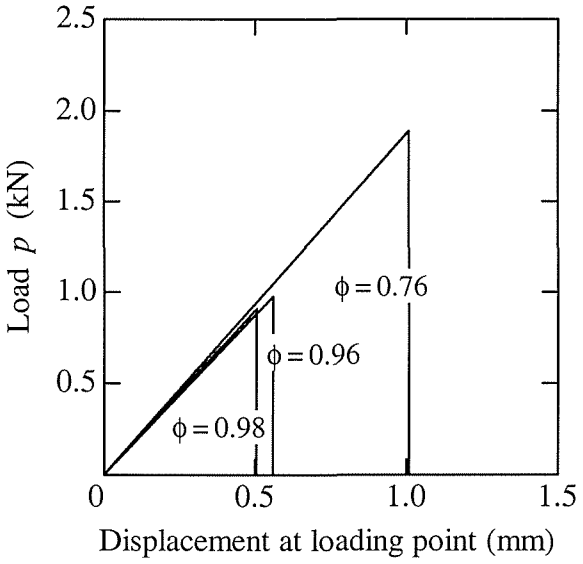

(b) 4PBT

Figure 5.6 Load-displacement curve at loading point (Epoxy B)

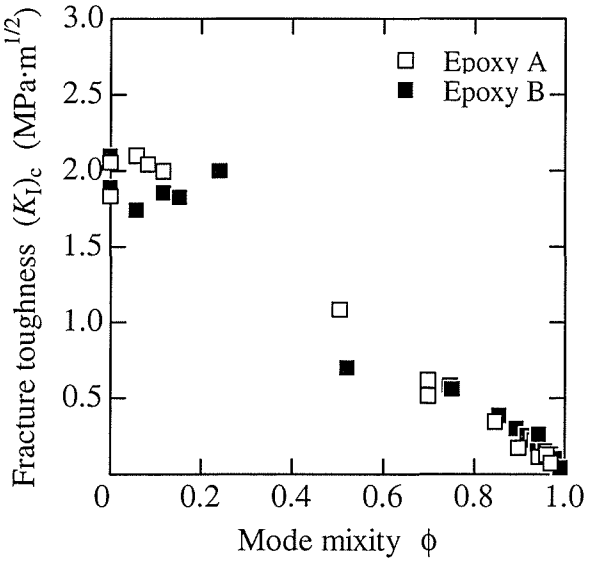

(a) Mode I component

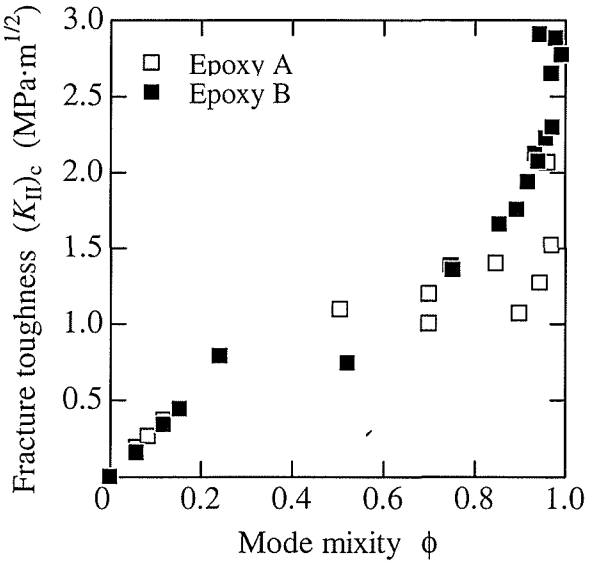

(b) Mode II component

Figure 5.7 Variation of fracture toughness with mode mixity

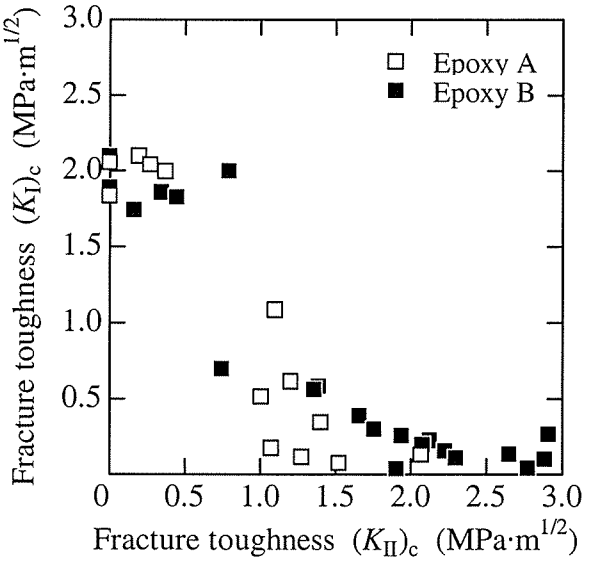

Figure 5.8 Relationship between mode I and mode II fracture toughness

5.4.3 Fracture criteria for mixed mode

The directions of crack initiation predicted by the aforementioned criteria are shown along with the present experimental results in Fig. 5.9(a). Poisson's ratio, ν, was assumed to be 0.40 for MEDC. The angle $-\theta_c$ predicted from every criterion monotonically increased with ϕ. The experimental result roughly accorded with each criterion below $\phi = 0.5$. When ϕ increased from 0.5 to 0.8, the measured $-\theta_c$ was almost constant while the one predicted by the criteria monotonically increased with ϕ. In the vicinity of $\phi = 1.0$, the criterion based on MHSC and the experimental result reached to about 70 degrees correspondently.

Figure 5.9(b) shows the fracture loci for mixed mode, $(K_I)_c/K_{Ic} - (K_{II})_c/K_{Ic}$, predicted by common criteria and obtained from the experimental results. The pure mode toughnesses K_{Ic} and K_{IIc} of Epoxy A and B shown in Table 5.1 were used to obtain the loci of EMPC and the loci of the experiments. The locus of Epoxy C was relatively in agreement with MERC just except around of $\phi = 1$. In the vicinity of $\phi = 1.0$, it was unstable because of a drastic increase in $(K_{II})_c$. For Epoxy B, the experimental result just near $\phi = 0$ was naturally agreed with every criterion since every locus was deduced base on K_{Ic}. However, as ϕ became larger, the experimental result was deviated from the predicted loci. The K_{IIc}/K_{Ic} of Epoxy B at $\phi = 1$ was approximately 1.4, while that of MHSC, MEDC, and MERC was less than 1.0. Moreover, the experimental locus of Epoxy B was not obviously an elliptical form, so that it disagreed with any criterion, even EMPC.

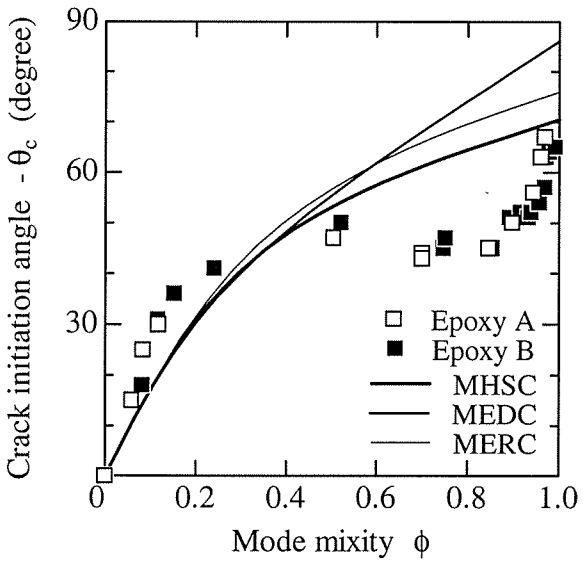

(a) Crack initiation angle

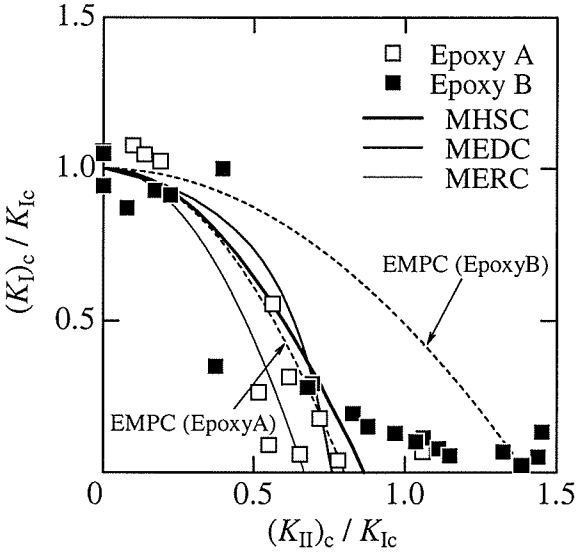

(b) Fracture locus

Figure 5.9 Criterion for mixed mode I/II fracture

5.4.4 Discussion

Though most theoretical criteria predict K_{IIc}/K_{Ic} of less than 1.0 and that the fracture locus for mixed mode, $(K_I)_c/K_{Ic} - (K_{II})_c/K_{Ic}$, has an elliptical form, the present experimental results do not follow those predictions as shown in Fig. 5.9(b). The criteria predict generally that the crack propagates when parameters such as $\sigma_{\theta\theta}$ and G attain their inherent critical values.

Some researchers, however, pointed out that these critical values depend on the mode mixity[5.12-5.16] and that a mode II fracture is essentially independent of a mode I fracture.[5.12,5.14,5.15] As is shown in the previous Chapter 4, for a brittle fracture of the epoxy resin, the pure mode II fracture toughness is quite sensitive to the thermo-viscoelastic relaxation phenomenon even at room temperature, while the relaxation had little effect on the pure mode I fracture. This means that the common criteria based on any inherent critical value are applicable not to epoxy resin, because the relaxation effect on the fracture toughness depends on mode mixity. This also could be the reason for the drastic increase in $(K_{II})_c/K_{Ic}$ near $\phi = 1$ for and the non-elliptic locus. In addition, the relaxation phenomenon is attributable to the cross-linked network represented by T_g, so that $(K_{II})_c/K_{Ic}$ depends on T_g even when $(K_I)_c/K_{Ic}$ is almost the same with regard of T_g.

As for the angle of the crack initiation, ã certain relationship between the mode mixity and the crack initiation angle was obtained without regard to T_g and also $(K_{II})_c/K_{Ic}$, although it did not wholly follow the angle predicted by the criteria as shown in Fig. 5.9(a). Several studies of ceramics and polymer materials have shown similar results,[5.25,5.26] therefore, one factor determining the crack initiation angle could be a component of mode I fracture toughness $(K_I)_c/K_{Ic}$.

5.5 CONCLUSION

I investigated the fracture locus and the direction of the crack initiation under the mixed mode I/II for epoxy resin at room temperature. In order to obtain these fracture properties under the mixed mode loading over a whole mode mixity ϕ, I conducted asymmetric bending tests. I examined four common fracture criteria – maximum hoop stress criterion, minimum strain energy density criterion, maximum energy release rate criterion, and Richard's empirical criterion – to compare with the experimental results.

The angle of crack initiation became larger with increasing ϕ. The angle was in a relatively good agreement with every criterion at lower ϕ, namely near pure mode I. In the vicinity of $\phi = 1$, namely, pure mode II, the experimentally obtained angle corresponded to that predicted by the maximum hoop stress criterion.

The fracture toughness $(K_I)_c$ under mixed mode loading monotonically decreased with ϕ. $(K_{II})_c$ increased drastically at the vicinity of $\phi = 1$ due to the thermo-viscoelastic relaxation

effect. Though most of all existing criteria, except an empirical one, predict that K_{IIc}/K_{Ic} is less than 1.0 regardless of K_{IIc} and the fracture locus, $(K_I)_c/K_{Ic} - (K_{II})_c/K_{Ic}$, is an elliptical form, the present experimental results did not follow those criteria.

K_{Ic} was almost the same and K_{IIc} was different in the specimens with different glass transition temperatures, T_g, and thus, their fracture loci were different. However, the angles well accorded with each other independent of T_g. It is concluded that, therefore, the relaxation effect on fracture toughness varies with the mode mixity, so the common fracture criteria for mixed mode could not be applied to the epoxy resin. In contrast, the crack initiation angle can be possibly determined independently of the relaxation effect.

REFERENCES

5.1 F. Erdgan, G.C. Sih, On the crack extension in plates under plane loading and transverse shear, J. Basic Eng. 85, 519-527 (1963).

5.2 Y.J. Chao, S.Liu, On the failure of cracks under mixed-mode loads, Int. J. Frac. 87, 201-223 (1997).

5.3 M.R. Ayatollahi, H. Abbasi, Crack growth prediction based on the maximum hoop strain criterion-plate strain, Build. Res. J. 49, 167-168 (2001).

5.4 M.A. Hussain, S.L. Pu, J. Underwood, Strain energy release rate for a crack under combined mode I and mode II, ASTM STP 560, 2-28 (1974).

5.5 M.Y. He, J.W. Hutchinson, Kinking of a crack out of an interface, Trans. ASME J. Appl. Mech. 56, 270-278 (1989).

5.6 G.C. Sih, Strain-energy-density factor applied to mixed mode crack problems, Int. J. Frac. 10, 305-321 (1974).

5.7 S.M.A. Khan, M.K. Khraisheh, A new criterion for mixed mode fracture initiation based on te crack rip plastic core region, Strength of Mater. 20, 55-84 (2004).

5.8 G. Hua, M.W. Brown, and K.J. Miller, Mixed-mode fatigue thresholds, Fatigue Eng. Mater. Structures 5, 1-17 (1982)..

5.9 T.M. Maccagno, J.F. Knott, The fracture behaviour of PMMA in mixed modes I and II, Eng. Frac. Mech. 34, 65-86 (1989).

5.10 S. Suresh, C.F. Shih, A. Morrone, and N.P. O'Dowd, Mixed-mode fracture toughness of ceramic materials, J. Am. Ceram. Soc. 73, 1257-1267 (1990).

5.11 J.P. Campbell, R.O.Ritchie, Mixed-mode, high-cycle fatigue-crack growth thresholds in Ti-6Al-4V, I. A comparison of large- and short-crack behavior, Eng. Frac. Mech. 67, 209-227 (2000).

5.12 M.Y. He, H.C. Cao, and A.G. Evans, Mixed-mode fracture: the four-point shear specimen, Acta Metal. Mater. 38, 839-846 (1990).

5.13 C. Liu, Y. Huang, M.L. Lovato, and M.G. Stout, Measurement of the fracture toughness of a fiber-reinforced composite using the Brazilian disk geometry, Int. J. Frac. 87, 241-263 (1997).

5.14 C. Liu, Y. Huang, M.L., and M.G. Stout, Enhanced mode-II fracture toughness of an epoxy resin due to shear banding, Acta Mater. 46, 2647-5661 (1998).

5.15 Awaji H, Kato T. Mode I-II combined mode fracture criterion for brittle materials, J. Japan Inst. metals 62, 735-741 (1998). (In Japanese)

5.16 Y.A. Roy, R. Narasimhan, and P.R. Arora, An experimental investigation of constraint effects on mixed mode fracture initiation in a ductile aluminium alloy, Acta Mater. 47, 1587-1596 (1999).

5.17 A.A. Griffith, The phenomena of ruture and flow in solids, Phil. Trans. Roy. Soc. Lon.

A221, 163–197 (1920).

5.18 H.A. Richard, Fracture predictions for cracks exposed to superimposed normal and shear stresses, Forschungsh 631, 1-60 (1985).

5.19 J.P. Benthem, W.T. Koiter, Asymptotic approximations to crack problems. In *Methods of Analysis and Solutions of Crack Problems* (Ed. G.C. Sih) 1, Noordhoff International Publishing, Leyden, 131-178 (1973)

5.20 T. Fett, Mixed-mode stress intensity factors for three-point bending bars, Int. J. Frac. 48, R67-R74 (1991).

5.21 T. Fett, G. Gerteisen, S. Hahnenberger, G. Martin, and D. Munz, J, Europ. Ceram. Soc. 15, 307-312 (1995).

5.22 T. Fett, Stress intensity factors for edge crack subjected to mixed mode four-point bending, Theoretical and Appl. Frac. Mech. 15, 99-104 (1991).

5.23 Mixed mode and Mode III cracks. In: Y. Murakami, editors. Stress intensity factors handbook, vol. 2. Pargamon (Oxford), Soc Mater Sci, Japan: 1987. 941.

5.24 K. Palaniswamy, W.G. Knauss, On the problem of crack extension in brittle solids under general loading. In:Nemat-Nasser, editor. Mechanics today, vol. 4. Pargamon(Oxford), Am. Aca. Mech. 1978. p. 87.

5.25 Li M, Sakai M, Mixed-mode fracture of ceramics in asymmetric four-point bending: Effect of crack-face grain interlocking/bridging, J. Am. Ceram. Soc. 79, 2718-2726 (1996).

5.26 K. Kishimoto, M. Notomi, S. Kadota, T. Shibuya, N. Kawamura, and T. Kawakami, Mixed-mode fracture behavior of silica particulate filled epoxide resin. In: Miller KJ, McDowell DL, editors. Mixed-mode crack behavior, ASTM STP 1359. West (1999).

Chapter 6

Prediction of fracture initiation in thermo-viscoelastic media

6.1 INTRODUCTION

The use of thermo-viscoelastic materials such as polymers and their composites under various time and temperature environments have been on the increases in recent years. To predict thermo-mechanical and fracture behaviors with time and temperature dependence of material properties in any environment have become important recently.

Many papers have treated thermal stress problems for viscoelastic materials.[6.1,6.2] Fundamental studies on thermo-viscoelastic behavior were carried out in the 1960s. Morland and Lee[6.3] proposed a constitutive law for thermo-rheologically simple media. Muki[6.4] and Sternberg[6.5] analyzed the transient temperature and stress fields of such simple geometries as a plate and polar symmetry. The transient thermal stress problems in cylindrical symmetry, however, are intrinsically difficult to solve, mathematically. Several papers have dealt with transient thermal stress problems in thermo-viscoelastic media with a cylindrical symmetry using various numerical methods.[6.3,6.5-6.12] The solutions to some special cases of cylindrical symmetry have been analytically obtained.[6.3,6.5,6.12] Also numerical approaches, such as the finite different, finite element, and boundary element methods have been used lately.[6.7-6.10] However, the temperature dependence of thermal properties, such as thermal conductivity, thermal diffusivity and/or specific heat, and coefficient of linear thermal expansion, have not

been considered in these papers, despite the fact almost all thermo-viscoelastic materials are well known to also have temperature-dependent thermal properties.[6.13] Some papers have dealt with the temperature-dependent coefficient of linear thermal expansion and thermal conductivity, but thermal diffusivity and/or specific heat have been assumed to be independent of temperature. This is because the heat conduction equation with temperature-dependent thermal diffusivity have not been solved mathematically. Although various numerical approaches to this heat conduction problem have been suggested,[6.14-6.18] the problem of transient thermo-viscoelastic stress field with a cylindrical symmetry in a temperature field with temperature-dependent thermal properties is still difficult to analyze due to nonlinearity in both fields. It is still interesting to investigate the effect of temperature dependence of thermal properties on thermal stress in thermo-viscoelastic media.

The fracture phenomenon in thermo-viscoelastic media has been theoretically and experimentally studied in the past decade. Schapery[6.19] and Christensen[6.20,6.21], respectively, proposed the fracture criteria for crack initiation and growth for viscoelastic materials. Their criteria were based on an energy balance theory[6.22], and the fracture initiation time could be predicted according to each criterion by using the inherent fracture energy of the materials, which is supposed to be inherently constant. Moreover, to better understand the fracture phenomenon, many researchers had theoretically extended these criteria and had numerically analyzed various fracture problems dealing with thermo-viscoelastic materials.

However, as was shown in Chapter 3 and 4, and also in several papers[6.28-6.33], a fracture property of thermo-viscoelastic material was inherently variable due to time-temperature dependence. It was also shown that the master curves of the fracture toughness by applying the shift factor of the dynamic moduli according to the time-temperature equivalence principle. Both the time-temperature dependences of stress field and fracture toughness, therefore, must be considered when the fracture problems in the thermo-viscoelastic media are analyzed.

The purpose of the present chapter is to propose a method for predicting fracture initiation time for thermo-viscoelastic media with time-temperature dependent fracture toughness. In Section 6.2, I analyze the thermal stress on a thermo-viscoelastic hollow cylinder with temperature-dependent thermal properties. The cylinder is heated gradually at the inner surface and kept at the initial temperature at the outer surface. The cylinder material is thermo-rheologically simple and has a temperature-dependent coefficient of linear thermal expansion, thermal conductivity, and thermal diffusivity (and/or specific heat). I discussed the stress field with time-temperature dependence based on the analysis results. In Section 6.3, I propose a method to predict fracture initiation time for the thermo-viscoelastic media from stress field and the fracture toughness allowing for both time-temperature dependences. I explain concept of the method with the use of master curves of stress intensity factor and

fracture toughness which are derived according to the time-temperature equivalence principle. Then, as concrete examples, I analyze a stress intensity factor in a thermo-viscoelastic cylinder with a crack under various conditions of temperature and crack length and explain the process for prediction of fracture initiation time.

6.2 THERMAL STRESS ANALYSIS

6.2.1 Mathematical analysis

(A) Analytical model

I analyzed the thermal stress on a thermo-viscoelastic hollow cylinder with outer radius r_b and inner radius r_a. The thermal properties are dependent on temperature. The cylinder with initial temperature, T_0, is heated from the inner surface. The transient temperature is given at the inner surface, and the temperature at the outer surface is kept constant as T_0. Assumed that the cylinder is sufficiently long, the temperature and stress fields are axisymetric and in the plane strain state. The temperature and stress fields are expressed as a function of cylindrical coordinate (r, θ) and the actual time, t.

(B) Transient temperature field

Considered that thermal conductivity, λ, varies with temperature $T(r, t)$, the equation for heat conduction is given as follows:[6.15]

$$\frac{1}{r}\frac{\partial}{\partial r}\left(\lambda(\Theta) r \frac{\partial \Theta}{\partial r}\right) - c_\rho(\Theta)\frac{\partial \Theta}{\partial t} = 0, \qquad (6.1)$$

where

$$\Theta = T - T_0.$$

λ and c_ρ are thermal conductivity and specific heat per unit volume dependent on temperature, respectively. Equation (6.1) is non-linear because of the temperature dependence of λ and possibly that of c_ρ. Applying Kirchhoff's transformation,

$$\Lambda(r,t) = \int_0^\Theta \frac{\lambda(\Theta')}{\lambda_0} d\Theta', \qquad (6.2)$$

where λ_0 is thermal conductivity at $\Theta = 0$, Eq. (6.1) can be linearized as the following equation for transformed temperature Λ,

$$\frac{\partial^2 \Lambda}{\partial r^2} + \frac{1}{r}\frac{\partial \Lambda}{\partial r} - \frac{1}{k}\frac{\partial \Lambda}{\partial t} = 0, \qquad (6.3)$$

where k is thermal diffusivity,

$$k = \frac{\lambda}{c_\rho}. \qquad (6.4)$$

To completely linearize Eq. (6.3), variable ψ defined as the following transformation

is induced.

$$\Psi(r,t)=\int_0^t \frac{k(\Theta)}{k_0}\,dt' \quad , \tag{6.5}$$

where k_0 is thermal diffusivity at $\Theta = 0$. Equation (6.5) is finally obtained as,

$$\frac{\partial^2\Lambda}{\partial r^2}+\frac{1}{r}\frac{\partial\Lambda}{\partial r}-\frac{1}{k_0}\frac{\partial\Lambda}{\partial\psi}=0. \tag{6.6}$$

For a temperature field only concerned with ψ related to t, Eq. (6.6) can be solved exactly by taking the Laplace transform with respect to ψ. For a transient non-isothermal state such as in this model, on the other hand, it is quite difficult to obtain analytical solutions to Eq. (6.6). This is because time variable ψ depends on both t and r. Therefore, I directly analyzed Eq. (6.1) with variable thermal properties with the finite difference method (FDM). (See in Appendix A6)

(C) Transient thermal stress field

For the quasi-static, axisymetric and plane strain problem, the equilibrium equation of stress σ_{ij} is given as,

$$\frac{\partial\sigma_{rr}}{\partial r}+\frac{\sigma_{rr}-\sigma_{\theta\theta}}{r}=0. \tag{6.7}$$

The constitutive equations for thermo-viscoelastic material, which is thermo-rheologically simple, are given as follows,[6.3]

$$\sigma_{rr}(r,t)=\int_0^t\left[\frac{E_{\mathrm{rR}}\left(\xi(t)-\xi(t')\right)}{(1+\nu)(1-2\nu)}\frac{\partial}{\partial t'}\left\{(1-\nu)\frac{\partial u_r}{\partial r}+\nu\frac{u_r}{r}-(1+\nu)\Omega\right\}\right]dt' \quad , \tag{6.8a}$$

$$\sigma_{\theta\theta}(r,t)=\int_0^t\left[\frac{E_{\mathrm{rR}}\left(\xi(t)-\xi(t')\right)}{(1+\nu)(1-2\nu)}\frac{\partial}{\partial t'}\left\{(1-\nu)\frac{u_r}{r}+\nu\frac{\partial u_r}{\partial r}-(1+\nu)\Omega\right\}\right]dt' \quad , \tag{6.8b}$$

where u_r is radial displacement and ν is Poisson's ratio assumed to be constant. ξ is reduced time and E_{rR} is relaxation modulus. ξ, E_{rR}, and Ω are given by,

$$\xi(r,t)=\int_0^t\left[a_{T\mathrm{R}}\left(\Theta(r,t')\right)\right]dt' \quad , \tag{6.9a}$$

$$E_{\mathrm{rR}}\left(\xi(r,t);\Theta_{\mathrm{R}}\right)=E_{\mathrm{r}}\left(t;\Theta(r,t)\right), \tag{6.9b}$$

$$\Omega(r,t)=\int_0^{\Theta}\left[\alpha\left(\Theta'(r,t)\right)\right]d\Theta' \quad , \tag{6.9c}$$

where a_T and E_r are shift factor and relaxation modulus, and α is the coefficient of linear thermal expansion dependent on temperature. Subscript R expresses a function for reduced time at standard temperature in the time-temperature equivalence principle. Substituting Eq. (6.8) into Eq. (6.7) gives Navier's equation of thermo-viscoelastic material with respect to displacement u_r. For an isothermal field or steady temperature field, Navier's equation can be solved analytically by taking the Laplace transform with respect to ξ. it is quite difficult to obtain analytical solutions for a transient non-isothermal state. This is because reduced time ξ depends on both t and r, so that the problem cannot be mathematically expressed as a single integral equation. This is similar non-linearity to the heat conduction equation of Eq. (6.6). Therefore, the thermal stress field of a thermo-viscoelastic cylinder in a transient non-isothermal state is also treated directly with FDM, similar to analyzing of the temperature field. (See in Appendix B6)

6.2.2 Material properties

(A) Thermo-viscoelasticity

The material properties of Epoxy A in Chapter 3, which was post-cured at 413 K for 10 h, was adopted to the present analysis. And the thermo-viscoelastic properties obtained was used for the present analysis. The master curves of the dynamic moduli E', E'', and the shift factor a_T at $T_R = T_g$ were shown in Figs. 3.1 and 3.5 in Chapter 3. I derived the relaxation modulus E_r by taking the Fourier inverse transform of E' and E'' as follows,

$$E_r(t) = \frac{1}{2\pi}\int_{-\infty}^{+\infty}\left[\{E' + iE''\}\exp(i\omega t)\right]d\omega, \tag{6.10}$$

where $i = \sqrt{-1}$ and ω was angular frequency.

(B) Thermal diffusivity, thermal conductivity, and specific heat

I measured the temperature dependence of thermal diffusivity, k, specific heat per volume, c_ρ, and thermal conductivity, λ, of the epoxy resin with Krischer's method.[6.34] The measurement unit is schematically shown in Fig. 6.1. The unit piled up consisted of eight epoxy resin plates with dimensions of 100 × 100 × 10 mm. A nichrome leaf heater was inserted into every other layer. T-type thermocouples (Cu-Co) were inserted into the upper side (insulated side) and lower side (heated side) of the 5th layer from the top. The unit was placed in the thermostatic oven to prevent large temperature differences between the unit and the environment. It was heated from 298 to 433 K to evaluate the temperature dependence of the thermal properties. Assuming that $kt/\lambda^2 > 0.6$ and heat flowed only in vertical direction, z, without heat loss from any side of the unit, the temperature distribution in the 5th layer is approximately given as follows:

$$T(z,t) = T_s + \frac{q_0 l}{\lambda}\left\{\frac{z^2}{2l^2} + \frac{kt}{l^2} - \frac{1}{6}\right\}, \qquad (6.11)$$

where T_s is the temperature at the start of measurement. l and z are the thicknesses of each epoxy resin plate and the position from the bottom of the 5th plate. q_0 is given from the electrical power of the nichrome heater:

$$q_0 = \frac{VI}{8A}, \qquad (6.12)$$

where A is an area heated by the nichrome leaves. V and I are voltage applied to the whole system and current. In the experiment, voltage V was 20 V constantly, and the histories of T and I at both sides of the 5th layer were measured. Using Eqs. (6.4), (6.11), and (6.12), c_ρ was derived from the slope of the temperature history curve, and λ from the time difference between the temperature history curves of both sides in the 5th layer.

The experimental results for k and c_ρ are plotted in Fig. 6.2. Below T_g (= 392 K), k slightly decreases with temperature while c_ρ increases. At the vicinity of T_g, these thermal properties greatly changed.

(C) Coefficient of thermal expansion property

The coefficient of linear thermal expansion α for the epoxy resin was measured with a thermal mechanical analyzer (Thermo Plus2/ TMA8310, Rigaku). The specimen was 4.0 × 6.0 × 10.0 mm. Quartz was used as a reference sample. Probes were rested on the surface of the specimen and the reference sample under low loading condition of 0.01 N. The specimen was heated from 293 to 473 K at a heating rate of 5 K/min in an air-static atmosphere. Elongation in the specimen was measured every 1K. α was determined from the slope of the thermal expansion-temperature curve. Temperature variations in α are plotted in Fig. 6.3. α increases with temperature, and then drastically changes from 80×10^{-6} to 180×10^{-6} /K around T_g.

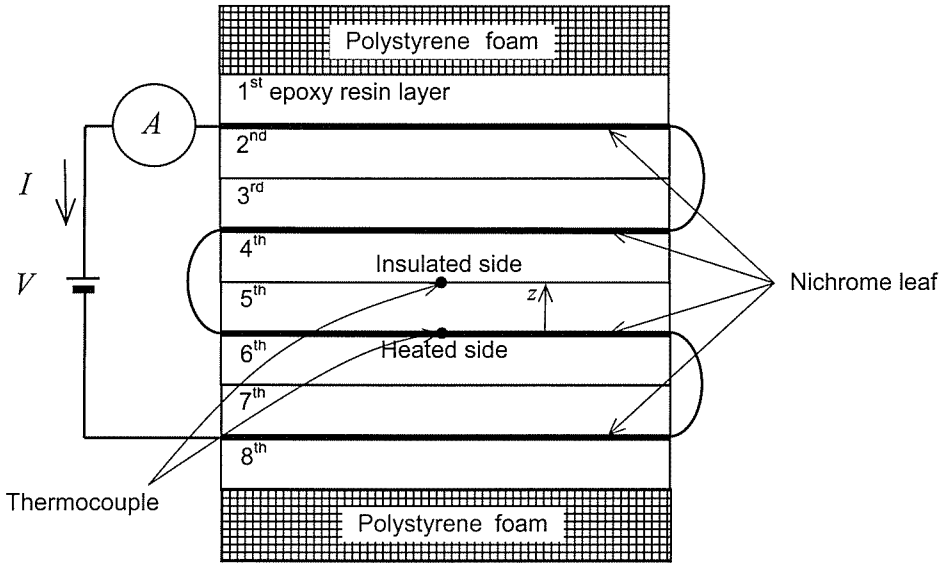

Figure 6.1 Measurement unit based on Krischer's method.

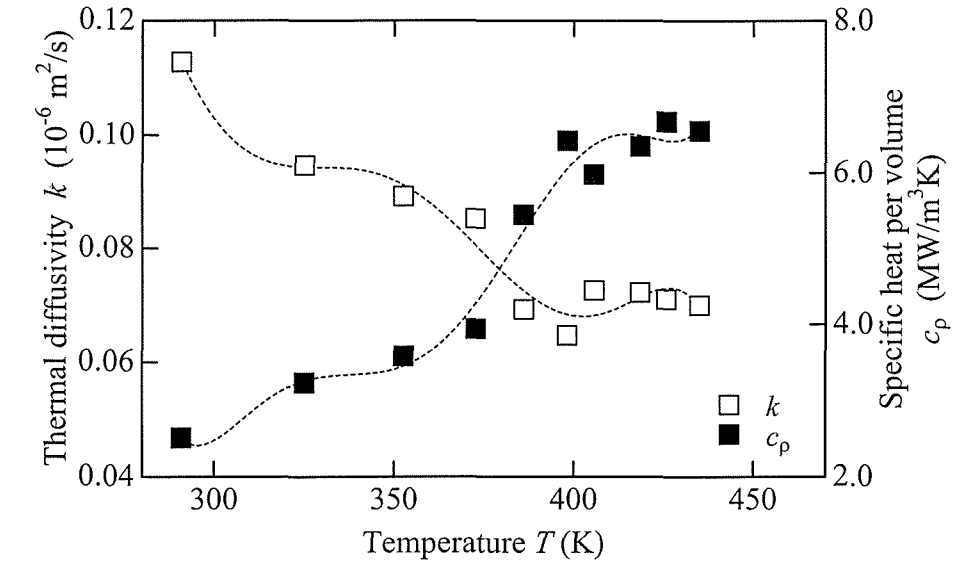

Figure 6.2 Dependence of thermal diffusivity and specific heat on temperature.

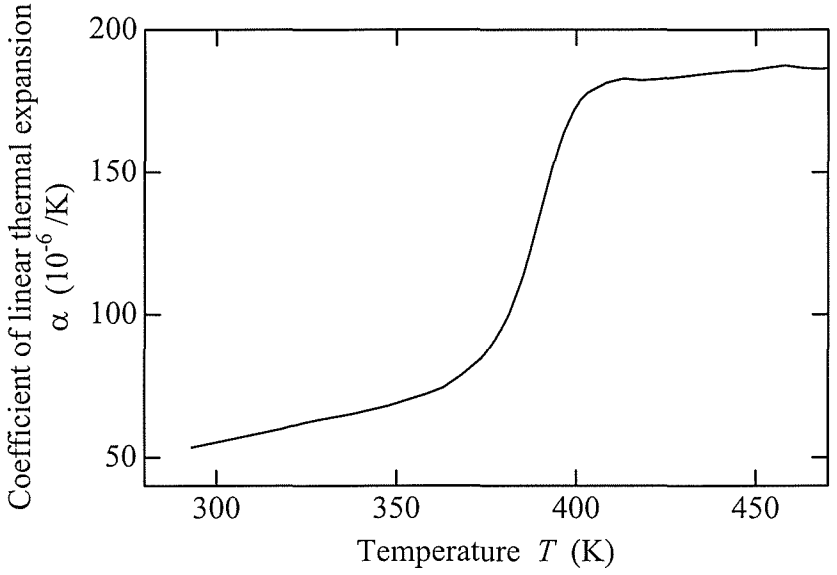

Figure 6.3 Dependence of coefficient of linear thermal expansion on temperature.

6.2.3 Conditions for numerical analysis

The object of analysis was a thermo-viscoelastic cylinder heated on its inner surface. Inner radius r_a ranged from 1 to 50 mm when the ratio of inner and outer radii r_a/r_b is constant at 0.5. Initial temperature T_0 was 298 K and outside temperature T_b was kept at T_0. The gradually increase temperature applied at the inner surface is given as follows:

$$T(t) = T_0 + (T_a - T_0) \cdot \left\{ 1 - \exp\left(-\frac{t}{\tau_a} \right) \right\} \quad \text{at } r = r_a , \qquad (6.13)$$

where τ_a was constant at 100 s and T_a ranged from 323 to 398 K. The geometric and temperature conditions are summarized in Table 6.1. Every surface was free of traction for the boundary conditions. The thermo-viscoelasticity of Epoxy A in Chapter 3 and the thermal properties obtained above were used for the present analysis.

6.2.4 Results and discussion

(A) Transient fields of temperature and stress

Figure 6.4 shows one of the typical results for $r_a = 1$ mm and $T_a = 398$ K. As time passes from 0 to 500 s, temperature propagates outwards (Fig. 6.4(a)). After 500 s, the temperature field almost reaches a steady state. Transient reduced time, ξ, at standard temperature, $T_R = 298$K, increases and relaxation modulus E_r decreases with passing time in Figs. 6.4(b) and (c). The changes in ξ and E_r are drastic especially near the heated inner surface. Although radial displacement u_r increases and the cylinder expands outwards until 250 s, it shrinks inward slightly after 250 s (Fig. 6.4(d)). Figures 6.4(e) and (f) show the transient distributions of radial stress σ_{rr} and hoop stress $\sigma_{\theta\theta}$. σ_{rr} is always compressive everywhere and its absolute value is much smaller than that of $\sigma_{\theta\theta}$. Compressive radial stress increases with passing t and reaches a maximum at 230 s around r = 1.4 mm. After that, it decreases slightly because of the relaxation in stress. $\sigma_{\theta\theta}$ is compressive near the inside and tensile and outside surfaces. The absolute value of $\sigma_{\theta\theta}$ increases and the compressive region extends outwards. After 100 s, stress relaxation in the vicinity of the inner surface rapidly occurs, while stress distribution in the other region gradually changes due to relaxation phenomena. Even when the temperature field is in a steady state, these stress distributions change continually.

Figure 6.5 shows the results for r_a= 10 mm and T_a= 398 K. These transient distributions are similar to the ones in Fig. 6.4. The effect of relaxation phenomena on stress in Fig. 6.5 is larger than that in Fig. 6.4, even though the heating temperature is the same. For example, the maximum tensile value for $\sigma_{\theta\theta}$ in Fig. 6.5(f) is about 7.8 MPa at 290 s while that in Fig. 6.5(f) is about 7.4 MPa at 620 s. The values for maximum tensile hoop stress and also compressive radial stress are greatly influenced by the relaxation phenomena. In the following

sections, I will discuss the effect of thermo-viscoelastic relaxation on their maximum values.

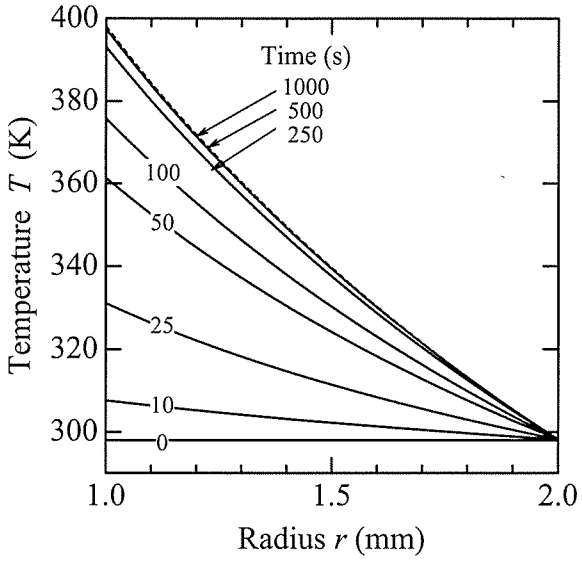

(a) Temperature

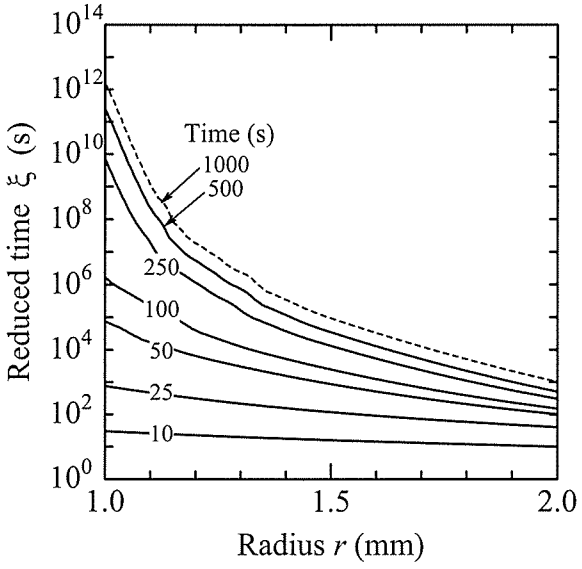

(b) Reduced time (T_R = 298 K)

Figure 6.4 Analysis results for the case of r_a = 1 mm and T_a = 398 K (Continued)

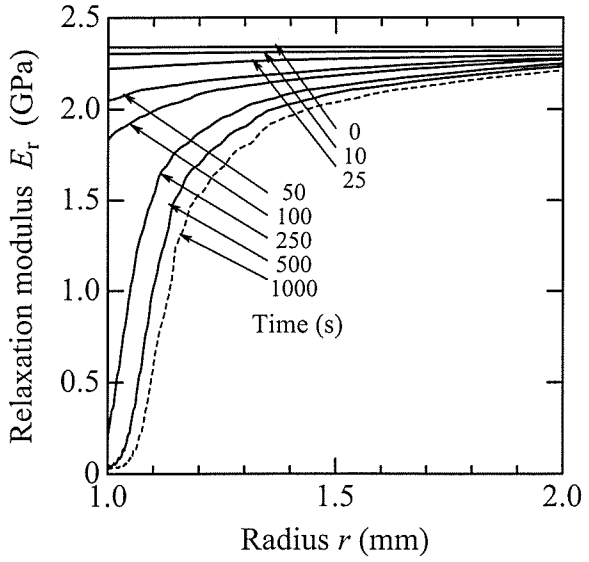

(c) Relaxation modulus

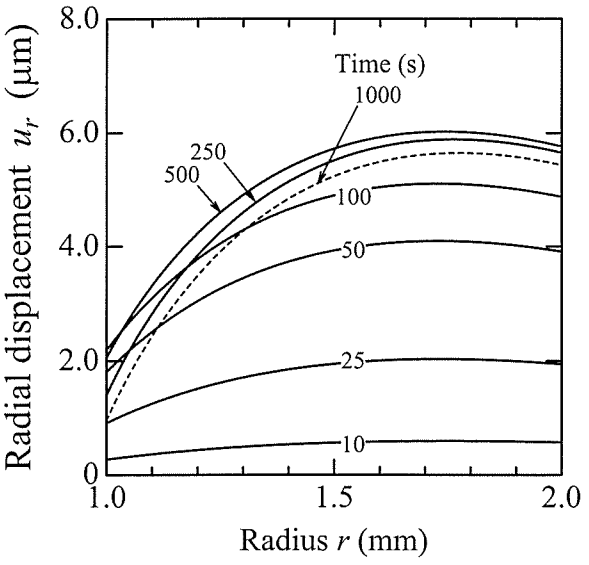

(d) Radial displacement

Figure 6.4 Analysis results for the case of $r_a = 1$ mm and $T_a = 398$ K (Continued)

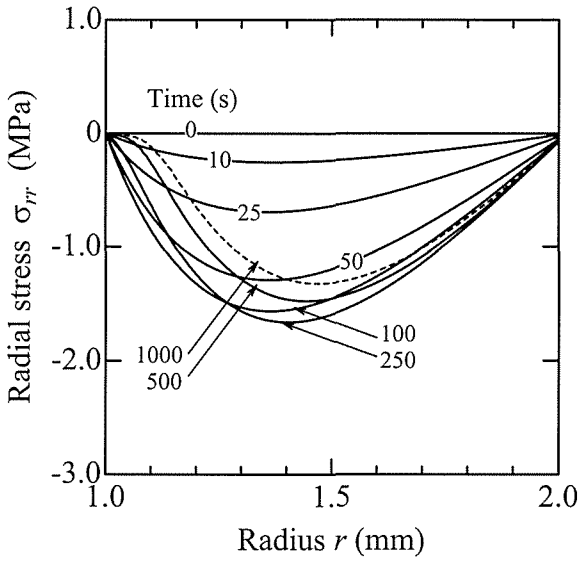

(e) Radial stress

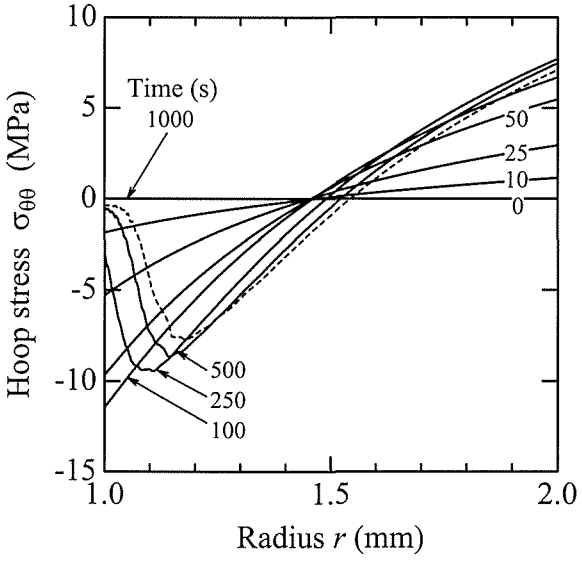

(f) Hoop stress

Figure 6.4 Analysis results for the case of $r_a = 1$ mm and $T_a = 398$ K.

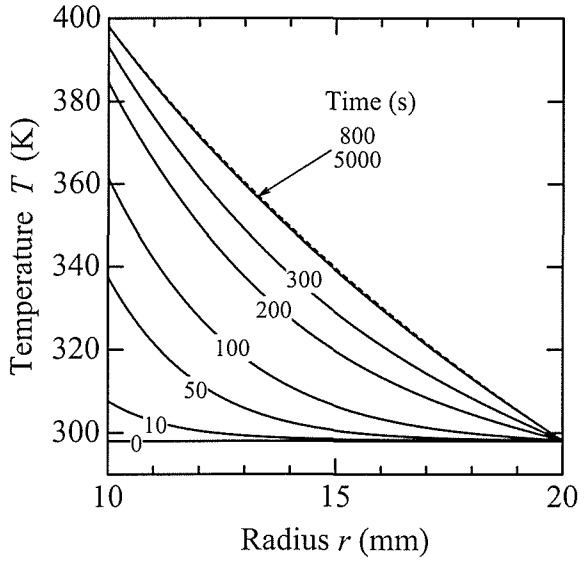

(a) Temperature

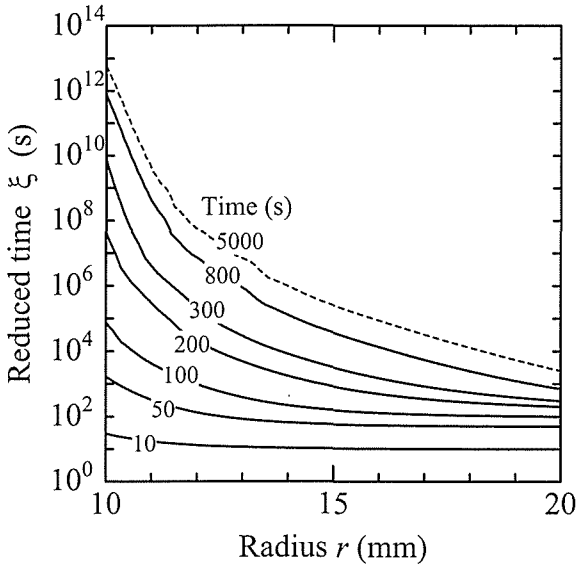

(b) Reduced time (T_R = 298 K)

Figure 6.5 Analysis results for the case of r_a = 10 mm and T_a = 398 K (Continued)

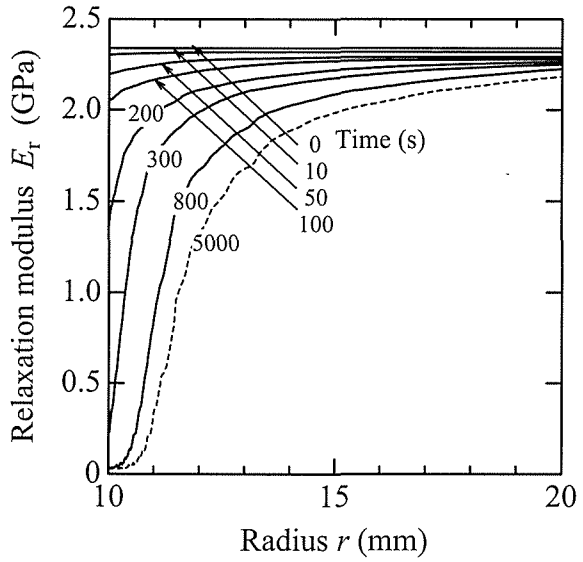

(c) Relaxation modulus

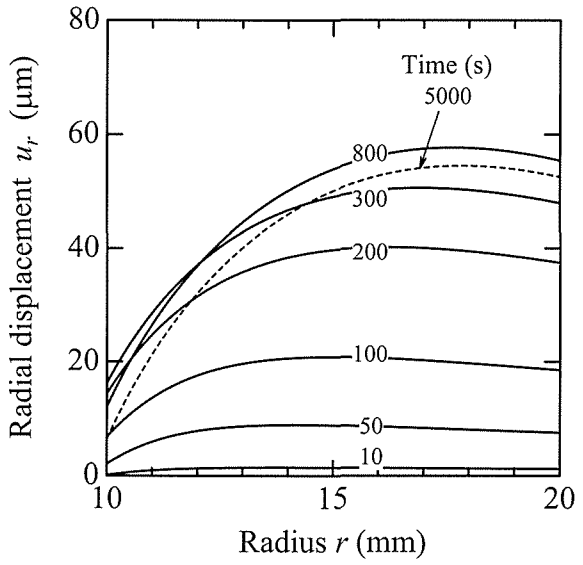

(d) Radial displacement

Figure 6.5 Analysis results for the case of $r_a = 10$ mm and $T_a = 398$ K (Continued)

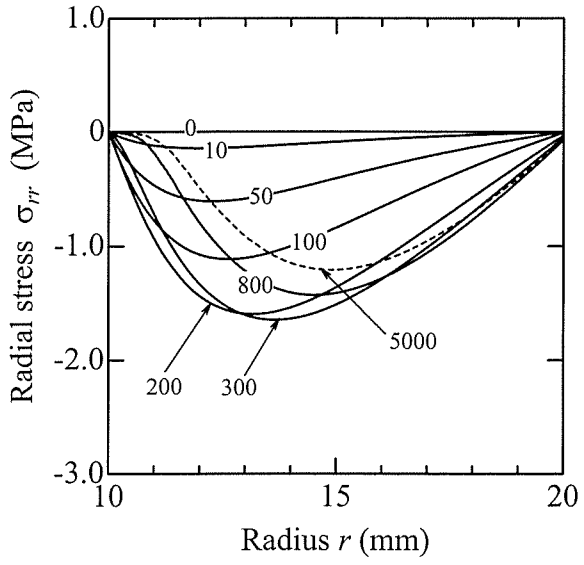

(e) Radial stress

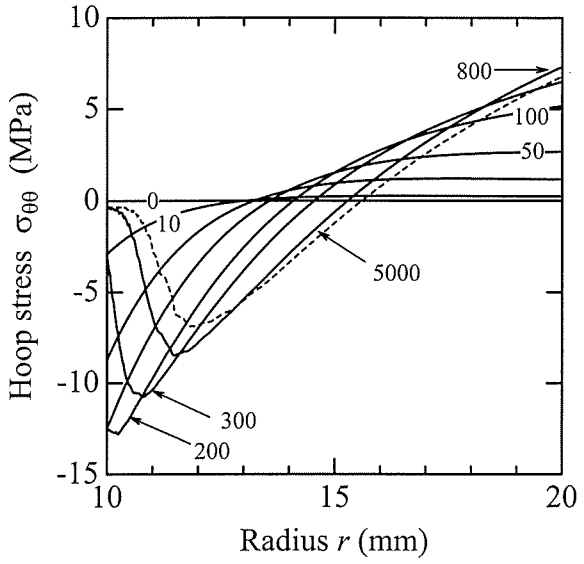

(f) Hoop stress

Figure 6.5 Analysis results for the case of $r_a = 10$ mm and $T_a = 398$ K.

(B) Maximum compressive radial stress

Figure 6.6 shows the typical distributions for temperature and radial stress, σ_{rr}, at time t_{rc}^{max}, at which σ_{rr} has reached its compressive maximum. Normalized position $(r-r_a)/(r_b-r_a)$ where σ_{rr} has reached maximum slightly changes being dependent on both cylinder size, r_a, and heating temperature T_a. Under the same heating temperature conditions (T_a = 398 K) in Fig. 6.6, σ_{rr} reaches a larger compressive maximum in a shorter time as r_a is smaller. The stress relaxation phenomenon appears near the inner surface at r_a, especially in a large cylinder. Compared with the same size cylinders (r_a = 50 mm) in Fig. 6.7, σ_{rr} reaches a larger compressive maximum as T_a is higher. The effect of stress relaxation around r_a is clearly evident under high heating temperature conditions. As time t_{rc}^{max} is not long, the temperature distribution varies transitionally at t_{rc}^{max} in large cylinders.

The maximum compressive radial stress σ_{rc}^{max} and t_{rc}^{max} are shown in Fig. 6.8. As previously mentioned, compressive maximum value σ_{rc}^{max} is smaller and t_{rc}^{max} is longer, as r_a is larger under the same T_a. This size-effect becomes more obvious for a higher T_a.

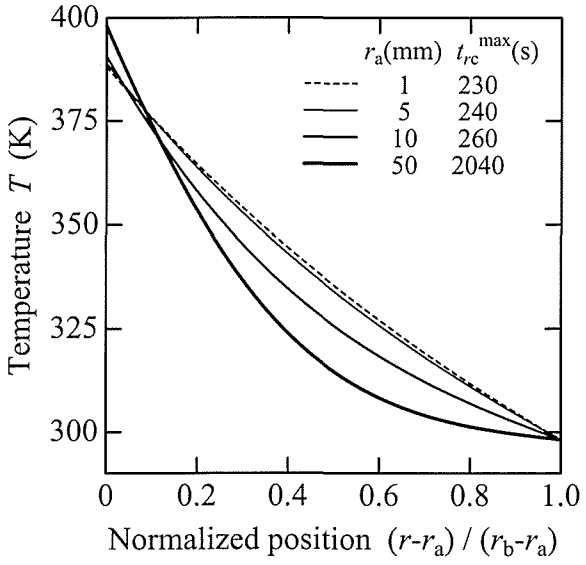

(a) Temperature

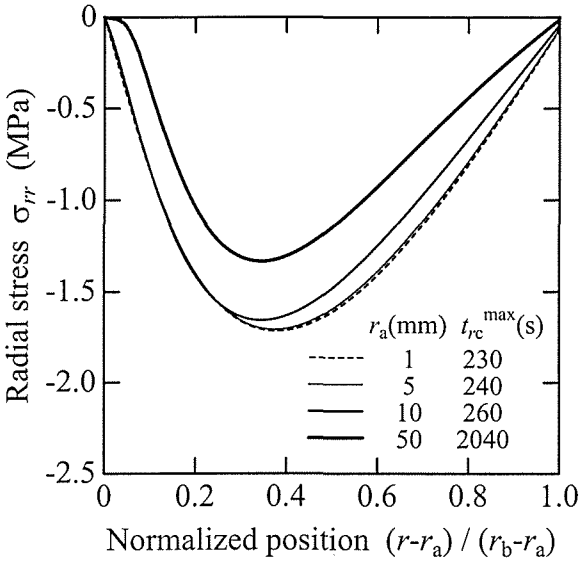

(b) Radial stress

Figure 6.6 Transient temperature and radial stress distributions at t_{rc}^{max} for the case of T_a = 398 K.
(t_{rc}^{max} is time when radial stress has reached its compressive maximum.)

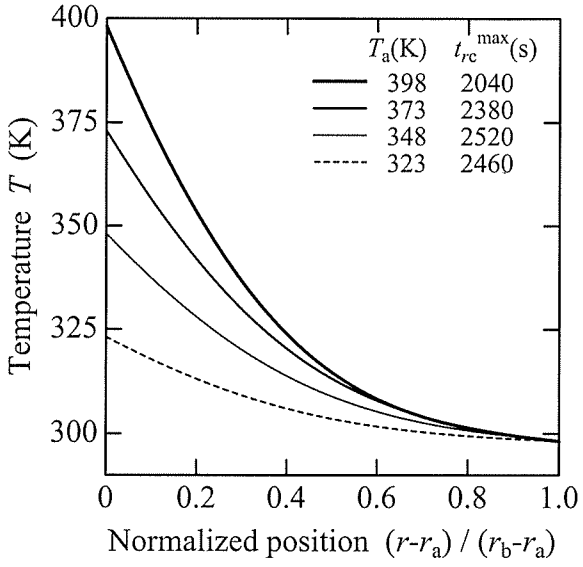

(a) Temperature

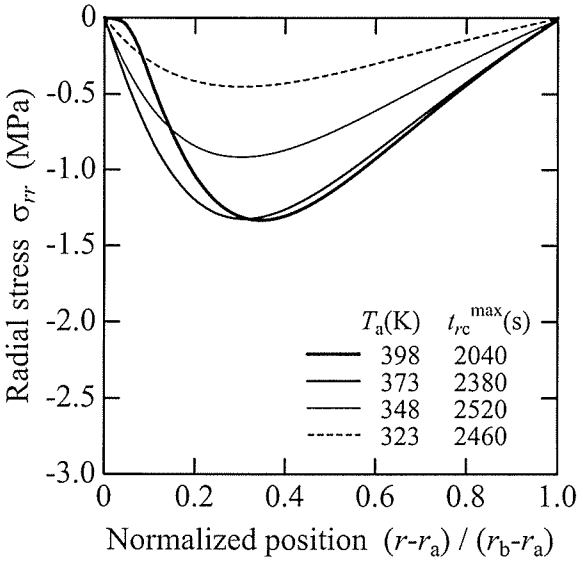

(b) Radial stress

Figure 6.7 Transient temperature and radial stress distributions at t_{rc}^{max} for the case of r_a = 50 mm.
(t_{rc}^{max} is time when radial stress has reached its compressive maximum.)

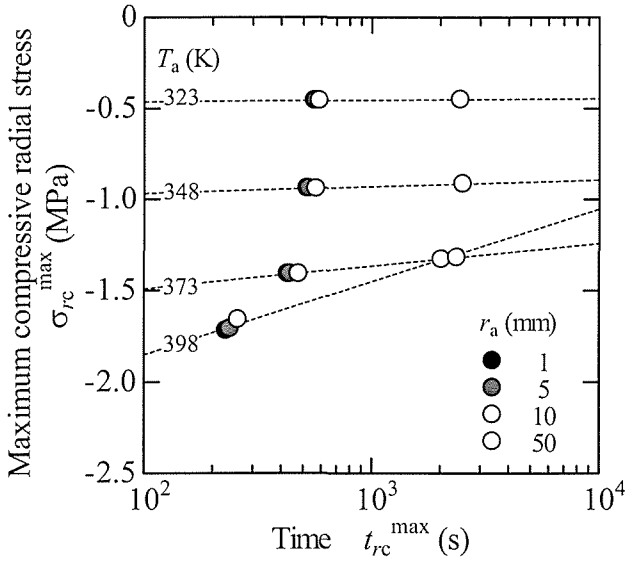

Figure 6.8 Maximum compressive radial stress.

(C) Maximum tensile hoop stress

Figure 6.9 shows the distributions of temperature and hoop stress $\sigma_{\theta\theta}$ at time $t_{\theta c}^{max}$, at which $\sigma_{\theta\theta}$ has reached tensile maximum at the outer surface. Tensile hoop stress $\sigma_{\theta\theta}$ has a maximum at r_b and the temperature distribution achieves almost a steady state at $t_{\theta c}^{max}$, regardless of cylinder size r_a or heating temperature T_a. Under the same heating temperature conditions (T_a = 398 K) in Fig. 6.9, $\sigma_{\theta\theta}$ reaches a larger maximum in a shorter time as r_a is smaller. Compared with the same size cylinders (r_a = 50 mm) in Fig. 6.10, $\sigma_{\theta\theta}$ reaches a larger tensile maximum in a shorter time as T_a is higher. Local relaxation near the inner surface is particularly evident in a larger sizes and under high heating temperature conditions.

The maximum values of tensile hoop stress $\sigma_{\theta t}^{max}$ and $t_{\theta t}^{max}$ are shown in Fig. 6.11. Tensile maximum value $\sigma_{\theta t}^{max}$ is smaller and $t_{\theta t}^{max}$ is longer as r_a is larger under the same T_a conditions, and this size-effect becomes more obvious at higher T_a, which is similar to the results in Fig. 6.8. This is because stress relaxation occurs during temperature conduction as can be seen in Figs. 6.4 and 6.5. The time required for a temperature steady-state mostly depends on r_a. The time is longer as r_a is larger. Thus, the stress relaxation at r_a, possibly throughout the whole cylinder, significantly affects $\sigma_{\theta t}^{max}$ in a large cylinder. Moreover, the time required for stress relaxation to occur greatly depends on T_a. High heating temperature facilitates stress relaxation. Therefore, the effect of stress relaxation on $\sigma_{\theta t}^{max}$ becomes larger as r_a is larger and when T_a is higher.

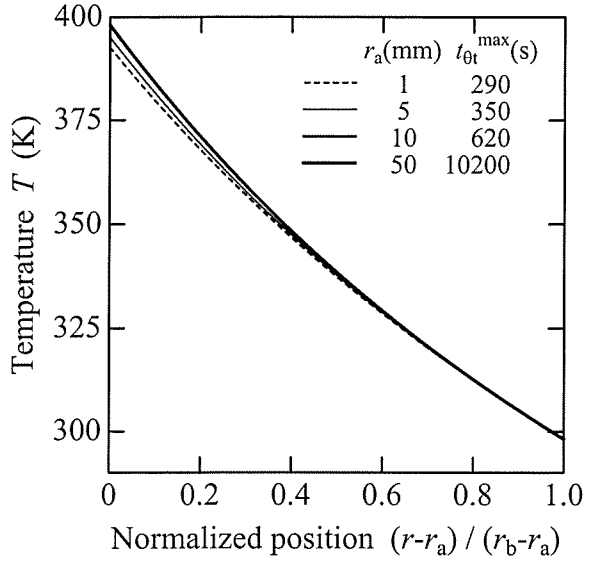

(a) Temperature

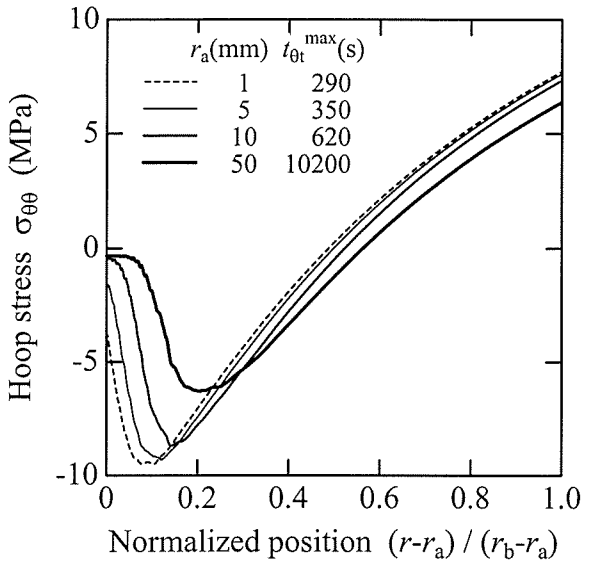

(b) Hoop stress

Figure 6.9 Transient temperature and hoop stress distributions at $t_{\theta t}^{max}$ for the case of T_a = 398 K.
($t_{\theta t}^{max}$ is time when hoop stress has reached its tensile maximum at outer surface.)

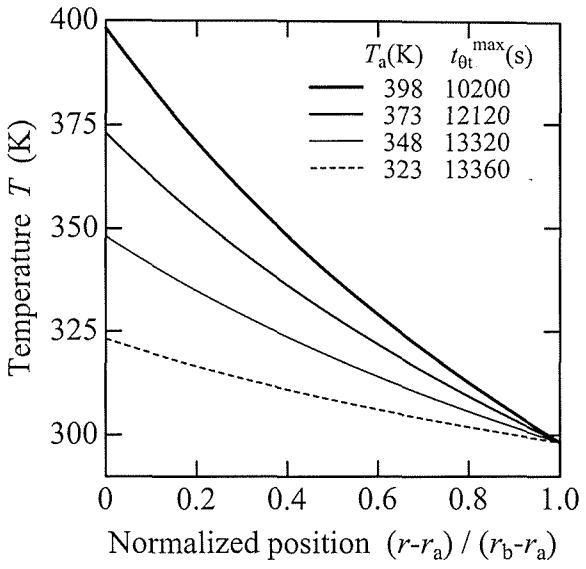

(a) Temperature

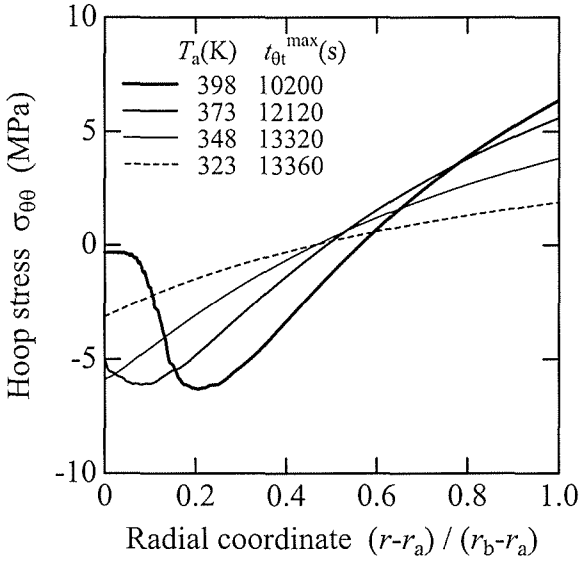

(b) Hoop stress

Figure 6.10 Transient temperature and hoop stress distributions at $t_{\theta t}^{max}$ for the case of r_a = 50 mm.
($t_{\theta t}^{max}$ is time when hoop stress has reached its tensile maximum at outer surface.)

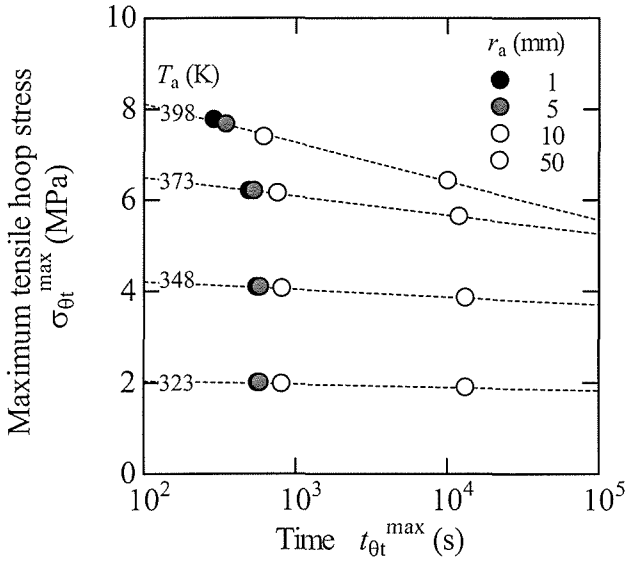

Figure 6.11 Maximum tensile hoop stress.

(D) Effect of temperature-dependence of thermal properties

To consider the effect of temperature dependency of thermal properties on the stress distribution, I also conducted numerical analysis with constant thermal properties λ_0 and $c_{\rho 0}$. Constant thermal properties λ_0 and $c_{\rho 0}$ were 0.28×10^{-6} m^2/s and 2.51×10^6 W/m^{3}K, which are epoxy resin properties at T_0 (298 K). I also analyzed using a constant coefficient of linear thermal expansion, $\alpha_0 = 5.48 \times 10^{-5}$ /K.

Figures 6.12 and 6.13 show the typical distributions of temperature and hoop stress $\sigma_{\theta\theta}$ in an unsteady temperature state. In these figures, the notations with T in parenthesis mean temperature-variable properties, e.g. $\lambda(T)$ denotes analysis results with temperature-variable thermal conductivity. For the large cylinder with r_a = 50 mm in Fig. 6.12, temperature conduction with λ_0 and $c_{\rho 0}$ is slightly faster than that with $\lambda(T)$ and $c_\rho(T)$, because heat diffusivity $k(T)$, namely temperature conductivity, decreases with increasing T as can be seen in Fig. 6.2. Thus, the temperature-dependence of λ and c_ρ has limited influence on the stress distribution. For the small cylinder with r_a = 1 mm in Fig. 6.13, temperature and stress distributions are almost the same, regardless of the temperature dependence of thermal properties. This is because the absolute value of k is small and the cylinder size is sufficiently small for temperature conduction.

Therefore, there is a little effect of temperature-dependence of thermal properties such as λ, k, and c_ρ only for the case of a large cylinder. In contrast, the temperature-dependence of α directly affects stress distribution.

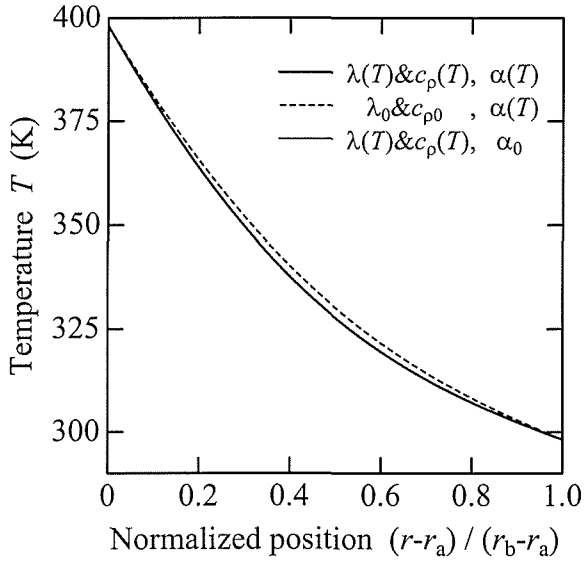

(a) Temperature

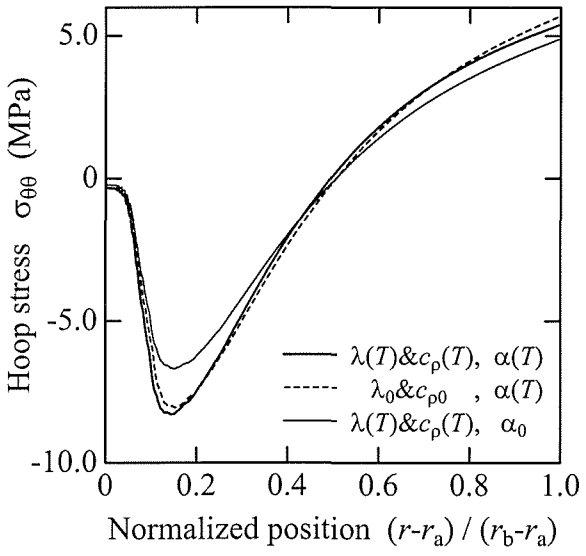

(b) Hoop stress

Figure 6.12 Effect of temperature dependency of thermal properties at 4000 s for the case of r_a = 50 mm, T_a = 398 K.

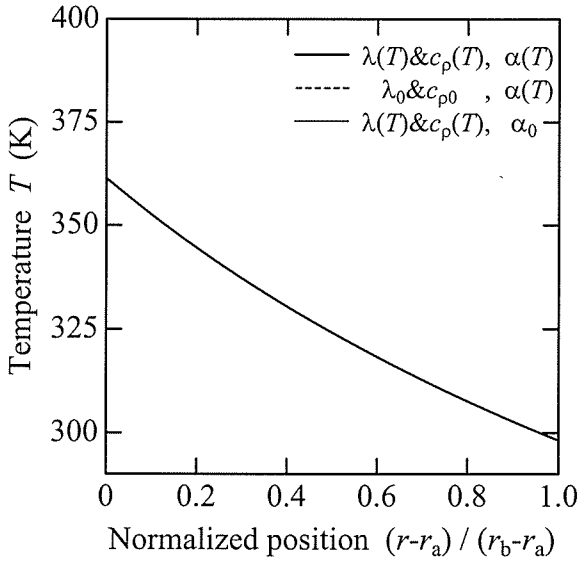

(a) Temperature

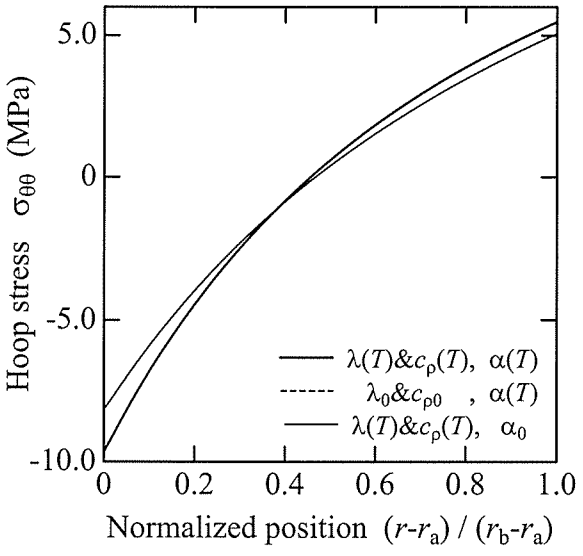

(b) Hoop stress

Figure 6.13 Effect of temperature dependency of thermal properties at 100 s for the case of r_a = 1 mm, T_a = 398 K.

(E) Effect of thermo-viscoelasticity

To clarify the effect of thermo-viscoelasticity on maximum tensile hoop stress $\sigma_{\theta t}^{max}$, I also did numerical analysis on an elastic cylinhder heated from its inner surface. The elastic material was assumed to have a constant elastic modulus, E_0, of 2.34 GPa, which is the epoxy resin's modulus at T_0, and the temperature-variable properties of the epoxy resin. I obtained maximum tensile hoop stress $\sigma_{\theta tE}^{max}$ from this elastic analysis.

Figure 6.14 shows the typical results for hoop stress distribution at $t_{\theta t}^{max}$ obtained from thermo-viscoelastic and elastic analyses of cylinders of different sizes. Remarkable local stress relaxation can be seen around the inner surface in a large thermo-viscoelastic cylinder (Fig. 6.14(a)). Due to this local relaxation phenomenon, the maximum tensile hoop stress in a thermo-viscoelastic cylinder, $\sigma_{\theta t}^{max}$, is smaller than that of a elastic cylinder, $\sigma_{\theta tE}^{max}$. Comparing Fig. 6.14(a) with Fig. 6.14(b), the difference between $\sigma_{\theta t}^{max}$ and $\sigma_{\theta tE}^{max}$ is larger with larger r_a .

Figure 6.15 shows the relationship between r_a and $\sigma_{\theta t}^{max} / \sigma_{\theta tE}^{max}$ under different heating temperature conditions considering the effect of thermo-viscoelasticity on $\sigma_{\theta t}^{max}$. When $\sigma_{\theta t}^{max} / \sigma_{\theta tE}^{max}$ for T_a = 323K is around 0.9, the thermo-viscoelastic effect is not significant. As the heating temperature is higher, $\sigma_{\theta t}^{max} / \sigma_{\theta tE}^{max}$ decreases. This means that the thermo-viscoelastic effect is stronger. When $\sigma_{\theta t}^{max} / \sigma_{\theta tE}^{max}$ for T_a = 398 K has small values below 0.7, the thermo-viscoelasticity greatly affects $\sigma_{\theta t}^{max}$. I found that the time for thermo-viscoelastic stress relaxation to occur at the inner surface depends on the heating temperature, as previously mentioned. Moreover, $\sigma_{\theta t}^{max} / \sigma_{\theta tE}^{max}$ decreases as r_a is larger under the same heating temperature condition. This is because the time required for a temperature steady-state mostly depends on the cylinder size. This size-effect clearly appears under any heating temperature condition, even for a low T_a.

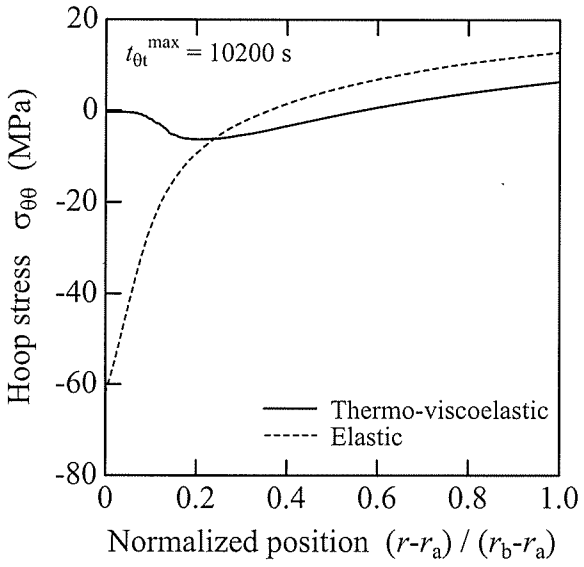

(a) r_a = 50 mm

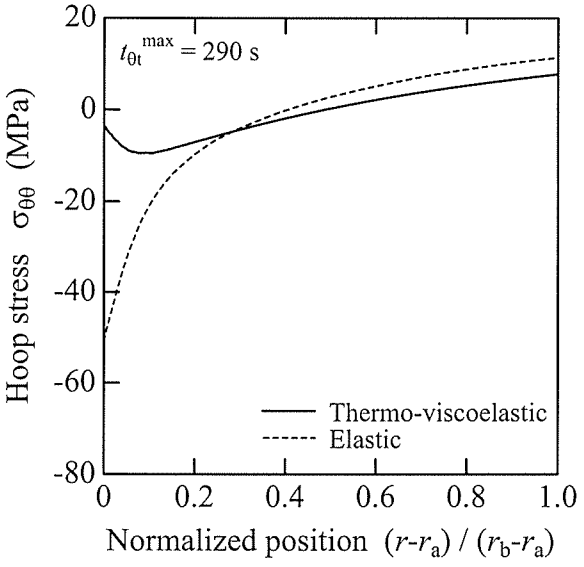

(b) r_a = 1 mm

Figure 6.14 Comparison between thermo-viscoelastic and elastic materials.

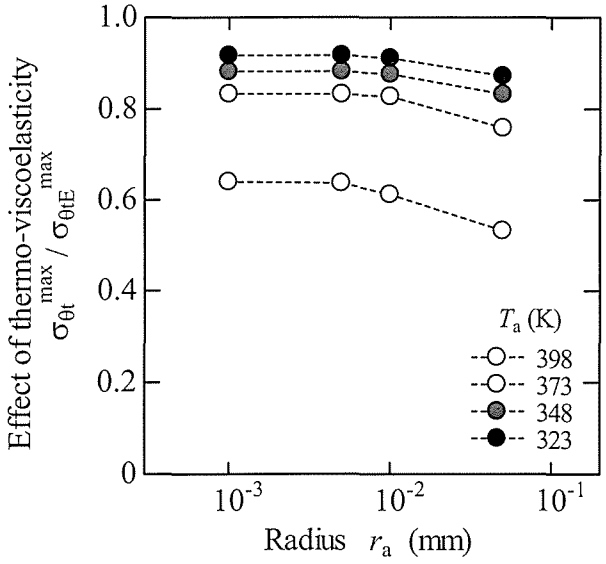

Figure 6.15 Effect of thermo-viscoelasticity on maximum tensile hoop stress.

6.3 PREDICTION OF FRACTURE INITIAION

6.3.1 Concept for predicting fracture initiaion

In Chapters 3 and 4, I have experimentally clarified that the time-temperature dependence of the fracture toughness, K_c, is similar to that of the dynamic storage modulus E'. The fracture toughness has the same shift factor as storage modulus E' concerning the fracture initiation time t_f, which means that

$$K_c\left(\xi_f\left(t_f\right);T_R\right)=K_c\left(t_f;T\left(t\right)\right), \qquad (6.14)$$

where ξ_f is the reduced time at the fracture initiation. (Eq. (6.9a))

Since the mechanical behavior depends on both time and on temperatures, the time-temperature dependences of fracture toughness and stress fields must then be considered for solving fracture problems dealing with thermo-viscoelastic media. Now I suggested a method to predict fracture initiation time t_f, which was the period from the start of the thermal and/or stress loading to the initiation of the crack propagation.

Figure 6.16 shows the concept for prediction as a flow chart. The fracture initiation time, t_f, in thermo-viscoelastic media is estimated as follows. First, the time-temperature dependence of material properties, such as relaxation modulus, E_r, (or complex modulus) and fracture toughness, was experimentally measured. If necessary, other mechanical and thermal properties, such as the Poisson's ratio, the linear thermal expansion coefficient, and the thermal conductivity could also be measured. The time-temperature equivalence principle was then applied to E_r to obtain the shift factor, $a_T(T; T_R)$ (Stage I in Fig. 6.16). Next, by using the measured material properties, a history of a stress field, $\sigma(t; T)$, near a crack tip was analyzed using a certain temperature field (Stage II). From the stress field around the crack tip, a history of the stress intensity factor, $K(t; T)$, was obtained (Stage III). This stress intensity factor, $K(t; T)$, was transferred to $K(\xi; T_R)$ for ξ at a standard temperature, T_R, by using a_T for the temperature history at the crack tip (Stage IV). Similarly, the fracture toughness, $K_c(t_f; T)$, was converted to $K_c(\xi_f; T_R)$ (Stage V). Then, the criterion for the fracture initiation was then given in the reduced time space by the following equation (Stage VI);

$$K_c\left(\xi_f\right)\le K\left(\xi\right) \text{ at } T_R. \qquad (6.15)$$

Eq. (6.13) evaluated ξ_f (Stage VII). By substituting ξ_f in Eq. (6.8), I should determine the actual fracture initiation time, t_f (Stage VIII).

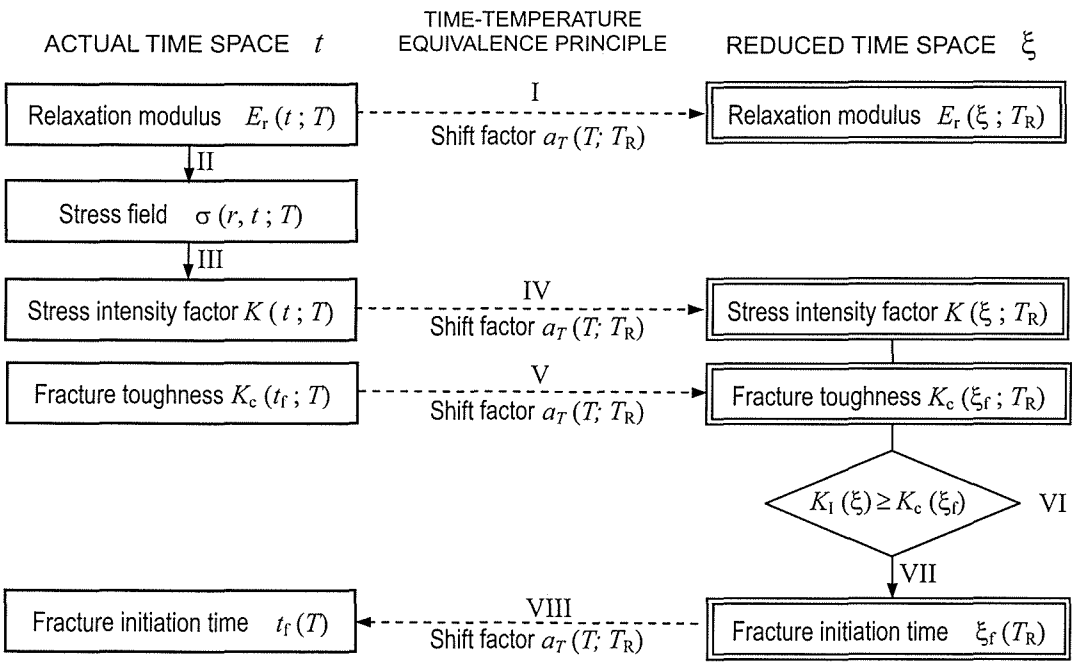

Figure 6.16 Concept for predicting fracture initiation in thermo-viscoelastic media.

6.3.2 Mathematical analysis

(A) Analytical model

As a concrete example of the proposed method, I mathematically and numerically analyzed the stress intensity factor for a thermo-viscoelastic cylinder with a crack. In the previous Section 6.2, the strong size-effect on stress field was obtained attributed to thermo-viscoelasticity, possibly the temperature-dependence of thermal properties, so that in this section, the temperature field is assumed to be an isothermal state to limit the discussion to time-temperature effect without the size-effect and also for ease of formulation. The main problem is the Mode I fracture in the plane strain state.

(B) Stress intensity factor

Stress components, σ_{ij}, in the thermo-viscoelastic hollow cylinder with a crack in an isothermal field can be expressed as a sum of two answers: stress field σ_{pij} for thermo-viscoelastic infinite media with a crack or dislocation, and stress field σ_{cij} for a hollow cylinder without a crack, that is,[6.35]

$$\sigma_{ij} = \sigma_{pij} + \sigma_{cij} \qquad (i,j=r,\theta). \tag{6.16}$$

First, consider a thermo-viscoelastic infinite plane with an edge dislocation having a Burger's vector ($b_v = -f$) at point $(r, \theta) = (v, 0)$. I know that isothermal thermo-viscoelastic problem of Laplace-transformation concerning the reduced time, ξ, are mathematically equivalent to elastic problems, which is called the correspondence principle.[6.3] Since the stress field is in a plane strain state, Airy's stress function Ψ_p in a Laplace-transformed region is expressed as

$$\Psi_p^* = -\frac{\zeta E_r^* f^*}{8\pi\left(1-\nu^2\right)}\left(r\cos\theta - v\right)\log\left(r^2+v^2-2rv\cos\theta\right), \tag{6.17}$$

where the superscript * means the Laplace-transformation concerning ξ is defined as,

$$\Psi^*(\zeta) = \int_0^{\zeta} \Psi(\xi)\exp(-\zeta\xi)\,d\xi .$$

From Eq. (6.17), the stress components obtained are

$$\sigma_{pr}^*(r,\theta,\zeta) = \frac{-\zeta E_r^* f^*}{4\pi\left(1-\nu^2\right)}\left[\frac{r\cos\theta - v - 2v\sin^2\theta}{r^2+v^2-2rv\cos\theta} - \frac{2v^2\sin^2\theta\left(r\cos\theta - v\right)}{\left(r^2+v^2-2rv\cos\theta\right)^2}\right], \tag{6.18a}$$

$$\sigma_{p\theta}^*(r,\theta,\zeta) = \frac{\zeta E_r^* f^*}{4\pi\left(1-\nu^2\right)}\left[\frac{\sin\theta\left(2v\cos\theta - r\right)}{r^2+v^2-2rv\cos\theta} - \frac{2v\sin\theta\left(r\cos\theta - v\right)\left(r-v\cos\theta\right)}{\left(r^2+v^2-2rv\cos\theta\right)^2}\right], \tag{6.18b}$$

$$\sigma^*_{p\theta\theta}(r,\theta,\zeta)=\frac{-\zeta E^*_r f^*}{4\pi(1-\nu^2)}\left[\frac{2\cos\theta(r-\nu\cos\theta)+r\cos\theta-\nu}{r^2+\nu^2-2r\nu\cos\theta}-\frac{2(r\cos\theta-\nu)\ (r-\nu\cos\theta)^2}{(r^2+\nu^2-2r\nu\cos\theta)^2}\right].$$

(6.18c)

Next, taking into account stress symmetry conditions, a thermo-viscoelastic solution for a general hollow cylinder without a crack is given by the following Airy's stress function Ψ_c:

$$\Psi^*_c=b^*_0\log r+c^*_0r^2+\left(\frac{c^*_1}{r}+d^*_1r^3\right)\cos\theta+\sum_{n=2}^{\infty}\left(a^*_nr^n+b^*_nr^{n+2}+c^*_nr^{-n}+d^*_nr^{2-n}\right)\cos n\theta, \quad (6.19)$$

where the coefficients $a_n,\ldots, d_n$ were determined by the boundary conditions. The stress components were therefore found to be

$$\sigma^*_{crr}(r,\theta,\zeta)=\frac{b^*_0}{r^2}+2c^*_0+\left(\frac{-2c^*_1}{r^3}+2d^*_1r\right)\cos\theta$$

$$+\sum_{n=2}^{\infty}\left[a^*_nn(n-1)r^{n-2}+b^*_n(n+1)(n-2)r^n+c^*_nn(n+1)r^{-n-2}+d^*_n(n-1)(n+2)r^{-n}\right]\cos n\theta,$$

(6.20a)

$$\sigma^*_{cr\theta}(r,\theta,\zeta)=\left(\frac{-2c^*_1}{r^3}+2d^*_1r\right)\sin\theta$$

$$+\sum_{n=2}^{\infty}\left[a^*_nn(n-1)r^{n-2}+b^*_n(n+1)r^n-c^*_nn(n+1)r^{-n-2}-d^*_n(n-1)r^{-n}\right]\sin n\theta, \quad (6.20b)$$

$$\sigma^*_{c\theta\theta}(r,\theta,\zeta)=\frac{-b^*_0}{r^2}+2c^*_0+\left(\frac{2c^*_1}{r^3}+6d^*_1r\right)\cos\theta$$

$$+\sum_{n=2}^{\infty}\left[a^*_nn(n-1)r^{n-2}+b^*_n(n+1)(n+2)r^n+c^*_nn(n+1)r^{-n-2}+d^*_n(n-1)(n-2)r^{-n}\right]\cos n\theta.$$

(6.20c)

When I consider that a crack was formed by distributing dislocations in the line of $r_c< r < r_b$ at $\theta= 0$, and the inside and outside surfaces of the cylinder were stress-free, the combined stress state σ_{ij} ($= \sigma_{pij} + \sigma_{cij}$) then satisfied the following boundary conditions:

$$\sigma_{rr}=\sigma_{r\theta}=0 \quad \text{at } r=r_a \text{ and } r_b; \quad 0\le\theta\le\pi, \quad (6.21a)$$

$$\sigma_{\theta\theta}=\phi(r,t) \quad \text{at } r_c< r < r_b; \quad \theta=0, \quad (6.21b)$$

where ϕ was a crack surface traction determined by conditions of applied loading. From Eq. (6.21), the coefficients $a_n,\ldots, d_n$ could be explained as a function of f with ν and were replaced by $\alpha_n,\ldots, \delta_n$ as follows:

$$\alpha^*_n(r,\nu)=\frac{-4\pi(1-\nu^2)}{\zeta E^*_r f^*}a^*_n,\quad \beta^*_n(r,\nu)=\frac{-4\pi(1-\nu^2)}{\zeta E^*_r f^*}b^*_n,$$

$$\chi_n^*(r,\nu)=\frac{-4\pi\left(1-\nu^2\right)}{\zeta E_r^* f^*}c_n^*,\quad \delta_n^*(r,\nu)=\frac{-4\pi\left(1-\nu^2\right)}{\zeta E_r^* f^*}d_n^*. \tag{6.22}$$

From Eqs. (6.19) and (6.20), I obtained the following singular integral equation for the unknown function f^*:

$$\int_{r_c}^{r_b}\left[\frac{-\zeta E_r^*(\zeta)}{4\pi\left(1-\nu^2\right)}\left(\frac{1}{r-\nu}+g^*(r,\nu,\zeta)\right)f^*(\nu,\zeta)\right]d\nu=-\varphi^*(r,\zeta), \tag{6.23}$$

where

$$g^*(r,\nu,\zeta)=\frac{-\beta_0^*}{r^2}+2\chi_0^*+\left(\frac{2\chi_1^*}{r^3}+6\delta_1^* r\right)$$

$$+\sum_{n=2}^{\infty}\left[\alpha_n^* n(n-1)\,r^{n-2}+\beta_n^*(n+1)(n+2)\,r^n+\chi_n^* n(n+1)r^{-n-2}+\delta_n^*(n-1)(n-2)r^{-n}\right]$$

After $f^*(\nu,\zeta)$ was determined from Eq. (6.23), mode I stress intensity factor, $K_I^*(r,\zeta)$, could be found as follows,

$$K_I^*(\zeta)=\frac{\zeta E_r^*}{4\left(1-\nu^2\right)}\lim_{r\to r_c}\sqrt{2(r-r_c)}f^*(r,\zeta). \tag{6.24}$$

I obtained $K_I(\xi)$ for the reduced time, ξ, by taking the numerical inverse-Laplace transformation of $K_I^*(\zeta)$.

Comparing $K_I(\xi)$ to mode I fracture toughness, $K_{Ic}(\xi)$, in a reduced time region according to Eq. (6.15), I could evaluate the reduced fracture initiation time, ξ_f. The actual fracture initiation time, t_f, could then be derived from ξ_f by Eq. (6.9a).

6.3.3 Conditions for numerical analysis

I next calculate the time of fracture initiation for a thermo-viscoelastic hollow cylinder with an external crack subjected to pressure on the internal surface.

The ratio of inner and outer radiuses r_a and r_b of the cylinder was $r_a/r_b = 0.5$. The external crack length ratio $(r_b\text{-}r_c)/(r_b\text{-}r_a)$ was changed from 0 to 0.8. The material of the thermo-viscoelastic cylinder was the bisphenol A-type epoxy resin which was the same one used in Section 6.2. The mode I fracture toughness, $K_{Ic}(t, T)$, of Epoxy A in Chapter 3 was also used for this analysis.

I assumed the temperature field to be either in a steady or in a transient-isothermal state. The temperature in the steady case ranged from 298 to 373 K, and that for the transient case was given as a fluctuating one.

The history of pressure, p, applied on the inner surface for every model was gradually increased as follows,

$$p(t) = p_a \left\{ 1 - \exp\left(-\frac{t}{\tau_a} \right) \right\} \quad \text{at } r = r_a , \qquad (6.25)$$

where p_a and τ_a were assumed to be constant at 10 MPa and 100 s. In this case, the crack surface traction ϕ in Eq. (6.21b), which was equivalent to the pressure p, was given as:

$$\varphi(r,t) = -\frac{p(t) r_a^2}{r_b^2 - r_a^2} \left(1 + \frac{r_b^2}{r^2} \right) \quad \text{at } r_c < r < r_b;\ \theta = 0 , \quad (6.26),$$

To solve numerically the singular integral equation (Eq. (6.21)), I used the Lobatto-Jacobi integral formula.[6.36]

6.3.4 Results and discussion for steady-temperature field

(A) Stress intensity factor

I analyzed the fracture initiation time for a thermo-viscoelastic cylinder under steady-isothermal temperature conditions. Figure 6.17 shows the histories of stress intensity factors $K_I(t)$ in different crack lengths under the same temperature condition 348 K. As seen in Fig. 6.17, the histories of $K_I(t)$ were similar to the applied pressure $p(t)$ given in Eq. (6.24), and the values of K_I directly depended on the crack lengths, r_b-r_c. The histories of the stress intensity factors $K_I(t)$, however, were entirely independent of the temperature of the isothermal field. This problem has since been statically solved, so $K_I(t)$ had an identical one regardless of the temperature condition.

(B) Same temperature field case

Figure 6.18 shows the master curves of K_I depending on the reduced time ξ for a temperature field of 348K. These master curves were derived from Fig. 6.17 at a standard temperature of T_R = 298 K. Since a_T was constant for the steady temperature case, the master curves of K_I could be easily obtained by uniformly shifting each curve of Fig. 6.17.

Figure 6.19 illustrates the procedure for predicting brittle fracture initiation. Figure 6.19(a) shows the master curves of the stress intensity factor, K_I, with a fracture toughness, K_{Ic}, at T_R = 298 K. The broken line was the master curve of K_{Ic} which was obtained by the least square method from the minimum values of K_{Ic} under each test condition. Figure 6.19(b) shows the relationship between the reduced time, ξ, at T_R = 298 K and the actual time t for the steady-state temperature 348 K. The solid diamond symbol at the intersection of K_I and K_{Ic} in Fig. 6.19(a) denotes the fracture initiation point determined by Eq. (6.15). The times of these symbols denote the reduced time of fracture initiation ξ_f. The actual fracture time t_f could be obtained from ξ_f in Fig. 6.19(b). For example, whenever $(r_b\text{-}r_c)/(r_b\text{-}r_a)$ = 0.80, a brittle fracture occurred at the reduced time $\xi \approx 10^4$ s. The actual fracture initiation time t_f = 26 s was derived

from Fig. 6.19(b). Both t_f and ξ_f increased with a decreasing crack length when they had the same temperature conditions.

Figure 6.20 shows the relationship between the crack length and the fracture initiation time t_f, which was derived from Fig. 6.19. When $(r_b-r_c)/(r_b-r_a)$ was shorter than 0.16, the crack could not propagate because the maximum value of K_I was always smaller than the minimum value of K_{Ic}. When the crack length was long enough, a brittle fracture occurred and the fracture initiation time t_f decreased with an increase in the crack length.

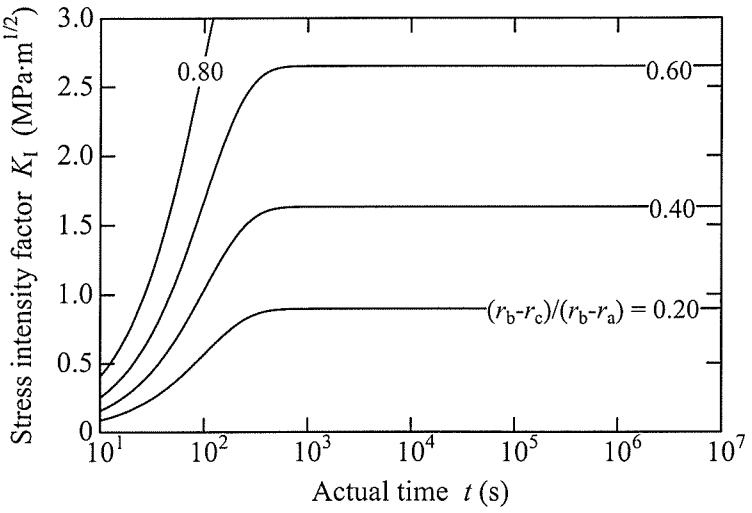

Figure 6.17 History of stress intensity factor for steady-isothermal temperature case 348 K.

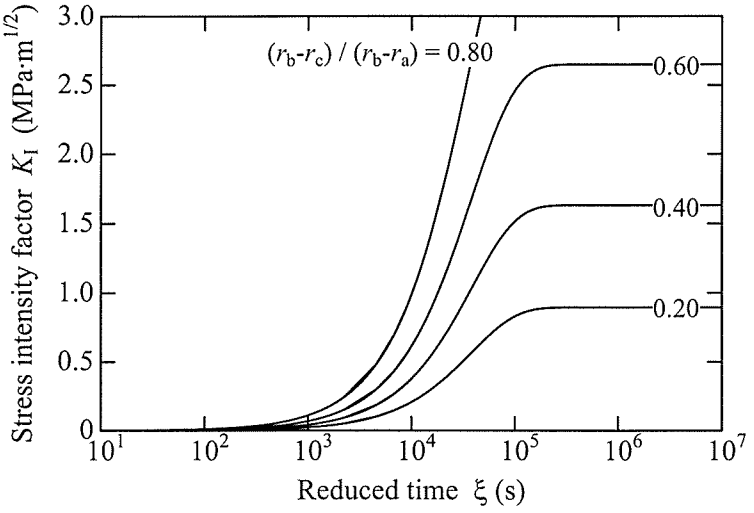

Figure 6.18 Master curve of stress intensity factor for steady-isothermal temperature case 348 K. (Standard temperature is 298 K.)

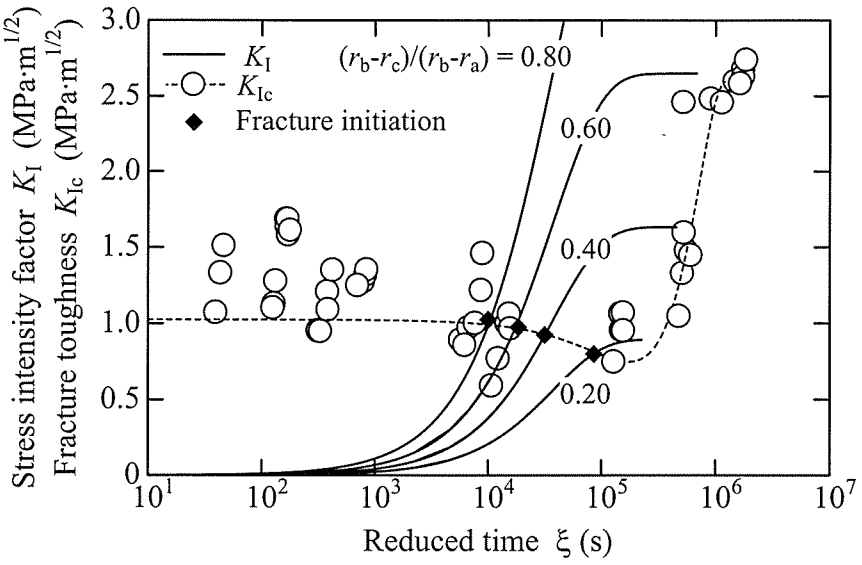

(a) Master curves of stress intensity factor and fracture toughness

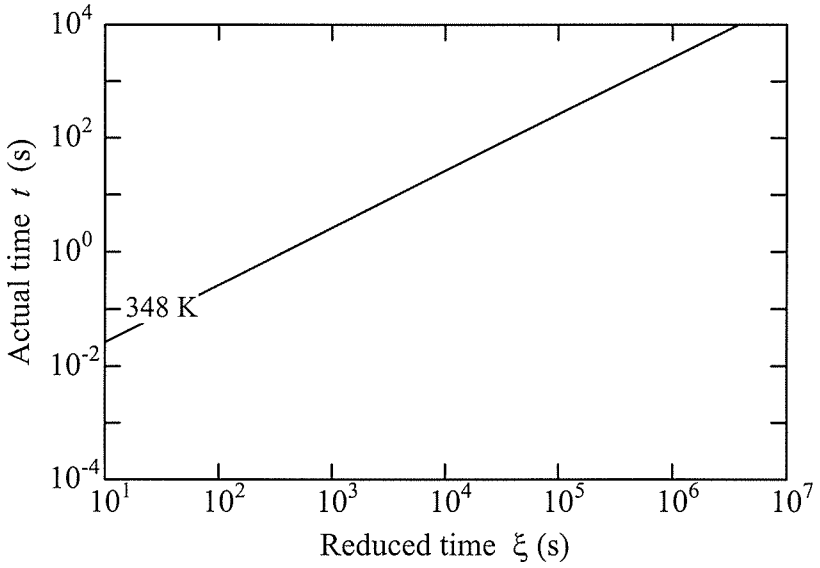

(b) Relationship between reduced time and actual time

Figure 6.19 Brittle fracture initiation for steady-isothermal temperature case 348 K. (Standard temperature is 298 K.)

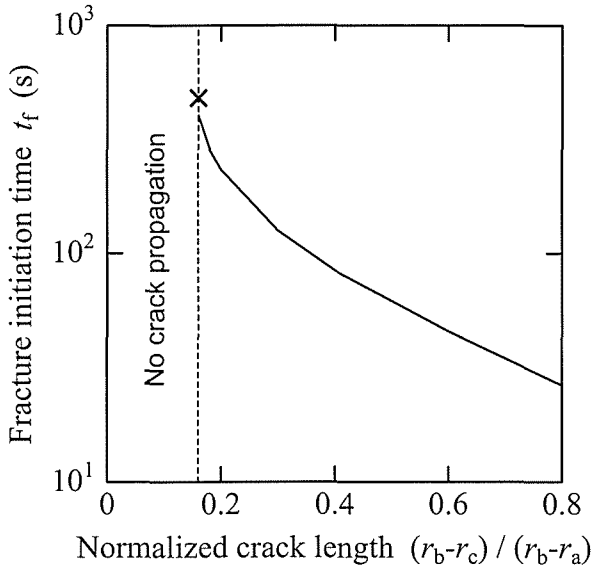

Figure 6.20 Relationship between crack length and fracture initiation time for steady-isothermal temperature case 348 K.

(C) Same crack length case

Figure 6.21 shows the master curves of K_I at a standard temperature 298 K for a constant crack length $(r_b-r_c)/(r_b-r_a) = 0.40$ under different temperatures. Although history of stress intensity factors, $K_I(t)$, did not depend on the temperature of the isothermal field, $K_I(\xi)$ significantly depended on the temperature. Since a high temperature was equivalent to a long reduced time in the thermo-viscoelastic material due to the time-temperature equivalence principle, the master curve of K_I shifted to the longer reduced time side when the temperature was higher.

Figure 6.22 illustrates the procedure for predicting brittle fracture initiation under the same crack length condition, where $(r_b-r_c)/(r_b-r_a) = 0.40$. In Fig. 6.22(a), a brittle fracture for 323 K occurs at $\xi_f \approx 1.8\times10^3$ s. The actual fracture initiation time $t_f = 98$ s was therefore obtained from Fig. 22(b). With respect to the same crack length condition, ξ_f increased but t_f decreased when the temperature rose.

Figure 6.23 shows the relationship between the temperature and the fracture initiation time t_f, which was derived from Fig. 6.22. Whenever $(r_b-r_c)/(r_b-r_a) = 0.40$, the crack could brittlely propagate below 361 K, and t_f was shorter as the temperature increased. Above 361 K, a ductile fracture could occur instead of a brittle fracture.

(D) Critical conditions for crack propagation

Figure 6.24 is a diagram showing the critical conditions of temperature and crack lengths for a brittle fracture, and which summarizes of the results for the isothermal-steady temperature case. Whenever shorter crack length, where $(r_b-r_c)/(r_b-r_a) < 0.16$, the crack could not propagate regardless of the temperature. Whenever longer crack length, where $(r_b-r_c)/(r_b-r_a) \geq 0.16$, a brittle fracture could occur in a low temperature field. When the crack length was long enough for $(r_b-r_c)/(r_b-r_a) \geq 0.16$, and also whenever the temperature was higher, a ductile fracture could occur. For example, in the case of $(r_b-r_c)/(r_b-r_a) = 0.40$, a crack could propagate brittely under 361 K. Above 361 K, however, a ductile fracture occurred.

Brittle fractures could occur under the conditions represented by the gray area in Fig. 6.24 for the steady-isothermal temperature case, therefore, it was possible to predict the brittle fracture initiation time and to estimate the critical conditions required for the crack propagation according to the method proposed here.

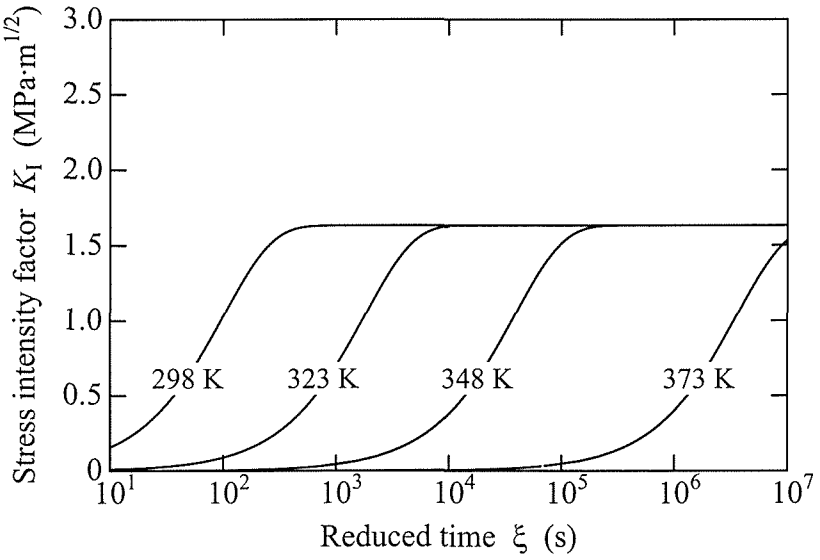

Figure 6.21 Master curve of stress intensity factor for crack length $(r_b\text{-}r_c)/(r_b\text{-}r_a) = 0.40$. (Standard temperature is 298 K.)

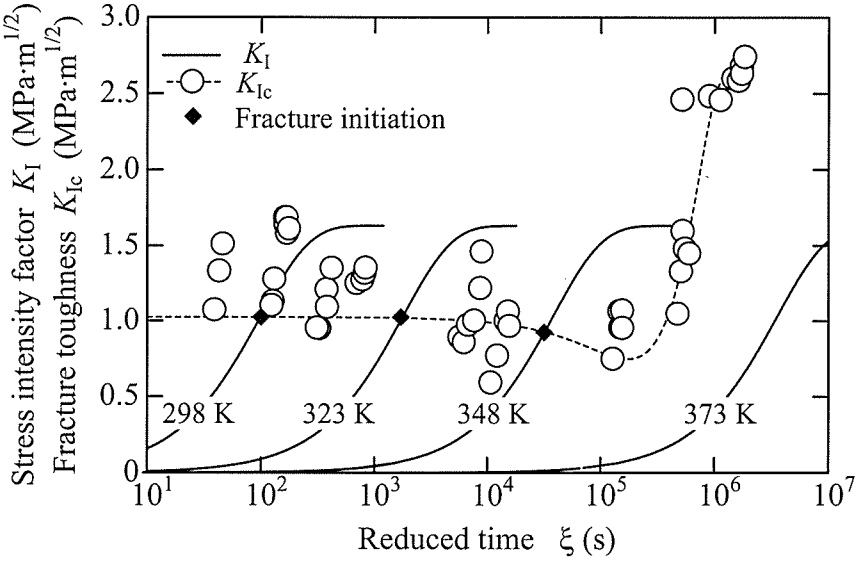

(a) Master curves of stress intensity factor and fracture toughness

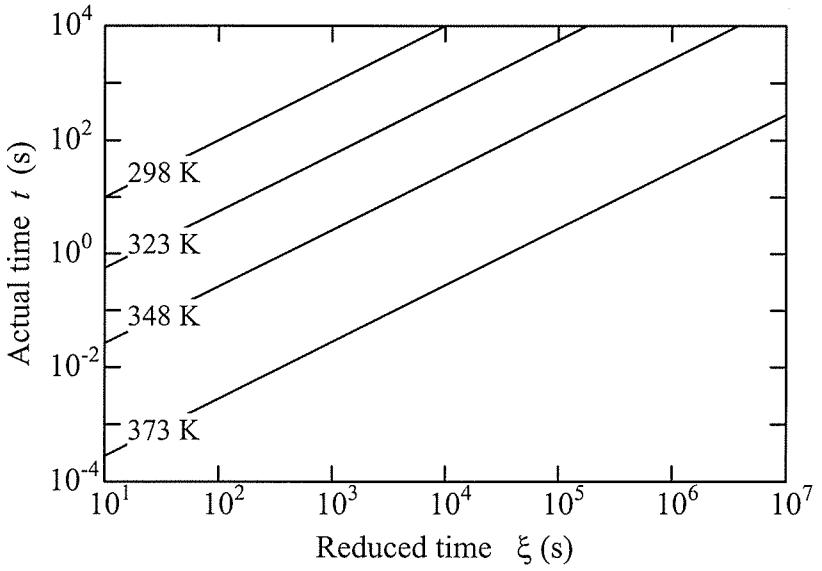

(b) Relationship between reduced time and actual time

Figure 6.22 Brittle fracture initiation for crack length $(r_b\text{-}r_c)/(r_b\text{-}r_a) = 0.40$.
(Standard temperature is 298 K.)

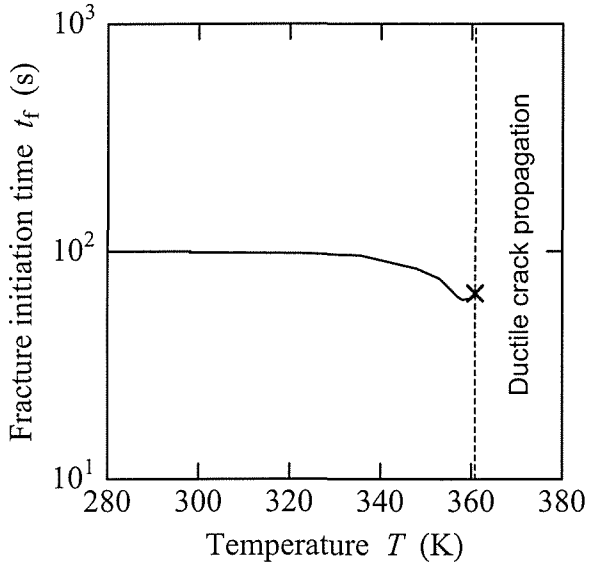

Figure 6.23 Relationship between crack length and fracture initiation time. for crack length $(r_b\text{-}r_c) / (r_b\text{-}r_a) = 0.40$

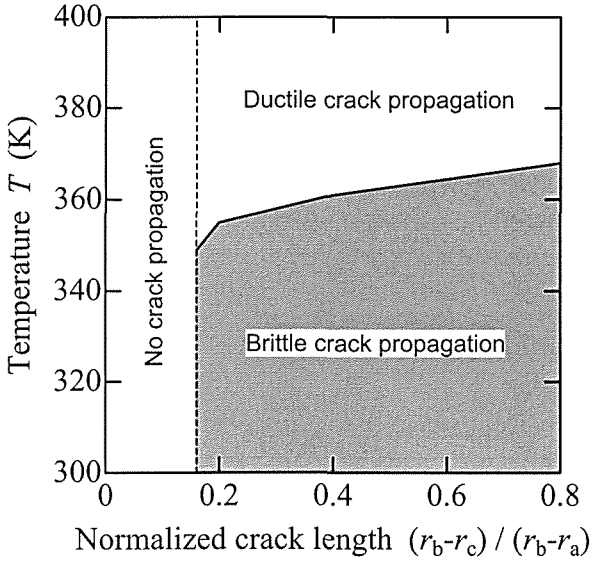

Figure 6.24 Critical conditions required for crack propagation.

6.3.5 Results and discussion for transient-temperature field

I analyzed the fracture initiation time for the case of the transient-isothermal temperature field was given by the following equation:

$$T(t) = T_0 + \frac{1}{2}(T_1 - T_0)\left\{1 - \cos\left(\frac{2\pi t}{\tau}\right)\right\}, \qquad (6.27)$$

where T_0 and T_1 were 298 K and 348 K, respectively, and τ was assumed to be constant at 1000 s.

The history of the stress intensity factor, $K_I(t)$, for a transient temperature case was independent of the temperature history because the temperature field was isothermal. The master curve $K_I(\xi)$, however, greatly depended the on temperature history.

Figure 6.25 shows the master curves of stress intensity factor, K_I, and fracture toughness, K_{Ic}, with the relationship between ξ and t for the transient temperature at the standard temperature T_R = 298 K. Due to temperature fluctuations, the shape of the master curve in the transient case differed from that of $K_I(t)$ in Fig. 6.17, and the relationship between ξ and t was not linear as shown in Fig. 6.25(b). This was because the shift factor a_T varied with the transient-temperature history. The reduced time ξ flowed fast with an increasing in temperature, while ξ passed slowly when the temperature is decreased.

Concerning transient-isothermal temperatures, brittle fracture initiation time t_f could be derived from Fig. 6.25 in the same way as that for the steady case as illustrated in Figs. 6.19 and 6.22. For example, the reduced time of fracture initiation ξ_f was 343 s for $(r_b\text{-}r_c)/(r_b\text{-}r_a)$ = 0.30, so I found that the fracture time t_f was 175 s. In this way, the fracture initiation time t_f could be obtained even when the temperature of the isothermal field was transient.

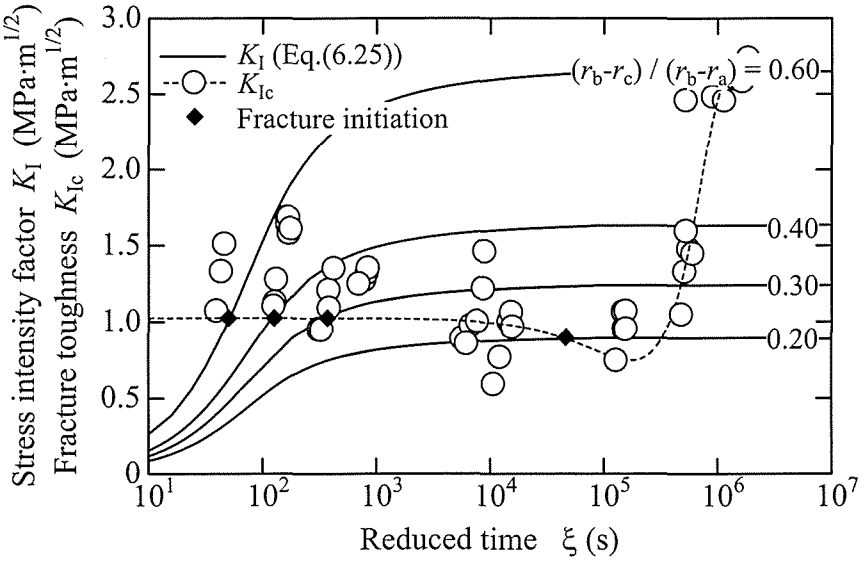

(a) Master curves of stress intensity factor and fracture toughness

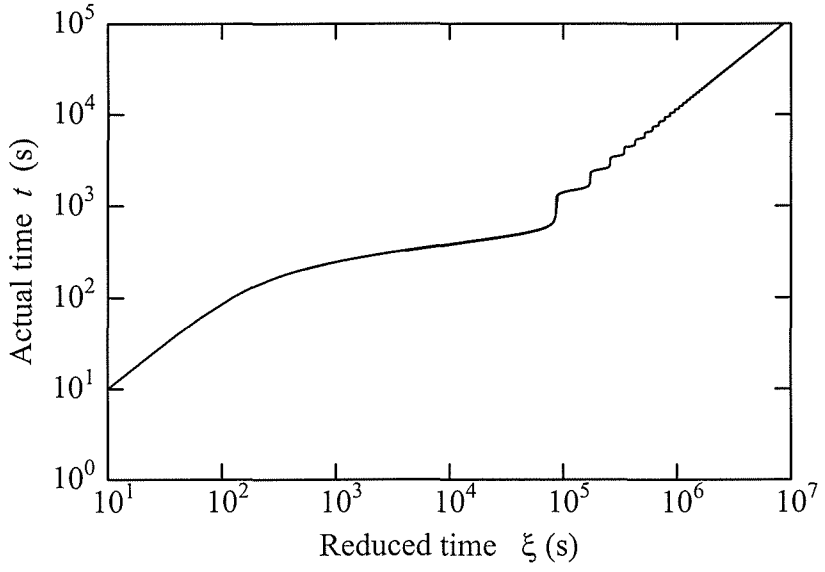

(b) Relationship between reduced time and actual time

Figure 6.25 Brittle fracture initiation for transient-isothermal temperature case.
(Standard temperature is 298 K.)

6.5 CONCLUSION

I proposed a method to predict fracture initiation time for thermo-viscoelastic material by using master curves of stress intensity factor and fracture toughness, which are derived according to the time-temperature equivalence principle. For the present analysis, I used material properties of the epoxy resins.

First, I showed the transient thermal stress analysis on a thermo-viscoelastic hollow cylinder with temperature-dependent thermal properties, which was gradually heated from the inner surface with the outer surface kept at the initial temperature. It was found that the stress distribution was affected by not only the heating temperature but also the size of the cylinder. With a higher heating temperature and a larger cylinder size, the thermo-viscoelastic effect was larger. This is because they were related to the time required to reach a temperature steady-state and that required for stress relaxation to occur, which are attributed to the drastic local relaxation at the vicinity of the inner surface. There was little effect on the temperature dependence of thermal properties. With a higher heating temperature and larger cylinders, the effect of the thermal properties is larger, although its effect on temperature and stress distribution was really small because the temperature conductivity is inherently slow.

Then, I proposed the method to predict fracture initiation time for the thermo-viscoelastic media from the stress field and the fracture toughness considering both time-temperature dependences. I explained the concept of the method with the use of master curves of stress intensity factor and fracture toughness, which are derived according to the time-temperature equivalence principle. As concrete examples, I analyzed a stress intensity factor in a thermo-viscoelastic cylinder with a crack under various temperatures and crack length conditions and explained the process for prediction of fracture initiation time. Particularly for the case of steady-isothermal temperature, I showed that the critical conditions regarding geometry and temperature required for the crack propagation could be obtained by using the proposed method.

Based on the analysis results, I conclude that the proposed method, which takes into account both time-temperature dependences of stress field and fracture toughness, is very useful in estimating crack propagation and is also able to solve various fracture problems dealing with thermo-viscoelastic materials.

REFERENCES

6.1 T.G. Rogers, E.H. Lee, The cylinder problem in viscoelastic stress analysis, Quaterly of Appl. Math. 22, 117-120 (1964).

6.2 E.C. Ting, Stress analysis for linear viscoelastic cylinder, *AIAA* J. 8, 18-22 (1969).

6.3 L.W. Morland, E.H. Lee, Stress Analysis for Linear Viscoelastic materials with temperature variation, *Trans. Soc. Rheol* 4, 233-263 (1960).

6.4 R. Muki, E. Sternberg, On Transient thermal stresses in viscoelastic materials with temperature-dependent properties, Trans. ASME. J. Appl. Mech. 28, 193-207 (1961).

6.5 K.C. Valanis, G. Lianis, A method of analysis of transient thermal stresses in thermorheologically simple viscoelastic solids, Trans. ASME. J. Appl. Mech. 31, 47-53 (1964).

6.6 F.J. Lockett, L.W. Morland, Thermal stresses in a viscoelastic thin-walled tube with temperature dependent properties, Int. J. Engng. Sci. 5, 879-898 (1967).

6.7 R.L. Taylor, K.S. Pister, and G.L. Goudreau, Thermomechanical analysis of viscoelastic solids, Int. J. Numer. Meth. Eng. 2, 45-59 (1970).

6.8 R.L. Frutiger, T.C. Woo, A thermoviscoelastic analysis for circular plates of thermorheologically simple material, J. Thermal Stresses 2, 45-60 (1979).

6.9 L.S. Chien, J.T. Tzeng, A thermal viscoelastic analysis for thick-walled composite cylinders, J. Comp. Mat. 29, 525-548 (1995).

6.10 S.S. Lee, Boundary element analysis of a viscoelastic thin-walled cylinder subjected to thermal transient, Int. J. Ves. Piping 63, 195-198 (1995).

6.11 Y. Miyano, M. Shimbo, Residual stress analysis of an epoxy thick-walled cylinder subjected to rapid cooling, Proc. 1986 SEM Spring Conference on Experimental Mechanics, 195-200 (1986).

6.12 A.D. Drozdov, Thermoviscoelasticity, in *Mechanics of Viscoelastic Solids*, John Wiley & Sons, West Sussex, 382-400 (1998).

6.13 N. Noda, Thermal stresses in materials with tempetature-dependent properties, *Appl. Mech. Rev.* 44, 383-397 (1991).

6.14 N.R. Eyres, D.R. Hartree, J. Ingham, R. Jackson, R.J. Sarjant, and J.B. Wagstaff, The calculation of variable heat flow in solids, *Phil. Trans. Roy. Soc. A* 240, 1-58 (1946).

6.15 H.S. Carslaw, J.C. Jaeger, General theory. In *Conduction of Heat in Solids*, Oxford University Press, Oxford, 1-49 (1959).

6.16 N.A. Badran, M.B. Abd-El-Malek, Group analysis of nonlinear heat-conduction problem for a semi-infinite body, Nonlinear Math. Phys. 2, 319-328 (1995).

6.17 S. Jahanian, Numerical representation of Jiang's constitutive equations for a material with temperature-dependent properties, Eng. Structures 19, 173-178 (1997).

6.18 K.J. Dowding, B.F. Blackwell, Sensitivity analysis for nonlinear heat conduction, J.

Heat Transfer 123, 1-10 (2001).

6.19 R.A. Schapery, A theory of crack initiation andgrowth in viscoelastic media – Parts I, Int. J. Frac. **11**, 141-159(1975)..

6.20 R.M. Christensen, A rate-dependent criterion for crack growth, Int. J. Frac. 15, 3-21(1979).

6.21 R.M. Christensen, E.M. Wu, A theory of crack growth in viscoelastic materials, Eng. Frac. Mech. 14, 215-225 (1981).

6.22 A.A. Griffith, The phenomena of rupture and flow in solids, Phil. Trans. Roy. Soc. Lon. A221, 163–197 (1920).

6.23 R. Frassine, A. Pavan, An application of viscoelastic fracture criteria to steady crack propagation in a polymeric material under fixed deformation, Int. J. Frac. 43, 303-317 (1990).

6.24 F. Dubois, C. Chazal, and C. Petit, Viscoelastic crack growth process in wood timbers: An approach by the finite element method for mode I fracture, Int. J. Frac. 113, 367-388. (2002).

6.25 D. Gamby and J. Chaoufi, Application of viscoelastic fracture criteria to progressive crack propagation in polymer matrix composites, Int. J. Frac. 100, 379-399 (1999).

6.26 J.A.F. Harvey and D. Cebon, Failure mechanisms in viscoelastic films, J. Mater. Sci. 38, 1021-1032 (2003).

6.27 J.R. Masuero, G.J. Creus, Finite elements analysis of viscoelastic fracture, Int. J. Frac. 60, 267-282 (1993).

6.28 S.F. Popelar, M.K. Chengalva, C.H. Popelar, and V.H. Kenner, Accelerated performance evaluation for polyimide films, Time-Dependent Failure of Polymers: Experimental Studies 155, 15-22 (1992).

6.29 Lim, W.W., Mizumachi, H. Fracture toughness of adhesive joints. II. temperature and rate dependencies of mode I fracture toughness and adhesive tensile strength, J. Appl. Polym. Sci. 57, 55-61, (1995).

6.30 R. Frassine, A. Pavan, Viscoelastic effects on the interlaminar fracture behaviour of thermoplastic matrix composites: I. rate and temperature dependence in unidirectional PEI/carbon-fibre laminates, Comp. Sci. Tech. 54, 193-200, (1995).

6.31 F R. Frassine, M. Rink, A. Pavan, Viscoelastic effects on the interlaminar fracture behaviour of thermoplastic matrix composites: II. rate and temperature dependence in unidirectional PEEK/carbon-fibre laminates, Comp. Sci. Tech. 56, 1253-1260 (1996).

6.32 R. Fracasso, M. Rink, A. Pavan, and R. Frassine, The effect of strain-rate and temperature on the interlaminar fracture toughness of interleaved PEEK/CF composites, Comp. Sci. Tech. 61, 57-63 (2001).

6.33 F. Massa, R. Piques, and A. Laurent, Rapid crack propagation in polyethylene pipe: combined effect of strain rate and temperature on fracture toughness, J. Mater. Sci. 32, 6583-6587 (1997).

6.34 O. Krischer, H. Esdorn, Einfaches Kurzzeitverfahren zur gleichzeitigen Bestimmung der Wärmeleitzahl, der Wärmekapazität und der Wärmeeindringzahl fester Stoffe, VDI-Forschungs-Heft 450, 28-39 (1955).

6.35 E. Delale, F. Erdogan, Stress intensity factors in a hollow cylinder containing a radial crack, Int. J. Frac. 20, 251-265 (1982).

6.36 P.S. Theocaris, N.I. Ioakimidis, A method of numerical solution of Cauchy-type singular integral equations with generalized kernels and arbitrary complex singularities, J. Computational Phys. 30, 309-323 (1979).

APPENDIX

A6. Temperature field

The cylinder is discretized to M nodes along radial coordinate r within the region from the inner to the outer surface. Through FDM, general radial coordinate r and real time t are expressed as $r_m = m\Delta r$ and $t_p = p\Delta t$ where Δr and Δt are space and time increments, and m= 1, 2,..., M and p = 1, 2,..., P. Appling central difference to space and forward difference to time, Eq. (6.1) can be approximately described by the following,

$$\left(\frac{\lambda_m^p}{(\Delta r)^2}-\frac{\lambda_m^p}{2r_m\Delta r}+\frac{\hat{\lambda}_m^p}{r^2}\right)\Theta_{m-1}^{p+1}-\left(\frac{2\lambda_m^p}{(\Delta r)^2}+\frac{2\hat{\lambda}_m^p}{(\Delta r)^2}\right)\Theta_m^{p+1}+\left(\frac{\lambda_m^p}{(\Delta r)^2}+\frac{\lambda_m^p}{2r_m\Delta r}+\frac{\hat{\lambda}_m^p}{r^2}\right)\Theta_{m-1}^{p+1} \\ -\left(c_\rho\right)_m^p\frac{\Theta_m^{p+1}-\Theta_m^p}{\Delta t}=0 \qquad \text{, (A6.1)}$$

where

$$\hat{\lambda}_m^p=\frac{\partial\lambda_m^p}{\partial\Theta}$$

Subscript m and superscript p mean values at position r_m and for time t_p, respectively.

Rearranging Eq. (A6.1), the following equation is yielded.

$$A_m^p\Theta_{m-1}^{p+1}+B_m^p\Theta_m^{p+1}+C_m^p\Theta_{m+1}^{p+1}=\Theta_m^p, \qquad \text{(A6.2)}$$

where

$$A_m^p=\frac{-\Delta t}{\left(c_\rho\right)_m^p}\left\{\frac{\lambda_m^p}{\Delta r^2}-\frac{\lambda_m^p}{2r_m\Delta r}+\frac{\hat{\lambda}_m^p}{\Delta r^2}\right\},$$

$$B_m^p=\frac{\Delta t}{\left(c_\rho\right)_m^p}\left\{\frac{2\lambda_m^p}{\Delta r^2}+\frac{2\hat{\lambda}_m^p}{\Delta r^2}+1\right\},$$

$$C_m^p=\frac{-\Delta t}{\left(c_\rho\right)_m^p}\left\{\frac{\lambda_m^p}{\Delta r^2}+\frac{\lambda_m^p}{2r_m\Delta r}+\frac{\hat{\lambda}_m^p}{\Delta r^2}\right\}.$$

Thus, temperature Θ_m^{p+1} at the next time step can be solved explicitly.

B6. Stress field

For the transient temperature field, Eqs. (6.7) and (6.8) can be approximated by the following,

$$\frac{\left(\sigma_{rr}\right)_{m+1}^{p}-\left(\sigma_{rr}\right)_{m}^{p}}{\Delta r}+\frac{\left(\sigma_{rr}\right)_{m}^{p}-\left(\sigma_{\theta\theta}\right)_{m}^{p}}{r_m}=0, \qquad \text{(B6.1)}$$

and

$$\left(\sigma_{rr}\right)_{m}^{p+1}=\nu_0\sum_{i=1}^{p}\left[E_m^{pi}\left\{\left(e_{1m}-e_2\right)u_m^{is}+e_2u_{m+1}^{is}+e_3\theta_m^{is}\right\}\right], \qquad \text{(B6.2a)}$$

$$\left(\sigma_{\theta\theta}\right)_{m}^{p+1}=\nu_0\sum_{i=1}^{p}\left[E_m^{pi}\left\{\left(e_{4m}-e_5\right)u_m^{is}+e_5u_{m+1}^{is}+e_3\theta_m^{is}\right\}\right], \qquad \text{(B6.2b)}$$

where

$$\nu_0=\frac{1}{2\left(1+\nu\right)\left(1-2\nu\right)},$$

$$e_{1m}=\frac{\nu}{r_m},\quad e_2=\frac{1-\nu}{\Delta r},\quad e_3=-\left(1+\nu\right),\quad e_{4m}=\frac{1-\nu}{r_m},\quad e_5=\frac{\nu}{\Delta r},$$

$$E_m^{pi}=\left[E_{\mathrm{rR}}\right]_m^{\langle p+1\rangle-\langle i+1\rangle}+\left[E_{\mathrm{rR}}\right]_m^{\langle p+1\rangle-\langle i\rangle},\quad \left[E_{\mathrm{rR}}\right]_m^{\langle p\rangle-\langle i\rangle}=E_{\mathrm{rR}}\left(\xi_m^p-\xi_m^i;\Theta_{\mathrm{R}}\right),$$

$$u_m^{is}=u_m^{i+1}-u_m^i,\quad \theta_m^{is}=\alpha_m^i\Theta_m^{is}=\alpha_m^i\left(\Theta_m^{i+1}-\Theta_m^i\right).$$

Substituting Eq. (B6.1) into (B6.2), we obtain Eq. (B6.3),

$$\nu_0\sum_{i=1}^{p}\left[F_{1m}u_{m-1}^{is}+F_{2m}u_m^{is}+F_{3m}u_m^{is}+F_{4m}\right]+\nu_0\sum_{i=1}^{p}\left[F_{5m}u_m^{is}+F_{6m}u_m^{is}\right]=0, \qquad \text{(B6.3)}$$

where

$$F_{1m}=f_1E_m^{pi},\quad F_{2m}=-\left(f_1+f_{2m}+2f_{3m}\right)E_m^{pi}+\left(f_{3m}-f_1\right)E_{m+1}^{pi},\quad F_{3m}=f_{3m}E_m^{pi}+f_1E_{m+1}^{pi},$$

$$F_{4m}=f_4\left[\left\{\alpha_m^i\left(\Theta_{m+1}^{is}-2\Theta_m^{is}\right)+\dot{\alpha}_m^i\left(\Theta_{m+1}^i-\Theta_m^i\right)\Theta_m^{is}\right\}E_m^{pi}+\alpha_m^i\Theta_m^{is}E_{m+1}^{pi}\right],$$

$$F_{5m}=-\left(f_{5m}+f_{6m}\right)E_m^{pi},\quad F_{6m}=f_6E_m^{pi},$$

$$f_1=\frac{1-\nu}{\Delta r^2},\quad f_{2m}=\frac{\nu}{r_m^2},\quad f_{3m}=\frac{\nu}{r_m\Delta r},\quad f_4=-\frac{1+\nu}{\Delta r},\quad f_{5m}=\frac{1-2\nu}{r_m^2},\quad f_{6m}=\frac{1-2\nu}{r_m\Delta r},$$

$$\dot{\alpha}_m^i=\frac{\partial\alpha_m^i}{\partial\Theta}.$$

Equation (B6.3) yields the following equation,

$$G_m^pu_{m-1}^{p+1}+H_m^pu_m^{p+1}+I_m^pu_{m+1}^{p+1}=J_m^p, \qquad \text{(B6.4)}$$

where

$$G_m^i=h_1E_m^{pi},\quad H_m^i=-\left(h_1+h_{2m}+h_{3m}\right)E_m^{pi}+\left(h_{4m}-h_1\right)E_{m+1}^{pi},\quad I_m^i=h_{5m}E_m^{pi}+h_1E_{m+1}^{pi},$$

$$J_m^p=J_{1m}^p+J_{2m}^p+J_{3m}^p,$$

$$J_{1m}^{p} = F_m^p u_{m-1}^p + G_m^p u_m^p + H_m^p u_{m+1}^p, \quad J_{2m}^{p} = -\sum_{i=1}^{p-1}\left[F_m^i u_{m-1}^{is} + G_m^i u_m^{is} + H_m^i u_{m+1}^{is}\right],$$

$$J_{3m}^{p} = h_6 \sum_{i=1}^{p}\left[\left\{\alpha_m^i\left(\Theta_{m+1}^{is} - 2\Theta_m^{is}\right) + \dot{\alpha}_m^i\left(\Theta_{m+1}^i - \Theta_m^i\right)\Theta_m^{is}\right\} E_m^{pi} + \alpha_m^i \Theta_m^{is} E_{m+1}^{pi}\right],$$

$$h_1 = \frac{1-\nu}{\Delta r^2}, \quad h_{2m} = \frac{1-\nu}{r_m^{\,2}}, \quad h_{3m} = \frac{1}{r_m \Delta r}, \quad h_{4m} = \frac{\nu}{r_m \Delta r}, \quad h_{5m} = \frac{1-\nu}{r_m \Delta r}, h_6 = \frac{1+\nu}{\Delta r}.$$

Thus, the displacement u_m^{p+1} at the next time step can be explicitly solved by Eq. (B6.4). Substituting u_m^{p+1} for Eq. (B6.2) gives stresses $\left(\sigma_{rr}\right)_m^{p+1}$ and $\left(\sigma_{\theta\theta}\right)_m^{p+1}$ at the next time step.

Chapter 7

Conclusion

7.1 CONCLUSION

I investigated the thermo-viscoelastic effect on the fracture toughness of epoxy resin. Particularly, I focused on the three objectives: One was to clarify the relationship between the fracture toughness and the network morphology, which is closely related to thermo-viscoelasticity. Parameters for the network morphology would be useful for estimating fracture toughness and also for determining curing conditions. The second one was to clarify the time-temperature dependence of the fracture toughness due to the thermo-viscoelastic relaxation. If the time-temperature equivalence principle has applicability to fracture toughness, it will become possible to easily obtain broad time-temperature dependence of the fracture toughness using the principle. The third one was to propose method for predicting fracture initiation in such thermo-viscoelastic materials as epoxy materials, allowing for both the time-temperature dependences of stress field and also fracture toughness.

In Chapter 2, "Mode I fracture toughness at room temperature," I discussed the relationships between the network morphology and the mode I fracture toughness, K_{Ic}, at room temperature for bisphenol-A type epoxy resins and silica particulate-filled epoxy composites. The glass transition temperature, T_g, and the fragility parameter, m, derived from the thermo-viscoelasticity were used in order to characterize the epoxy resins and the

composites post-cured under various conditions and different volume fractions of silica particles.

Raman spectroscopic analysis proved that T_g expresses the degree of the cross-linking reaction of the epoxy resins and the matrix resins in the composites. The fractography results showed that m of the epoxy resin depends on the heterogeneous microstructure but that m of the composite was dominated by the volume fraction of the silica particle. The K_{Ic} of the epoxy resins increased as m decreased when T_g saturated at approximately 400 K. The K_{Ic} of the composites with a high T_g and low m was high. For the epoxy resins and the composites, therefore, the specimen with higher T_g and also lower m has a higher K_{Ic} value. I concluded, based on the experimental results, that T_g and m are very useful for characterizing these materials and estimating mode I fracture toughness at the room temperature.

In Chapter 3, "Time-temperature dependence of mode I fracture toughness," I discussed the relationships between the network morphology and the time-temperature dependence of mode I fracture toughness, K_{Ic}, for the bisphenol-A type epoxy resins and silica particulate-filled epoxy composites. First, the time-temperature dependence of K_{Ic} was investigated in the epoxy resins and the composites. The T_g and m were then used to characterize them.

It was found that K_{Ic} of the epoxy resin and composite depends on both temperature and time and that K_{Ic} follows the time-temperature equivalence principle. The time-temperature dependence behavior of K_{Ic} was affected by m: K_{Ic} of the epoxy resin with a smaller m increased from lower temperatures to the brittle-ductile transition temperature than that of resin with a larger m when their T_g saturated at approximately 400 K. The composite had smaller m than the epoxy resins so that K_{Ic} increased from a much lower temperature. In contrast, the brittle-ductile transition was governed by α-relaxation phenomena expressed by T_g, independent of m. I concluded that T_g and m are useful parameters not only for characterizing these epoxy materials but also for estimating the time-temperature dependence of mode I fracture toughness.

In Chapter 4, "Time-temperature dependence of mode II fracture toughness," I discussed the mode II fracture toughness, K_{IIc}, of the bisphenol A-type of epoxy resin at room temperature and its time-temperature dependence. I performed an asymmetric four-point bending test under various conditions of temperature and displacement rate to investigate time-temperature dependence of K_{IIc}.

It was found, from the test results conducted at the room temperature under a constant displacement rate, that K_{IIc} strongly depended on the displacement rate and the temperature even at the room temperature due to the thermo-viscoelastic effect and also that there was no clear correlation between T_g, m, and K_{IIc}. The test results under various temperature and rate conditions showed that K_{IIc} followed the time-temperature equivalence principle in regard to

the fracture time. The time-temperature dependence of K_{IIc} was similar to that of dynamic loss modulus, E'', and the transition from brittle to ductile fractures occurred nearly simultaneously when E'' peaked. I concluded that the time-temperature dependence of K_{IIc} must be considered in order to evaluate K_{IIc} and obtain the relationships between T_g, m, and K_{IIc} even at room temperature for the epoxy resins. I also suggested that a similar result could go for other thermo-viscoelastic materials.

In Chapter 5, "Mixed mode fracture toughness at room temperature," I discussed the fracture locus and the direction of the crack initiation under the mixed mode I/II loading for the epoxy resins at the room temperature. To obtain an angle of fracture initiation and fracture locus, $(K_I)_c/K_{Ic}$ – $(K_{II})_c/K_{Ic}$, under mixed mode loading over a whole mode mixity, ϕ, I conducted two kinds of asymmetric bending tests. I compared the experimental results with four common fracture criteria – maximum hoop stress criterion, minimum strain energy density criterion, maximum energy release rate criterion, and Richard's empirical criterion.

The angle of crack initiation became larger with increasing ϕ. The angle obtained from the experiments was in relatively good agreement with every criterion at lower ϕ, namely, near pure mode I. In the vicinity of $\phi = 1.0$, namely pure mode II, the angle corresponded to the one predicted by the maximum hoop stress criterion. In specimens with different T_g, the angles well accorded with each other independently of T_g. As for mixed mode fracture toughness, the mode I component of fracture toughness, $(K_I)_c$, under mixed mode loading monotonically decreased with ϕ. The mode II component, $(K_{II})_c$, increased with ϕ, particularly at the vicinity of $\phi = 1$, because of the thermo-viscoelastic relaxation effect. On account of this drastic increase of $(K_{II})_c$ and thus the variation of relaxation effect with ϕ, the fracture locus in the experimental result had a non-elliptical form, although almost all common criteria predict an elliptical form. In specimens with different T_g, the $(K_I)_c$ with ϕ was almost the same, while the $(K_{II})_c$ and fracture locus were different from each other. I concluded that the relaxation effect on fracture toughness varies with the mode mixity, so the common fracture criteria for mixed mode can not be applied to epoxy resins. In contrast, the crack initiation angle can be possibly determined independently of the relaxation effect.

In Chapter 6, "Prediction of fracture initiation in thermo-viscoealstic media," I proposed a method for predicting fracture initiation time for thermo-viscoelastic media using master curves of the stress intensity factor and fracture toughness, which were derived according to the time-temperature equivalence principle.

First, I analyzed the transient thermal stress on a thermo-viscoelastic hollow cylinder with temperature-dependent thermal properties, which was gradually heated from the inner surface with the outer surface kept at the initial temperature. It was found that the stress distribution was affected by not only the heating temperature but also by the size of the cylinder. With either higher heating temperatures or a larger cylinder, the thermo-viscoelastic

effects on the stress field were larger. Similarly, with higher heating temperatures and a larger cylinder, the effects of the temperature dependence of the thermal properties and stress distribution were larger, although the effects were actually quite small because the temperature conductivity was inherently slow.

Then, I proposed the method to predict fracture initiation time for the thermo-viscoelastic media where both the stress field and the fracture toughness have the time-temperature dependence. I explained how the method uses the master curves of stress intensity factor and fracture toughness, which can be derived according to the time-temperature equivalence principle. As concrete examples, I analyzed the stress intensity factors in a thermo-viscoelastic cylinder with a crack under various temperature and crack length conditions to explain the prediction process for fracture initiation time. Particularly for the case of steady-isothermal temperature, I obtained the critical conditions regarding the geometry and temperature required for crack propagation using the proposed method. Based on the analysis results, I concluded that the proposed method, which takes the time-temperature dependences of the fracture toughness as well as the stress field that of into account, is useful in estimating crack initiation and also can solve various fracture problems in thermo-viscoelastic materials such as epoxy materials.

The significant conclusions drawn from this work are summarized below:

Morphology of epoxy resins can be characterized by the glass transition temperature, T_g, and the fragility parameter, m, which can be derived from the thermo-viscoelasticity. The former is closely related to the degree of cross-linking reaction and the latter to the heterogeneity in cross-link density. Mode I fracture toughness, K_{Ic}, of epoxy resins at room temperature depends on the morphology: The K_{Ic} increased as m decreased when T_g saturated at approximately 400 K. For the case of silica-particulate epoxy composites, T_g expresses the degree of the cross-linking reaction of matrix epoxy resins and m is dominated by the volume fraction of the silica particles. Composites with higher T_g and lower m have higher K_{Ic} values. Therefore, T_g and m are very useful for characterizing materials and estimating K_{Ic} for epoxy resins and their composites.

The fracture toughnesses of the epoxy resins and composites for both mode I and II have time-temperature dependences because of thermo-viscoelastic effect. Master curves of the fracture toughnesses can be obtained using shift factors of the dynamic storage modulus according to time-temperature equivalence principle with regard to fracture time. The master curves of both mode I and mode II fracture toughness have a shape similar to that of dynamic loss modulus; however, the thermo-viscoelastic effect on mode II fracture toughness is larger than that on mode I fracture toughness at room temperature; that is, shear loading causes thermo-viscoelastic relaxation more easily than tensile loading does. Therefore, for mode I and II fractures, the dependence of relaxation time on temperature is almost the same, while

the distribution of the relaxation time differs from each other. In addition, m is strongly related to time-temperature dependence of K_{Ic} while T_g is related to the transition point of brittle-ductile fracture; therefore, T_g and m are useful even for estimating the time-temperature dependence of K_{Ic}.

To obtain a fracture criterion for mixed mode I/II fracture in such thermo-viscoelastic materials as epoxy resins, the thermo-viscoelastic effect on fracture toughness must be considered, even for fractures at room temperature. The thermo-viscoelastic effect on fracture toughness varies with the loading mode, so that the general fracture criteria, which assume that fracture energy is inherently constant, are also inapplicable to epoxy materials. In contrast, the crack initiation angle can be probably estimated using a mode I component of fracture toughness independently of the thermo-viscoelastic effect.

To predict fracture phenomena in the thermo-viscoelastic media in thermal environments, the thermo-viscoelastic effect on fracture toughness must be considered, in addition to that on the stress field. The method proposed in this dissertation, which was derived according to the time-temperature equivalence principle, allows for the thermo-viscoelastic effects on both stress field and fracture toughness. With the proposed method, therefore, fracture initiation in the thermo-viscoelastic media subjected to any temperature and time environment is predictable.

7.2 Future Work

Based on above results and conclusions, I offer the following future prospects:

As for the time-temperature dependence of fracture toughness, it is suggested that a master curve of fracture toughness allowing for time-temperature dependence could exist regardless of the loading mode or that the master curves for mode I and II fracture toughnesses might agree with each other when the master curves are obtained under not different test conditions in a real time space but *thermo-viscoelastically* under the same conditions in a reduced time space.

As for the fracture criterion for mixed mode, it is necessity to establish an alternative criterion that takes into account variations of the thermo-viscoelastic effect on fracture toughness with the loading mode. A criterion might exist for fracture toughness obtained under *thermo-viscoelastically* the same conditions in a reduced time space. Further experiments and mathematical or numerical analyses are needed to clarify these matters. If such master curves and mixed mode criterion are obtained, fracture initiations in thermo-viscoelastic media can be easily predicted under any environment and loading mode conditions according to the method proposed in this dissertation.

Epoxy resins with a more heterogeneous structure in the cross-link density could show much higher mode I fracture toughness. For example, quenching after curing could be an

effective way to make a heterogeneous network in epoxy resins and increase fracture toughness. Also, by using epoxide resins with extremely heterogeneous distribution of molecular weights or curing agents with various numbers of functional groups, epoxy resins could have intrinsically heterogeneous network structures and be toughened without losing any of their excellent properties. Moreover, these heterogeneous epoxy resins are expected to show other unique thermal and electrical properties that greatly depend on relaxation phenomena. I expected that a parameter regarding free volume would be most effective for estimating network morphology because the free volume is closely related to both the glass transition temperature and fragility parameter. In addition, studies of the relationships among the free volume, network morphology, and the fracture toughness will give fresh views on glass transition phenomena, which are still controversial.

All results presented in this dissertation and expected in future work would be applicable to most thermo-viscoelastic polymer and composite materials. Particularly, applying them to recent nanocomposites, such as nano-sized particulate-filled composites and organic-inorganic hybrid materials on molecular level, would be interesting.